KTH Architecture and
the Built Environment

Blast-Induced Vibrations and Stress Field Changes around Circular Tunnels

Carl Wersäll

Master of Science Thesis 08/04
Division of Soil- and Rock Mechanics
Dept. of Civil and Architectural Engineering
Royal Institute of Technology
Stockholm 2008

Master of Science Thesis 08/04
Division of Soil and Rock Mechanics
ISSN 1652-599X

Abstract

Blast-induced vibrations is a common problem in urban areas during rock excavation and can cause damage to existing structures. Risk management of this problem is regulated in various standards for assessment of damage in buildings and other structures above ground. For underground structures, however, there exists no proper method for damage assessment which is why guidance levels intended for on-ground structures are implemented below ground even though the damage criteria are different. New methods for determining these criteria are therefore necessary. The aim of this study is to propose a more refined concept of blast-induced vibration analysis which can be applied in that process.

The problem of dynamic interaction of waves with underground structures is idealized to a cylindrical tunnel in an infinite elastic material (with no material damping) subjected to a plane sinusoidal wave. The main focus is on the compressional wave since this is the predominant type in blast-induced vibrations. However, the interaction of a shear wave is also evaluated briefly for understanding due to its simpler nature.

The dynamic response of a circular tunnel was investigated by mathematical analysis and numerical simulation using the three-dimensional distinct element software 3DEC. It was found that a cylindrical cavity shows resonance phenomena when the wavelength of the P-wave is equal to the circumference of the cavity or when the wavelength of the SH-wave is equal to the diameter. This implies that there is a risk of vibration amplification due to resonance during blasting since the dominating frequency of the vibrations is often of the same order of magnitude as the resonance frequency. Furthermore, the tangential stresses caused by the propagating wave are not negligible and might cause damage to the tunnel. The maximum tangential stress can be approximated by a simple relationship.

Sammanfattning

Omgivningspåverkan från vibrationer är ett vanligt problem i samband med sprängningsarbeten i urbana områden och kan orsaka skador på byggnadsverk m.m. Riskhantering i samband med detta regleras i olika standarder och anvisningar som är framtagna för byggnadsverk ovan jord. För anläggningar under markytan, såsom tunnlar, existerar dock ingen lämplig metod för att förutsäga och kvantifiera skador varför gränsvärden som är framtagna för ovanjordskonstruktioner även tillämpas under jord. Detta trots att skadefallen ej är jämförbara. Därför finns behov av nya metoder för att kunna fastställa skadekriterier. Denna studie är avsedd att ge förbättrade prognosmetoder som kan vara av praktisk nytta i denna process.

Problemet är idealiserat till en cirkulärcylindrisk kavitet i ett oändligt linjärelastiskt material (utan materialdämpning) som utsätts för en plan sinusformad våg. Fokus ligger på tryckvågor eftersom de är dominerande i sprängningsinducerade vibrationer; men även skjuvvågor har undersökts eftersom de är enklare att analysera och därför är mer lättförståliga.

Den dynamiska responsen av en cylindrisk tunnel undersöktes med matematisk analys och numeriska simuleringar i det tredimensionella distinkta elementprogrammet 3DEC. Det visades att en cirkulärcylindrisk kavitet uppvisar resonansfenomen då P-vågens våglängd är lika med kavitetens omkrets eller då SH-vågens våglängd är lika med diametern. Det betyder att det finns risk för resonans i samband med sprängningsarbeten då den dominerande frekvensen är av samma storleksordning som resonansfrekvensen. Dessutom är de dynamiska förändringarna av tangentialspänningen runt tunneln ej försumbara och det kan därför föreligga risk för skada. Den maximala tangentialspänningen kan uppskattas med hjälp av ett enkelt samband.

Preface

This Master of Science thesis is the result of six months work at the Royal Institute of Technology (KTH), Stockholm, and Berg Bygg Konsult AB (BBK), Solna. The supervisors of this project were Dr Martin Jonsson (BBK) and Dr Anders Bodare (KTH).

I would like to thank Dr Martin Jonsson who has been supervising this entire study and offering much of his time and knowlegde to help me increase the quality of my work. I would also like to thank Dr Anders Bodare for guiding me in performing analyses and teaching me all the necessary mathematics. Thanks also to Dr K. Rainer Massarsch (Resonator International AB) for providing valuable comments and helping in progress of this work. Without the experience and devotion of these three people this study would not have been possible and would certainly not have been such a pleasant experince as it came to be.

Last but not least i would like to thank Diego Mas Ivars (Itasca Geomekanik AB) for taking his time to check the FDM model and suggest improvements.

Stockholm, April 2008

Carl Wersäll

List of symbols

a	tunnel diameter
c_P	P-wave velocity
c_S	S-wave velocity
E	elastic modulus
f	frequency
f_r	resonance frequency
$H_n^{(1)}$	Hankel function of the first kind and n:th order
$H_n^{(2)}$	Hankel function of the second kind and n:th order
i	$\sqrt{-1}$
J_n	Bessel function of the first kind and n:th order
K	bulk modulus
k	wave number
k_P	compressional wave number
k_{Pr}	P-wave number at resonance
k_r	wave number at resonance
k_S	shear wave number
k_0	pressure coefficient
M	constrained modulus
p_z	vertical in-situ stress
r	radial coordinate
t	time
u	particle displacement
$\hat{u}$	particle displacement amplitude
$\dot{u}$	particle velocity
$\ddot{u}$	particle acceleration
u_0	particle displacement amplitude of incoming wave
v	particle velocity
v_0	particle velocity amplitude of incoming wave
$\hat{v}$	particle velocity amplitude
w	total particle displacement caused by an SH-wave
$w^{(i)}$	particle displacement of incoming SH-wave
$w^{(s)}$	particle displacement of scattered SH-wave
w_0	particle displacement amplitude of incoming SH-wave
x	cartesian coordinate
Y_n	Bessel function of the second kind and n:th order
y	cartesian coordinate
Z	impedance
z	cartesian coordinate
ε	strain
θ	angular coordinate anticlockwise from the direction of wave propagation
κ	ratio of S- and P-wave numbers
λ	Lamé constant
λ	wavelength

λ_r	wavelength at resonance
μ	Lamé constant (shear modulus)
ν	Poisson's ratio
ρ	density
σ	stress
φ	particle displacement potential of P-wave
φ_0	particle displacement potential amplitude of incoming P-wave
ψ	particle displacement potential of SV-wave
ω	circular frequency
ω_r	circular resonance frequency

Contents

1 INTRODUCTION

This thesis aims to enhance the understanding of damage mechanisms in tunnels and other underground structures when subjected to blast-induced vibrations. Due to the lack of extensive studies in this field, it is to be regarded as an initial step in the process of defining damage criteria and thus providing the proper tools for risk management for existing underground rock excavations during construction in urban areas. An idealized case of a circular cylindrical tunnel of infinite length in an infinite linear elastic material subjected to a plane wave is evaluated.

1.1 Background

As cities become more crowded, the need for increased capacity of transportation is an imminent problem. In densely populated areas, constructing new roads and railroads on the ground is, however, usually not possible due to lack of space. Therefore the solution is often to construct tunnels underground. In urban areas, however, there are already many existing underground excavations, such as road tunnels, subway and various tunnels for power, communications, water supply etc. These structures are affected by excavation in their vicinity, partly by static effects such as redistribution of stresses, but there are also the dynamic concerns such as construction-induced vibrations. Underground structures are also affected by construction on or above ground.

In cities with shallow soil deposit, such as Stockholm where there are several large underground infrastructure projects in progress, excavation is usually performed in rock. Blasting is the most frequently used method for rock excavation (Ouchterlony and Niklasson, 2004) and can generate vibrations which affect nearby structures. The effect these vibrations have on buildings and other structures on the ground surface is relatively well documented. For existing underground excavations, however, the impact is not thoroughly understood. Prediction methods and guidance levels developed for structures are often applied even though other considerations have to be made than above ground. In Sweden, threshold levels for vibrations in existing tunnels in the vicinity of ongoing blasting activity are commonly decided based on the Swedish Standard SS 460 48 66 (Swedish Standards Institute, 1991) or on the Stockholm Transport (SL) general recommendations Fö-I-364 and Fö-I-365 (AB Storstockholms Lokaltrafik, 2001a,b) which to some extent are based on the Swedish Standard. This standard was developed for buildings on the ground surface and should therefore not be applied for underground structures without taking into consideration that damage criteria underground are different from those in

buildings. Even though the difference in dynamic response between conventional buildings and tunnels is well known, this is still the only existing method for determining guidance levels. In some exceptional cases, more sophisticated prediction methods have been used (usually combinations of finite element analysis, field measurements and experimental blasting). Studies are therefore needed to identify possible damage mechanisms in underground structures when they are subjected to blast-induced vibrations so that safe and more economical blasting is possible.

The planning and execution of blasting in urbanized areas is a complex task due to the many parameters that can influence the propagation of vibrations and their interaction with tunnels. The prediction of blast-induced vibrations can be uncertain and difficult to model. Some of the factors affecting wave propagation and damage are:

- Local geology.
- In-situ stress.
- Shape of tunnel.
- Reinforcement in tunnel.
- Wave velocities of rock or soil mass.
- Deformation characteristics of rock or soil mass.
- Soil-structure interaction (for lined rock tunnels or concrete tunnels in soil).
- Characteristics of the incident vibrations, such as:
  - Amplitude (particle displacement, velocity and acceleration).
  - Dominating frequency.
  - Number of cycles.

1.2 Objectives

The objective of this thesis is to analyze in detail the steady state dynamic response of a cylindrical cavity when exposed to a propagating wave front. The assumed vibration input is a plane wave with sinusoidal waveform and the material is linear elastic with deformation moduli of intact rock. The results obtained herein are intended as a basis for further research for determining damage criteria in tunnels and other underground structures. The main goals of this study are to:

- Quantify particle displacement, velocity and acceleration around the cavity.
- Quantify stress field change around the cavity caused by the vibrations.
- Determine the resonance frequency of a circular tunnel.

1.3 Outline

The dynamic response of tunnels when exposed to different wave types was investigated mathematically. For shear waves, existing analytical solutions for the dynamic response were evaluated and a parametric study was performed focusing on frequency (Section 3.2). For compressional waves, analytical expressions for the response of a cylindrical cavity were derived and evaluated (Section 3.3). The evaluation focused on the study of the influence of frequency (wavelength) and radial distance from the circumference on resulting particle velocity and tangential stress. The results obtained by mathematical analyses of the response to compressional waves were then verified by numerical simulations in 3DEC (Section 4.3).

2 THEORETICAL FRAMEWORK

A brief overview of the theoretical background will be presented in this chapter. For a thorough explanation of wave propagation in elastic materials, see Graff (1975). Extensive coverage of soil dynamics can be found in various texts, for example, Bodare (1997), Towhata (2008) or Kramer (1995).

2.1 Wave propagation in elastic media

Wave motion can be described as movement of energy through a material. The transportation of energy is achieved by particles translating and returning to equilibrium after the wave has passed (Bodare, 1997). Two types of waves can propagate in an elastic infinite material, compressional waves and shear waves. The compressional wave propagates faster than the shear wave and is therefore the first to reach an observation point when both wave types have been generated simultaneously at a distant source (e.g. an earthquake or a blast round). Therefore, the compressional wave is denoted P-wave (primary) and the shear wave is denoted S-wave (secondary). The direction of particle motion relative to the direction of propagation is coincident for the P-wave and perpendicular for the S-wave, as shown in Figure 2.1. The P- and S-waves are called *body waves* (as opposed to *surface waves*).

A distinction is made between particle velocity and propagation velocity. Particle velocity is the velocity of the individual particles which oscillates around an equilibrium state. Together with particle displacement, particle acceleration and frequency it describes the vibration characteristics and it is a property of the vibration signal. An example of a particle velocity history from a blast signal is shown in Figure 2.2 and its corresponding frequency spectrum is shown in Figure 2.3. Propagation velocity, however, is a material property and describes how fast a wave moves through the material. Some examples of P- and S-wave velocities for different types of soil are shown in Table 2.1. The P- and S-wave velocities can be obtained by

$$c_P = \sqrt{\frac{M}{\rho}} \tag{2.1}$$

and

$$c_S = \sqrt{\frac{\mu}{\rho}}, \tag{2.2}$$

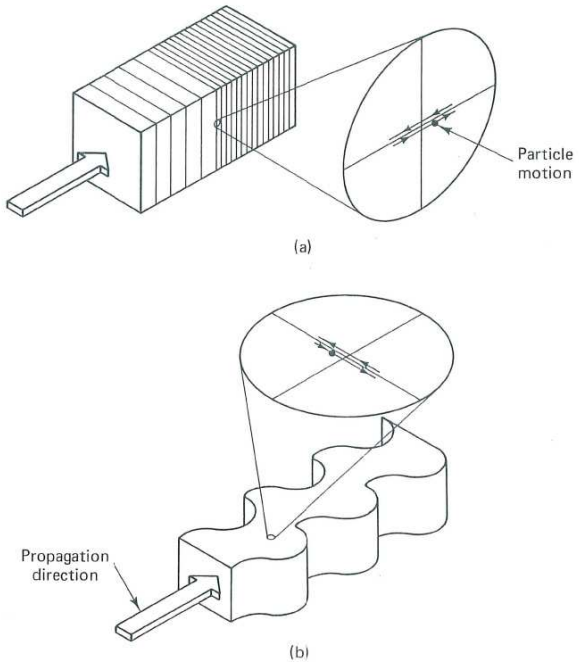

Figure 2.1: (a) P-wave. (b) S-wave. Taken from Dowding (1985).

where M is constrained modulus, μ is shear modulus and ρ is density[1].

Material		P-wave velocity, c_P [m/s]	S-wave velocity, c_S [m/s]
Clay, silt	Dry	100-600	40-300
	Water saturated	1450	40-250
Sand, gravel	Dry	150-1000	100-500
	Water saturated	1450	80-450
Till	Dry	600-1500	300-750
	Water saturated	1400-2000	250-700
Granite, gneiss		3500-7000	1700-3500

Table 2.1: Typical values of propagation velocities for different types of soil. Reproduced from Bodare (1997).

2.2 Wave propagation in rock mass

In elastic analysis, the material is often assumed to be infinite (or semi-infinite), linear elastic, continuous and isotropic. Rock mass is usually none of the above but these

[1]See Appendix A.1 for a summary of conversion formulas for elastic and dynamic properties.

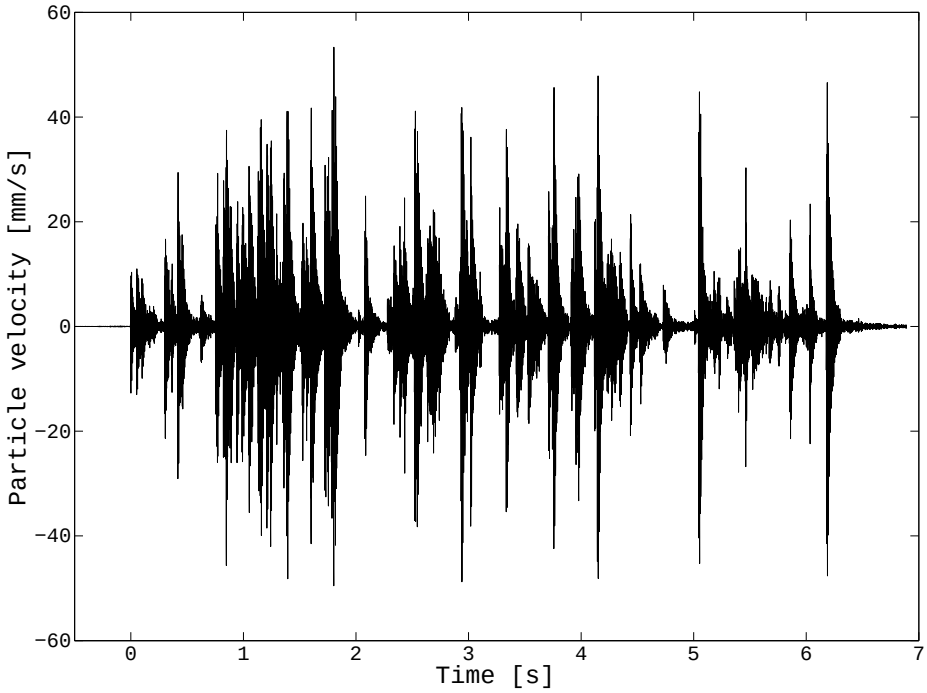

Figure 2.2: An example of measured particle velocity history from tunnel blasting.

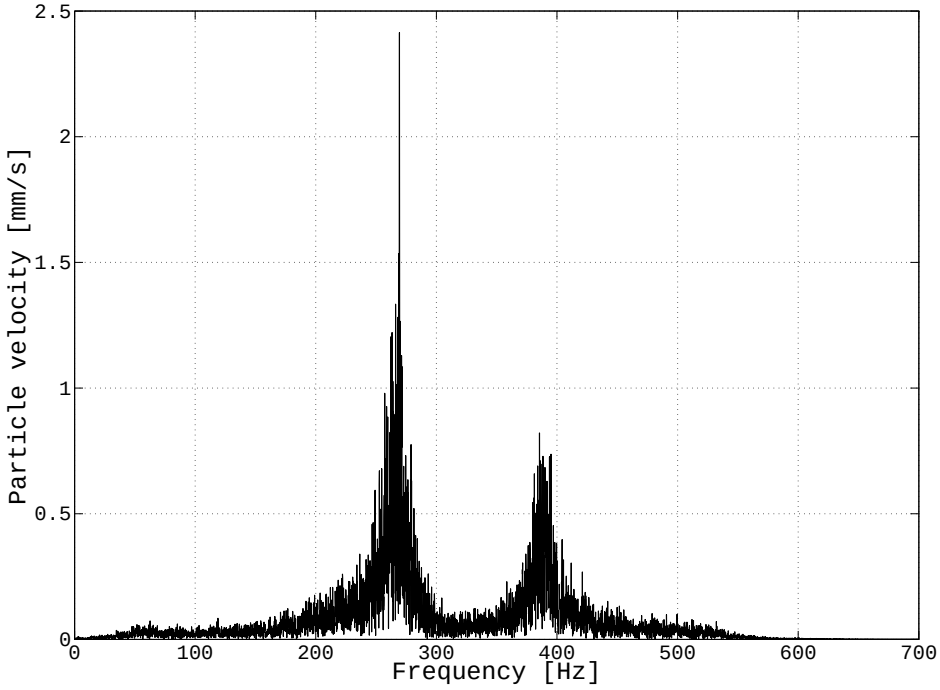

Figure 2.3: Frequency spectrum of the above blast signal.

assumptions can be valid for deep tunnels subjected to small strains (e.g. blast load). One of the most difficult parameters to consider when defining rock mass is joints since they are very site-specific and affect the direction and characteristics of waves. A P-wave propagating in a jointed rock mass attenuates faster than one in continuous rock. Both amplitude and frequency of the particle velocity is decreased. A rock joint can be considered as a low-pass filter, filtering out components with wavelengths smaller that the joint separation (Wu et al., 1998; Hao et al., 2000). The wave is also refracted, resulting in a change in direction. Due to the complexity in modeling the true behavior of a wave propagating in a jointed rock mass and the difficulty in determining site specific joint parameters such as quantity, characteristics and orientation, this study will analyze only the case of intact rock.

2.3 Reflection of body waves

There exist many aspects of reflection of body waves. This section will only consider waves in a semi-infinite halfspace reflected on a free surface. Even though this thesis mainly deals with cavities, it will be proven useful to make the analogy to a plane surface. The separation of the problem into SH and PSV components (which is described in the following section) is valid also for cavities and the double amplitude amplification will be proven valid for waves with high frequency reflected on a cavity.

2.3.1 SH- and PSV-problems

When either a P-wave or an S-wave is reflected on a free surface, both P-waves and S-waves are generated and propagate back into the material from where the incoming wave originates. Usually, vibrations contain both P- and S-waves. To simplify calculations (for reasons described below), it is convenient to divide the particle motion for the incoming and scattered waves into three components, one P-wave component and two S-wave components. Usually, dynamic mathematical analysis of wave propagation in geomaterials is conducted in a semi-infinite halfspace with a free surface on which waves are reflected or in an infinite fullspace with a cavity acting as the reflecting surface. The geometry of these problems is commonly defined with both the normal to the plane of reflection and the direction of propagation for the incoming wave oriented in the xy-plane. An example of this is shown in Figure 2.4. In this case, the S-wave component lying within the horizontal plane is denoted SH-wave (horizontal S-wave) and the S-wave component lying within the vertical plane is denoted SV-wave (vertical S-wave). The reason for this separation is that mathematical analysis shows that:

- Reflection of P-waves generate both P-waves and SV-waves.
- Reflection of SV-waves generate both P-waves and SV-waves.
- Reflection of SH-waves generate only SH-waves.

Thus, reflection of SH-waves can be treated separately. Hence, the problem is commonly divided into the SH-problem and the PSV-problem.

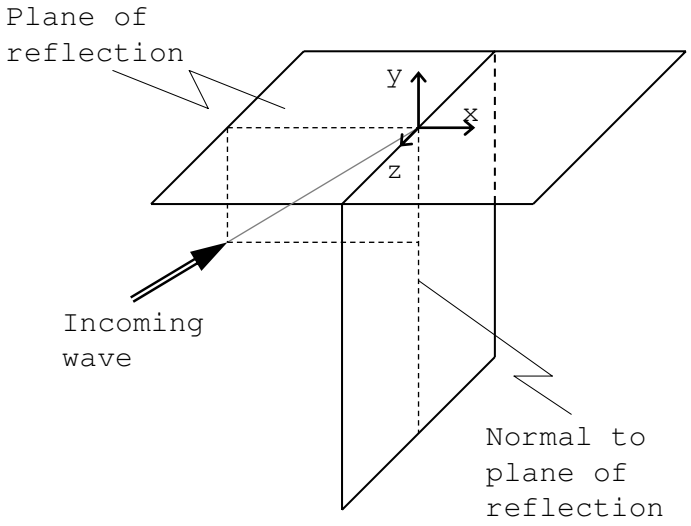

Figure 2.4: Example of wave and reflection plane orientations for a semi-infinite halfspace.

A definition of the different components for a wave propagating along the x-axis toward a plane of reflection having a normal lying in the xy-plane is shown in Figure 2.5. When the normal to the plane of reflection or the direction of wave propagation is not oriented in the xy-plane, these are still denoted SH-wave and SV-wave but the components of particle motion do not necessarily lie within the horizontal and vertical planes as above. If, for example, the normal still lies within the xy-plane but the wave is propagating in the xz-plane, the SH-component becomes vertical and the SV-component becomes horizontal. In such cases, these denotions can be quite confusing but they are the definitions generally used in dynamic analysis and are therefore adopted in this study as well.

Generally, the SH-wave can be defined as the component of shear wave particle motion which is parallel to the plane of reflection and the SV-wave can be defined as the component perpendicular to the SH-component. It shall be noted that the directions of particle motion which define the SH and SV-waves depend on both the direction of propagation and the orientation of the reflecting surface.

2.3.2 Amplification on a free surface

When a compressional plane wave is reflected on a free surface, the particle velocity amplitude at the surface is doubled. It can easiest be understood by considering the

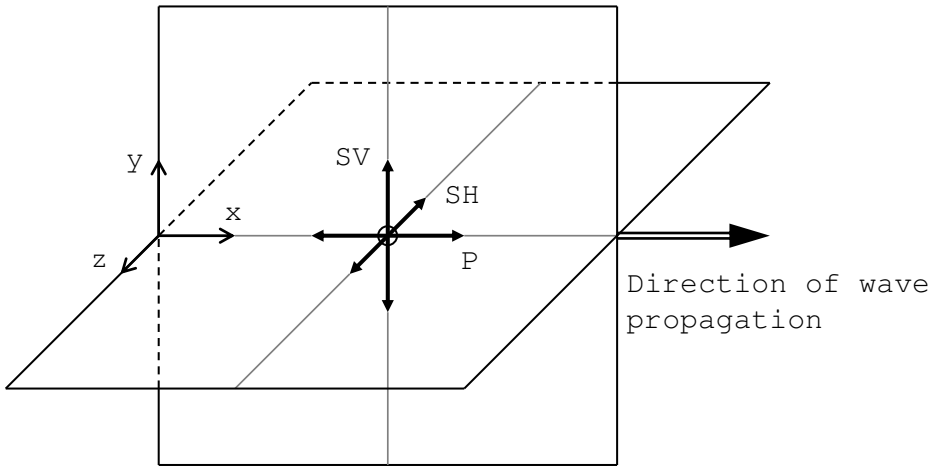

Figure 2.5: Definition of P, SH and SV-components of a wave propagating along the x-axis.

analogy of a longitunal wave traveling through a thin rod. If the end is fixed, as shown in Figure 2.6a, the part of the wave not yet reflected collides with the reflected part and thereby adding the stresses together. This causes the stress amplitude to be doubled and the particle velocity to become zero. When the end is free (analogous with a plane wave reflected on a free surface), as shown in Figure 2.6b, the compressive stress must be zero at the free end since there can be no resisting forces. For the stress to be zero, the stress of the reflected part of the wave must be tensile and of equal size as the part not yet reflected, thus canceling out the stresses and doubling the velocity.

2.4 Harmonic waves

The most important properties of a vibrational signal are frequency, particle displacement, particle velocity and particle acceleration. If the waveform is sinusoidal, the particle displacement of a plane wave propagating in the x-direction can be expressed as

$$u(x,t) = u_0 e^{i(kx-\omega t)}, \tag{2.3}$$

where u_0 is the displacement amplitude, k is the wave number and ω is the circular frequency, related to frequency f by

$$\omega = 2\pi f. \tag{2.4}$$

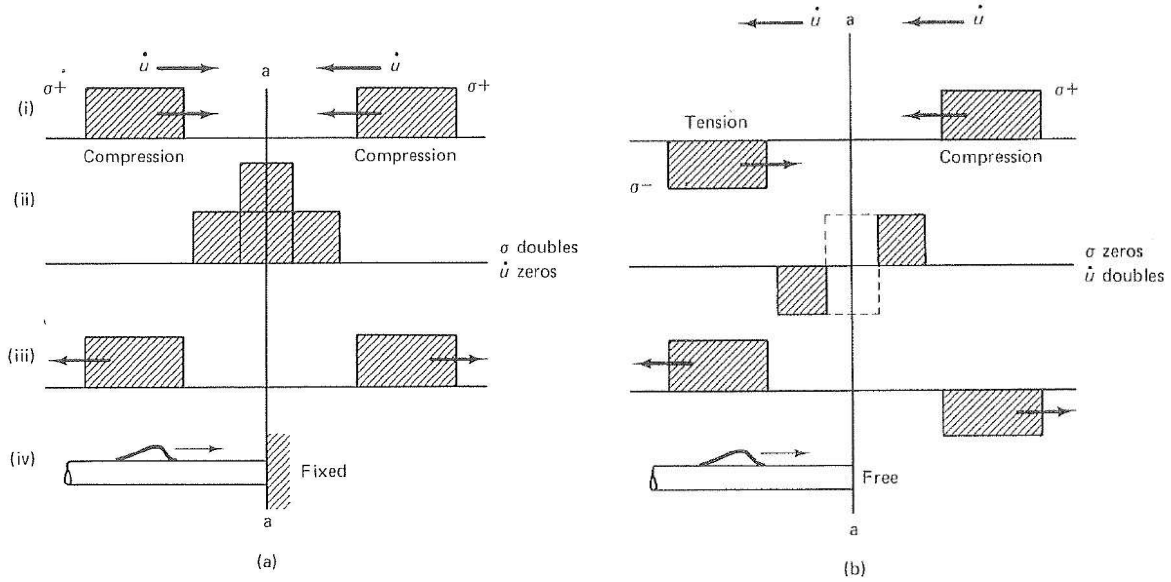

Figure 2.6: Reflection of longitunal waves in a thin rod: (a) Fixed end. (b) Free end. Taken from Dowding (1985).

The wavenumber is defined as

$$k = \frac{2\pi}{\lambda}, \tag{2.5}$$

where λ is wavelength. The velocity and acceleration can then be expressed as[2]

$$\dot{u}(x,t) = \frac{\partial}{\partial t}u(x,t) = -i\omega u(x,t), \tag{2.6}$$

$$\ddot{u}(x,t) = \frac{\partial^2}{\partial x^2}u(x,t) = \omega^2 u(x,t), \tag{2.7}$$

which means that if the frequency and one of the parameters above are known, the remaining parameters can be obtained by Equations (2.6) and (2.7). For real blast signals (non-sinusoidal waveforms), the conversion is usually done by numerical differentiation or integration but can be approximated by Equations (2.6) and (2.7). Another important feature is that if the amplitude of u, $\dot{u}$ or $\ddot{u}$ is known for two different points, A and B, and the frequency is constant then

$$\left|\frac{u_A}{u_B}\right| = \left|\frac{\dot{u}_A}{\dot{u}_B}\right| = \left|\frac{\ddot{u}_A}{\ddot{u}_B}\right| \tag{2.8}$$

so that, for example, doubling the displacement amplitude implies that the velocity and acceleration amplitudes are also doubled.

A harmonic wave can also be expressed in terms of the displacement potential,

$$\varphi(x,t) = \varphi_0 e^{i(k_P x - \omega t)}, \tag{2.9}$$

$$\psi(x,t) = \psi_0 e^{i(k_S x - \omega t)}, \tag{2.10}$$

[2]Note velocity is also denoted v in this report but acceleration is not denoted a since it is reserved for tunnel radius.

where φ is the displacement potential of a P-wave, ψ is the displacement potential of an S-wave, φ_0 and ψ_0 are their respective amplitudes, k_P is the compressional wave number and k_S is the shear wave number. If only one of the waves is present, then the displacement is obtained by

$$u(x,t) = \frac{\partial}{\partial x}\varphi(x,t) = ik_P\varphi(x,t) \tag{2.11}$$

or

$$u(x,t) = \frac{\partial}{\partial x}\psi(x,t) = ik_S\psi(x,t). \tag{2.12}$$

If both the P- and S-waves are present the displacement is obtained by adding the gradient of φ and the rotation of Ψ,

$$\mathbf{u} = \nabla\varphi + \nabla \times \Psi, \tag{2.13}$$

where $\mathbf{u}$ and Ψ are the vector forms of displacement and S-wave displacement potential,

$$\mathbf{u} = (u_x, u_y, u_z) \tag{2.14}$$
$$\Psi = (\psi_x, \psi_y, \psi_z) \tag{2.15}$$

in cartesian coordinates or

$$\mathbf{u} = (u_r, u_\theta, u_z) \tag{2.16}$$
$$\Psi = (\psi_r, \psi_\theta, \psi_z) \tag{2.17}$$

in cylindrical coordinates.

2.5 Dynamic stress

One way of calculating the compressive dynamic stress in an elastic medium, induced by a propagating plane P-wave, is by using the impedance, which is defined by

$$Z = \rho\, c_P, \tag{2.18}$$

where ρ is density and c_P is P-wave propagation velocity. The compressive stress in the direction of wave propagation can then be calculated by the simple relationship

$$\sigma = Z\, v, \tag{2.19}$$

where v is the particle velocity[3]. This relationship can be derived from the expression for strain, induced by a plane P-wave,

$$\varepsilon = \frac{v}{c_P}. \tag{2.20}$$

By using Hooke's law, Equation 2.1, elastic conversion formulas (see Appendix A.1) and the fact that the strain caused by a plane wave is non-zero in only one direction so that the volumetric strain is $\varepsilon_{vol} = \varepsilon$, we obtain

$$\sigma = \lambda\varepsilon_{vol} + 2\mu\varepsilon = M\varepsilon = \rho\, c_P\, v, \tag{2.21}$$

where λ and μ are Lamé constants and M is constrained modulus. For derivation of Equation (2.20), see Bodare (1997) or Yang and Scovira (2007).

[3]Since the wave is a plane P-wave, the direction of the particle velocity is in the direction of wave propagation.

2.6 Bessel functions

In problems stated in cylindrical coordinates, differential equations of the form

$$x^2\frac{d^2y}{dx^2} + x\frac{dy}{dx} + (x^2 - n^2)y = 0 \tag{2.22}$$

are commonly encountered. This is called Bessel's differential equation of order n and has a solution of

$$y(x) = C_1 J_n(x) + C_2 Y_n(x), \tag{2.23}$$

where C_1 and C_2 are constants and $J_n(x)$ and $Y_n(x)$ are the n:th order Bessel functions of the first and second kind, respectively. The solution can also be expressed in terms of the Hankel functions, as

$$y(x) = C_1 H_n^{(1)}(x) + C_2 H_n^{(2)}(x), \tag{2.24}$$

where $H_n^{(1)}(x)$ and $H_n^{(2)}(x)$ are the Hankel functions of the first and second kind respectively and are related to the Bessel functions by

$$H_n^{(1)}(x) = J_n(x) + iY_n(x), \tag{2.25}$$

$$H_n^{(2)}(x) = J_n(x) - iY_n(x). \tag{2.26}$$

The damped oscillating behavior of the Bessel functions is shown in Figure 2.7 for order zero and one.

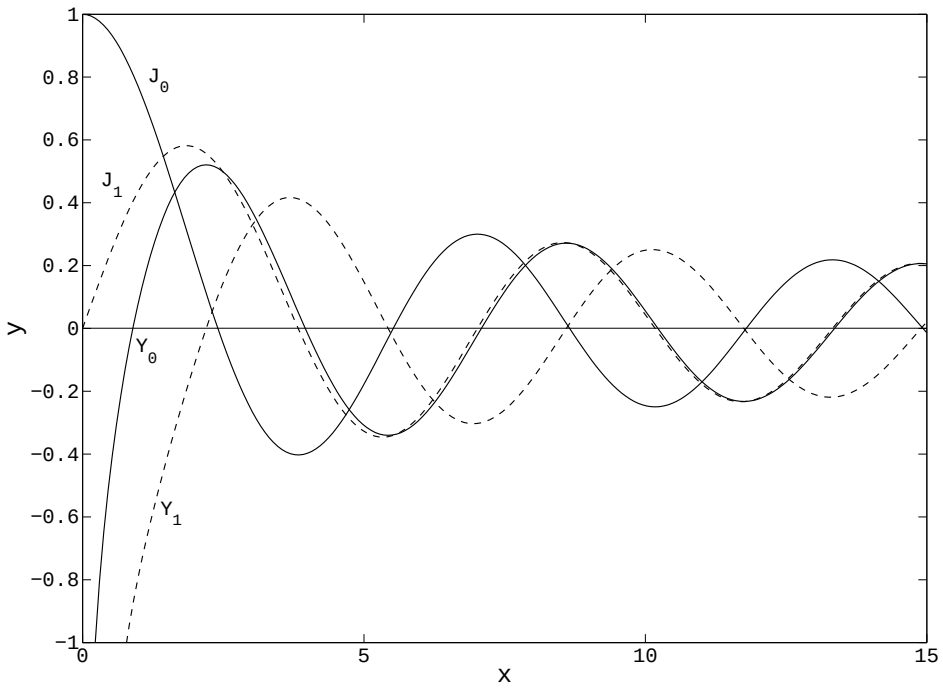

Figure 2.7: Bessel functions of order zero and one: $J_0(x), J_1(x), Y_0(x), Y_1(x)$.

3 ANALYTICAL SOLUTIONS

Reflection of elastic waves on a cavity is complex to analyze mathematically. The problem has therefore been idealized to a cylindrical cavity in an infinite linear elastic material subjected to a plane sinusoidal wave. The transient response of the cavity is beyond the scope of this study, i.e. only steady state has been examined. The analyses in this section are to a large extent based on the comprehensive work by Mow and Pao (1971), though some expressions contained inaccuracies and were therefore derived separately.

The most interesting problem to analyze is reflection of P-waves, since blast-induced vibrations mostly consist of P-waves. Due to the much simpler nature of the SH-problem[1], it has been evaluated briefly for enhancing the understanding of the problem. Reflection of SV-waves is left out because it is very similar to reflection of P-waves and is not applicable for blast vibrations.

3.1 Input parameters

Both cartesian and cylindrical coordinate systems are used in this report and are defined in Figure 3.1. The incoming wave is always propagating in the x-direction and the angle θ is measured from that direction. The radial coordinate is denoted r and is measured from the center of the cavity. The tunnel radius is denoted a so that the tunnel circumference is located at $r = a$. For those calculations where the tunnel radius has to be specified, $a = 5$ m is generally applied.

Since only two deformation parameters of an elastic material are independent, only two have to be specified and the rest can be derived. Typical values of elastic modulus and Poisson's ratio for intact rock mass are assumed in this study (Stille et al., 2004),

$$\begin{aligned} E &= 60\,\text{GPa}, \\ \nu &= 0.25. \end{aligned}$$

Using the conversion formulas in Appendix A.1, the remaining deformation parameters

[1] See Section 2.3.1 for explanation of the SH- and PSV-problems.

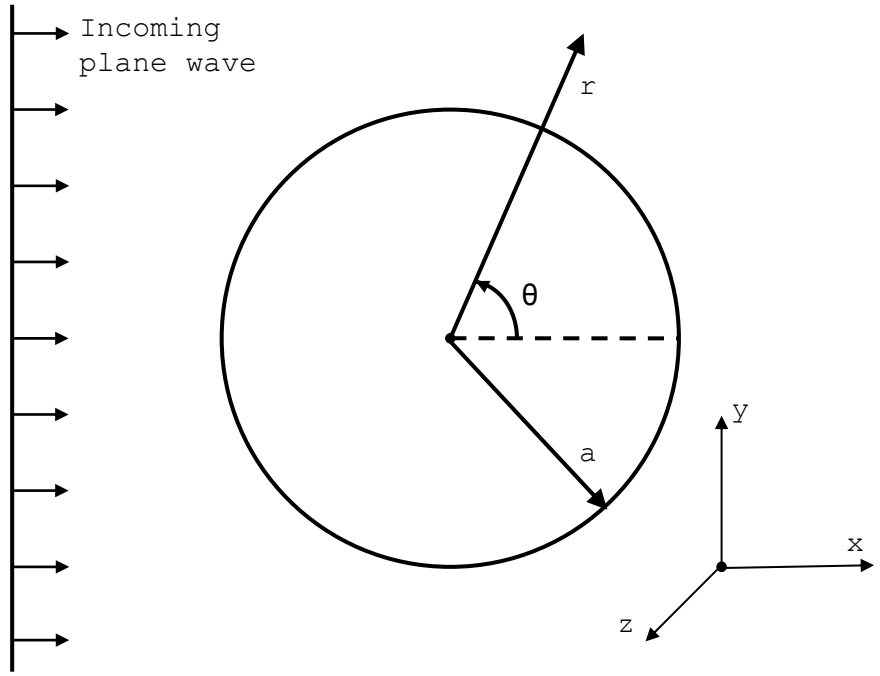

Figure 3.1: Definition of cartesian and cylindrical coordinates.

become

$$\begin{aligned} \lambda &= 24\,\text{GPa}, \\ \mu &= 24\,\text{GPa}, \\ K &= 40\,\text{GPa}, \\ M &= 72\,\text{GPa}, \end{aligned}$$

where λ and μ are Lamé constants (μ is equivalent with shear modulus), K is bulk modulus and M is constrained modulus (oedometer modulus). By specifying the density $\rho = 2600$ kg/m^3 and using the equations

$$M = \rho c_P^2, \tag{3.1}$$
$$\mu = \rho c_S^2, \tag{3.2}$$

the P- and S-wave velocities become

$$\begin{aligned} c_P &\approx 5262\,\text{m/s}, \\ c_S &\approx 3038\,\text{m/s}. \end{aligned}$$

By Equation (2.18), the impedance becomes

$$Z \approx 13.6 \cdot 10^6\,\text{Pa·s/m}.$$

In those analyses where vibration parameters have to be specified, they have been chosen to resemble those of blast-induced vibrations. The particle velocity 0.1 m/s is generally applied and the frequency ranges between 0-1000 Hz.

3.2 Dynamic response to SH-waves of a cylindrical cavity

As mentioned in Section 2.3, incident SH-waves generate only SH-waves when reflected and can therefore be treated separately from the P- and SV-waves. When an elastic material is subjected to multiple body waves, the total particle displacement at any point is obtained by superposition. Thus, the displacement of the incoming and scattered waves can be superimposed as

$$w = w^{(i)} + w^{(s)}, \tag{3.3}$$

where $w^{(i)}$, $w^{(s)}$ and w are the incoming, scattered and total displacements, respectively. Mow and Pao (1971) formulated the steady state solution for reflection of a plane SH-wave on a circular cylindrical cavity of infinite length in an elastic fullspace as

$$w^{(i)} = w_0 \sum_{n=0}^{\infty} \epsilon_n i^n J_n(kr) \cos(n\theta) e^{-i\omega t}, \tag{3.4}$$

$$w^{(s)} = w_0 \sum_{n=0}^{\infty} A_n H_n^{(1)}(kr) \cos(n\theta) e^{-i\omega t}, \tag{3.5}$$

where w_0 is the displacement amplitude of the incident wave,

$$\epsilon_n = \begin{cases} 1 & \text{if } n = 0, \\ 2 & \text{if } n > 0, \end{cases} \tag{3.6}$$

J_n and H_n are Bessel and Hankel functions (see section 2.6), k is the wave number, defined by

$$k = \frac{2\pi}{\lambda}, \tag{3.7}$$

λ is the wavelength of the incoming wave, r is the radial coordinate, θ is the angular coordinate (measured from the direction of wave propagation), A_n is a constant given by

$$A_n = -\epsilon_n i^n \frac{nJ_n(ka) - kaJ_{n+1}(ka)}{nH_n^{(1)}(ka) - kaH_{n+1}^{(1)}(ka)}, \tag{3.8}$$

ω is the circular frequency of the incoming wave and a is the tunnel radius.

3.2.1 Evaluation

Using Equations (3.3) through (3.8) to evaluate the displacement[2] at the cavity surface closest to the incoming wave (i.e. at $r = a$, $\theta = \pi$) and normalizing the wave number by the tunnel diameter, so that

$$kr = ka = \frac{\pi}{\left(\frac{\lambda}{2a}\right)}, \tag{3.9}$$

[2]The displacement induced by an SH-wave is exclusively in the z-direction.

the relationship between normalized wavelength and displacement amplitude amplification can be obtained numerically. The result is shown in Figure 3.2. It can be observed that the maximum displacement amplitude occurs very close to where the normalized wavelength equals one, i.e. when the wavelength almost equals the diameter of the cavity. The amplification at resonance is approximately 2.2. By plotting the displacement amplitude as a function of ka/π in a linear scale, as shown in Figure 3.3, it is obvious that the peaks occur at multiples of one. This implies that a circular cylindrical cavity in the SH-case has resonance frequencies where the wave number multiplied by the tunnel radius equals multiples of π, i.e.

$$k_r = \frac{n\pi}{a}, \qquad n = 1, 2, 3, ... \tag{3.10}$$

and hence the wavelength at resonance equals

$$\lambda_r = \frac{2a}{n}, \qquad n = 1, 2, 3, ... \tag{3.11}$$

In terms of circular frequency, the maximum displacement occurs at

$$\omega_r = c_S \frac{n\pi}{a}, \qquad n = 1, 2, 3, ... \tag{3.12}$$

which corresponds to the frequency

$$f_r = c_S \frac{n}{2a}, \qquad n = 1, 2, 3, ... \tag{3.13}$$

It is seen in Figure 3.2 that w/w_0 tends to unity as λ increases, i.e. that the total displacement for longer wavelengths (low frequencies) is equal to the displacement of the incident wave. This can also be shown mathematically by using Equations (2.25), (2.26) and the asymptotic relationships for Bessel functions as the argument tends to zero (Råde and Westergren, 2004). For $x \to 0^+$,

$$J_n(x) \sim \frac{1}{n!}\left(\frac{x}{2}\right)^n \tag{3.14}$$

$$Y_0(x) \sim \frac{2}{\pi}\ln(x) \tag{3.15}$$

$$Y_n(x) \sim -\frac{(n-1)!}{\pi}\left(\frac{2}{x}\right)^n, n > 0, \tag{3.16}$$

so that for $\lambda \to \infty$, i.e. $k \to 0^+$,

$$\lim_{k \to 0^+} w = w_0. \tag{3.17}$$

This result is expected since hardly any reflection should take place when the diameter of the cavity is very small compared to the wavelength.

Regarding the behavior at the opposite limit, i.e. as the wavelength tends to zero (the frequency tends to infinity), it would be expected that the wave behaves as if reflected on a free planar surface since $r/\lambda \to \infty$ when $\lambda \to 0$. This implies that the displacement amplitude at the free surface would be theoretically doubled as discussed in Section 2.3. Even though not mathematically proven, it appears from Figures 3.2 and 3.3 as if though the normalized displacement either converges toward two or oscillates around two.

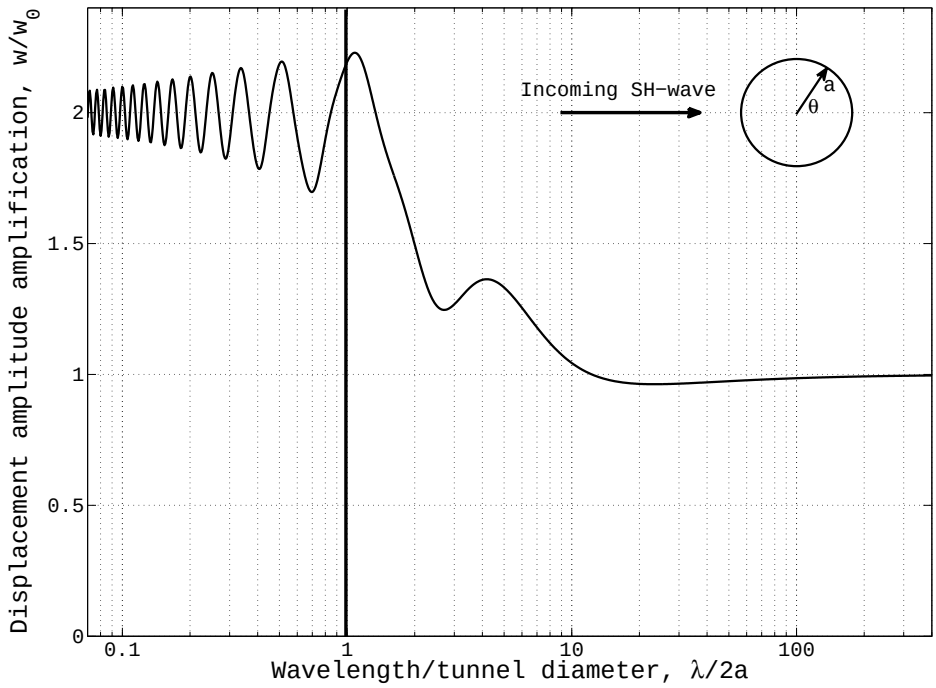

Figure 3.2: Displacement amplitude amplification at $r = a$ and $\theta = \pi$ for reflection of SH-waves.

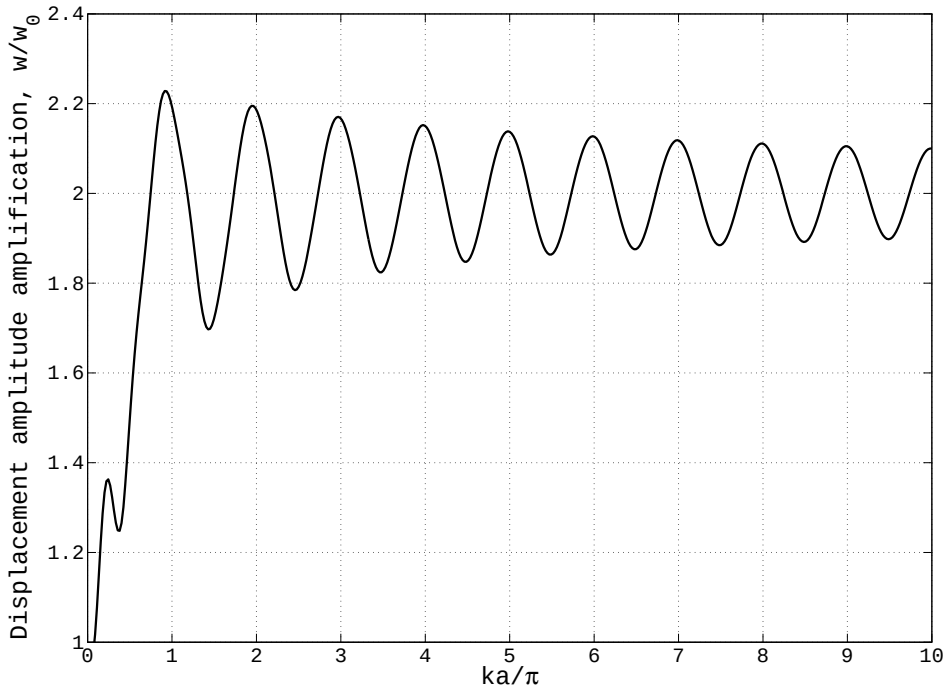

Figure 3.3: Displacement amplitude amplification at $r = a$ and $\theta = \pi$ as a function of wave number.

The figures above describe the amplification at $\theta = \pi$ (the point closest to the incident wave front). At $\theta = \pi/2$ and $\theta = 0$ the maximum amplifications are 1.75 and 1.4, respectively.

3.3 Dynamic response to P-waves of a cylindrical cavity

Reflection of P-waves, i.e. the PSV-problem, is more complex than the SH-problem as both P-waves and SV-waves are generated (see Section 2.3) but is more interesting for blasting issues since P-waves are predominant in blast-induced vibrations. As with the SH-problem, all waves can be superposed so that the total particle displacement potential, displacement, velocity or acceleration is the sum of the incoming P-wave, the reflected P-wave and the reflected SV-wave. The displacement potentials are given by Mow and Pao (1971) as

$$\varphi = \sum_{n=0}^{\infty} \left[\varphi_0 \epsilon_n i^n J_n(k_P r) + A_n H_n^{(1)}(k_P r)\right] \cos(n\theta) e^{-i\omega t}, \tag{3.18}$$

$$\psi = \sum_{n=0}^{\infty} B_n H_n^{(1)}(k_S r) \sin(n\theta) e^{-i\omega t}, \tag{3.19}$$

where φ is sum of the displacement potentials of the incoming and scattered P-waves, ψ is the displacement potential of the SV-wave, φ_0 is the displacement potential amplitude of the incident wave,

$$\epsilon_n = \begin{cases} 1 & \text{if } n = 0, \\ 2 & \text{if } n > 0, \end{cases} \tag{3.20}$$

J_n and H_n are Bessel and Hankel functions (see Section 2.6), k_P and k_S are the P- and S-wave numbers respectively, ω is the circular frequency and A_n and B_n are constants.

To find A_n and B_n, the boundary conditions

$$\sigma_{rr}|_{r=a} = 0 \tag{3.21}$$

and

$$\tau_{r\theta}|_{r=a} = 0 \tag{3.22}$$

must be applied. Examining the expression for the dynamic stress concentration factor in Mow and Pao (1971) and its behavior as the frequency tends to zero, there is a discrepancy between the actual limit and the one stated in the report, i.e. the static solution is not obtained as claimed therein. Solving the equations for tangential stress and dynamic stress concentration factor numerically, the result supports the assumption that some mistake has been made in their report. The mistake is still not corrected in the later edition (Pao and Mow, 1973). It is concluded that the expressions for the coefficients A_n and B_n in Mow and Pao (1971) are incorrect and have therefore been recalculated herein. The results are presented in the following section.

3.3.1 Closed-form solution

The particle displacement is obtained by

$$\mathbf{u} = \nabla\varphi + \nabla \times \Psi, \tag{3.23}$$

where $\mathbf{u}$ and Ψ are the vector forms of displacement and SV-potential. The gradient of φ is given by

$$\nabla\varphi = \frac{\partial\varphi}{\partial r}\mathbf{e}_r + \frac{1}{r}\frac{\partial\varphi}{\partial\theta}\mathbf{e}_\theta + \frac{\partial\varphi}{\partial z}\mathbf{e}_z, \tag{3.24}$$

where $\mathbf{e}_r$, $\mathbf{e}_\theta$ and $\mathbf{e}_z$ are the unit vectors in the r, θ and z directions respectively. The rotation of Ψ is given by

$$\nabla \times \Psi = \begin{bmatrix} \mathbf{e}_r & \mathbf{e}_\theta & \mathbf{e}_z \\ \frac{\partial}{\partial r} & \frac{1}{r}\frac{\partial}{\partial\theta} & \frac{\partial}{\partial z} \\ \psi_r & \psi_\theta & \psi_z \end{bmatrix} \tag{3.25}$$

Since $\psi_r = 0$ and $\psi_\theta = 0$, the vector Ψ becomes the scalar ψ and

$$\nabla \times \Psi = \frac{1}{r}\frac{\partial\psi}{\partial\theta}\mathbf{e}_r - \frac{\partial\psi}{\partial r}\mathbf{e}_\theta. \tag{3.26}$$

The plain strain condition implies that $\frac{\partial\varphi}{\partial z} = 0$, which yields

$$\nabla\varphi = \frac{\partial\varphi}{\partial r}\mathbf{e}_r + \frac{1}{r}\frac{\partial\varphi}{\partial\theta}\mathbf{e}_\theta. \tag{3.27}$$

Hence, the radial and tangential displacements become

$$u_r = \frac{\partial\varphi}{\partial r} + \frac{1}{r}\frac{\partial\psi}{\partial\theta}, \tag{3.28}$$

$$u_\theta = \frac{1}{r}\frac{\partial\varphi}{\partial\theta} - \frac{\partial\psi}{\partial r}. \tag{3.29}$$

The strains are given by

$$\varepsilon_{rr} = \frac{\partial u_r}{\partial r}, \tag{3.30}$$

$$\varepsilon_{\theta\theta} = \frac{1}{r}\frac{\partial u_\theta}{\partial\theta} + \frac{u_r}{r}, \tag{3.31}$$

$$\varepsilon_{zz} = \frac{\partial u_z}{\partial z}, \tag{3.32}$$

$$\varepsilon_{r\theta} = \frac{1}{2}\left(\frac{1}{r}\frac{\partial u_r}{\partial\theta} + \frac{\partial u_\theta}{\partial r} - \frac{u_\theta}{r}\right), \tag{3.33}$$

$$\varepsilon_{rz} = \frac{1}{2}\left(\frac{\partial u_z}{\partial r} + \frac{\partial u_r}{\partial z}\right), \tag{3.34}$$

$$\varepsilon_{\theta z} = \frac{1}{2}\left(\frac{\partial u_\theta}{\partial z} + \frac{1}{r}\frac{\partial u_z}{\partial\theta}\right), \tag{3.35}$$

where ε_{zz}, ε_{rz} and $\varepsilon_{\theta z}$ are equal to zero because of the plain strain condition. The stresses are obtained by Hooke's law,

$$\sigma_{rr} = \lambda\left(\varepsilon_{rr}+\varepsilon_{\theta\theta}+\varepsilon_{zz}\right)+2\mu\varepsilon_{rr}, \tag{3.36}$$

$$\sigma_{\theta\theta} = \lambda\left(\varepsilon_{rr}+\varepsilon_{\theta\theta}+\varepsilon_{zz}\right)+2\mu\varepsilon_{\theta\theta}, \tag{3.37}$$

$$\tau_{r\theta} = 2\mu\varepsilon_{r\theta}, \tag{3.38}$$

where λ and μ are the Lamé constants[3]. Since $\cos(n\theta)$ and $\sin(n\theta)$ are present in the infinite series and the boundary conditions in Equations (3.21) and (3.22) must be valid for all θ, each term in the series must equal zero. Solving the above equations yields

$$A_n = -\varphi_0\epsilon_n i^n\frac{\alpha_n^{(1)}}{\alpha_n^{(2)}} \tag{3.39}$$

and

$$B_n = 2nk_P\varphi_0\epsilon_n i^n\frac{\beta_n^{(1)}}{\beta_n^{(2)}}, \tag{3.40}$$

where

$$\begin{aligned}\alpha_n^{(1)} = {} & 4k_P n^3 H_n^{(1)}(k_S a)\mu J_{n+1}(k_P a)+4J_n(k_P a)n^3\mu H_{n+1}^{(1)}(k_S a)k_S \\ & -2n^2 J_n(k_P a)a\lambda k_P^2 H_n^{(1)}(k_S a)-2n^2 J_n(k_P a)a\mu k_S^2 H_n^{(1)}(k_S a) \\ & -4n^2 J_n(k_P a)a\mu k_P^2 H_n^{(1)}(k_S a)-4k_P H_{n+1}^{(1)}(k_S a)k_S a\mu n^2 J_{n+1}(k_P a) \\ & +2J_n(k_P a)a\lambda k_P^2 n H_n^{(1)}(k_S a)+4J_n(k_P a)a\mu k_P^2 n H_n^{(1)}(k_S a) \\ & -4k_P n H_n^{(1)}(k_S a)\mu J_{n+1}(k_P a)+2J_n(k_P a)a\mu n k_S^2 H_n^{(1)}(k_S a) \\ & -4J_n(k_P a)\mu n H_{n+1}^{(1)}(k_S a)k_S-2J_n(k_P a)a^2\lambda k_P^2 H_{n+1}^{(1)}(k_S a)k_S \\ & -4J_n(k_P a)a^2\mu k_P^2 H_{n+1}^{(1)}(k_S a)k_S+J_n(k_P a)a^3\lambda k_P^2 k_S^2 H_n^{(1)}(k_S a) \\ & +2J_n(k_P a)a^3\mu k_P^2 k_S^2 H_n^{(1)}(k_S a)-2k_P k_S^2 a^2 H_n^{(1)}(k_S a)\mu J_{n+1}(k_P a) \\ & +4k_P H_{n+1}^{(1)}(k_S a)k_S a\mu J_{n+1}(k_P a),\end{aligned} \tag{3.41}$$

$$\begin{aligned}\alpha_n^{(2)} = {} & -2a^2\mu H_{n+1}^{(1)}(k_P a)k_P k_S^2 H_n^{(1)}(k_S a)-4\mu H_{n+1}^{(1)}(k_P a)k_P n H_n^{(1)}(k_S a) \\ & -2a^2\lambda k_P^2 H_n^{(1)}(k_P a)H_{n+1}^{(1)}(k_S a)k_S+2a\mu n H_n^{(1)}(k_P a)k_S^2 H_n^{(1)}(k_S a) \\ & -4\mu n H_n^{(1)}(k_P a)H_{n+1}^{(1)}(k_S a)k_S+4n^3 H_n^{(1)}(k_P a)\mu H_{n+1}^{(1)}(k_S a)k_S \\ & -4an^2 H_{n+1}^{(1)}(k_P a)k_P\mu H_{n+1}^{(1)}(k_S a)k_S-2a\mu n^2 H_n^{(1)}(k_P a)k_S^2 H_n^{(1)}(k_S a) \\ & -4a\mu k_P^2 H_n^{(1)}(k_P a)n^2 H_n^{(1)}(k_S a)+2a\lambda k_P^2 H_n^{(1)}(k_P a)n H_n^{(1)}(k_S a) \\ & +4a\mu H_{n+1}^{(1)}(k_P a)k_P H_{n+1}^{(1)}(k_S a)k_S-2a\lambda k_P^2 H_n^{(1)}(k_P a)n^2 H_n^{(1)}(k_S a) \\ & -4a^2\mu k_P^2 H_n^{(1)}(k_P a)H_{n+1}^{(1)}(k_S a)k_S+4n^3 H_{n+1}^{(1)}(k_P a)k_P\mu H_n^{(1)}(k_S a) \\ & +a^3\lambda k_P^2 H_n^{(1)}(k_P a)k_S^2 H_n^{(1)}(k_S a)+2a^3\mu k_P^2 H_n^{(1)}(k_P a)k_S^2 H_n^{(1)}(k_S a) \\ & +4a\mu k_P^2 H_n^{(1)}(k_P a)n H_n^{(1)}(k_S a),\end{aligned} \tag{3.42}$$

[3] μ is equivalent with shear modulus, see Appendix A.1.

$$\begin{aligned}\beta_n^{(1)} &= -2n^2 H_{n+1}^{(1)}(k_P a)\mu J_n(k_P a) + a^2 H_{n+1}^{(1)}(k_P a)k_P^2\lambda J_n(k_P a) \\ &\quad -2H_n^{(1)}(k_P a)\mu J_{n+1}(k_P a) + 2\mu n^2 H_n^{(1)}(k_P a)J_{n+1}(k_P a) \\ &\quad -a^2\lambda k_P^2 H_n^{(1)}(k_P a)J_{n+1}(k_P a) + 2\mu H_{n+1}^{(1)}(k_P a)J_n(k_P a) \\ &\quad +2a^2 H_{n+1}^{(1)}(k_P a)k_P^2\mu J_n(k_P a) - 2a^2\mu k_P^2 H_n^{(1)}(k_P a)J_{n+1}(k_P a)\end{aligned} \tag{3.43}$$

and

$$\begin{aligned}\beta_n^{(2)} &= -2a^2\mu H_{n+1}^{(1)}(k_P a)k_P k_S^2 H_n^{(1)}(k_S a) - 4\mu H_{n+1}^{(1)}(k_P a)k_P n H_n^{(1)}(k_S a) \\ &\quad -2a^2\lambda k_P^2 H_n^{(1)}(k_P a)H_{n+1}^{(1)}(k_S a)k_S + 2a\mu n H_n^{(1)}(k_P a)k_S^2 H_n^{(1)}(k_S a) \\ &\quad -4\mu n H_n^{(1)}(k_P a)H_{n+1}^{(1)}(k_S a)k_S + 4n^3 H_n^{(1)}(k_P a)\mu H_{n+1}^{(1)}(k_S a)k_S \\ &\quad -4an^2 H_{n+1}^{(1)}(k_P a)k_P\mu H_{n+1}^{(1)}(k_S a)k_S - 2a\mu n^2 H_n^{(1)}(k_P a)k_S^2 H_n^{(1)}(k_S a) \\ &\quad -4a\mu k_P^2 H_n^{(1)}(k_P a)n^2 H_n^{(1)}(k_S a) + 2a\lambda k_P^2 H_n^{(1)}(k_P a)n H_n^{(1)}(k_S a) \\ &\quad +4a\mu H_{n+1}^{(1)}(k_P a)k_P H_{n+1}^{(1)}(k_S a)k_S - 2a\lambda k_P^2 H_n^{(1)}(k_P a)n^2 H_n^{(1)}(k_S a) \\ &\quad -4a^2\mu k_P^2 H_n^{(1)}(k_P a)H_{n+1}^{(1)}(k_S a)k_S + 4n^3 H_{n+1}^{(1)}(k_P a)k_P\mu H_n^{(1)}(k_S a) \\ &\quad +a^3\lambda k_P^2 H_n^{(1)}(k_P a)k_S^2 H_n^{(1)}(k_S a) + 2a^3\mu k_P^2 H_n^{(1)}(k_P a)k_S^2 H_n^{(1)}(k_S a) \\ &\quad +4a\mu k_P^2 H_n^{(1)}(k_P a)n H_n^{(1)}(k_S a).\end{aligned} \tag{3.44}$$

The particle displacement amplitudes become

$$\begin{aligned}\hat{u}_r &= \sum_{n=0}^{\infty}\varphi_0\epsilon_n i^n\left(-J_{n+1}(k_P r) + \frac{nJ_n(k_P r)}{k_P r}\right)k_P\cos(n\theta) \\ &\quad +A_n\left(-H_{n+1}^{(1)}(k_P r) + \frac{nH_n^{(1)}(k_P r)}{k_P r}\right)k_P\cos(n\theta) \\ &\quad +B_n\frac{nH_n^{(1)}(k_S r)}{r}\cos(n\theta)\end{aligned} \tag{3.45}$$

and

$$\begin{aligned}\hat{u}_\theta &= \sum_{n=0}^{\infty} -\frac{\varphi_0\epsilon_n i^n J_n(k_P r) + A_n H_n^{(1)}(k_P r)}{r}n\sin(n\theta) \\ &\quad -B_n\left(-H_{n+1}^{(1)}(k_S r) + \frac{nH_n^{(1)}(k_S r)}{k_S r}\right)k_S\sin(n\theta),\end{aligned} \tag{3.46}$$

where $\hat{u}$ is the amplitude of u. Particle velocity amplitudes are obtained by multiplying the displacements by $-i\omega$,

$$\hat{v}_r = -i\omega\hat{u}_r, \tag{3.47}$$

$$\hat{v}_\theta = -i\omega\hat{u}_\theta, \tag{3.48}$$

as discussed in Section 2.4. Finally, the tangential stress becomes

$$\sigma_{\theta\theta} = -\frac{1}{r^2}\sum_{n=0}^{\infty} S_n\cos(n\theta), \tag{3.49}$$

where

$$\begin{aligned} S_n &= \lambda k_P^2 r^2 \varphi_0 \epsilon_n i^n J_n(k_P r) + \lambda k_P^2 r^2 A_n H_n^{(1)}(k_P r) \\ &\quad + 2\mu n^2 \varphi_0 \epsilon_n i^n J_n(k_P r) + 2\mu n^2 A_n H_n^{(1)}(k_P r) \\ &\quad - 2\mu n B_n H_{n+1}^{(1)}(k_S r) k_S r + 2\mu B_n n^2 H_n^{(1)}(k_S r) \\ &\quad + 2\mu \varphi_0 \epsilon_n i^n J_{n+1}(k_P r) k_P r - 2\mu n \varphi_0 \epsilon_n i^n J_n(k_P r) \\ &\quad + 2\mu A_n H_{n+1}^{(1)}(k_P r) k_P r - 2\mu n A_n H_n^{(1)}(k_P r) \\ &\quad - 2\mu B_n n H_n^{(1)}(k_S r) \end{aligned} \tag{3.50}$$

3.3.2 Evaluation

The analytical solutions are best evaluated with numerical computer software. The two parameters of greatest interest, radial particle velocity and tangential stress, are here calculated numerically from the above equations and evaluated for different frequencies. Obtaining results for a large range of frequencies is difficult due to the infinite series in the analytical expressions, which has to be approximated.

3.3.2.1 Radial particle velocity

Since the constant input parameter of the incoming wave is the particle velocity, it is of great importance to investigate the output velocity at the tunnel surface. The velocity amplification for any frequency is equivalent to the displacement and acceleration amplifications, as discussed in Section 2.4. As shown in Figure 3.4, the maximum radial velocity is obtained at the point closest to the incident wave (i.e. at $\theta = \pi$). The real part, the imaginary part and the absolute value of the velocity amplification at $\theta = \pi$, as a function of wave number, is shown in Figure 3.5 for $r = a = 5$ m and a close-up of the absolute value is shown in Figure 3.6. As expected, the amplification is equal to one for low frequencies and is close to two for higher frequencies (see the discussions in Sections 2.3 and 3.2). The amplification at resonance is approximately 2.1, which is less than for the SH-wave. The double amplitude is reached at $k_P \approx 0.12$ (which represents $f \approx 100$ Hz).

Haug et al. (1978) found the wavelength at the first resonance frequency of a cylindrical cavity to equal the circumference of the cavity. This implies that the compressive wave number multiplied by the radius of the cavity should equal one at resonance. As seen in Figure 3.7, where velocity amplification is plotted versus wave number multiplied by tunnel radius (the figure is valid for all radii), the first peak is indeed very close to one, giving strength to the above statement. So the first resonance peak occurs at

$$k_{Pr} = \frac{1}{a}, \tag{3.51}$$

which implies that the wavelength at resonance is

$$\lambda_r = 2\pi a, \tag{3.52}$$

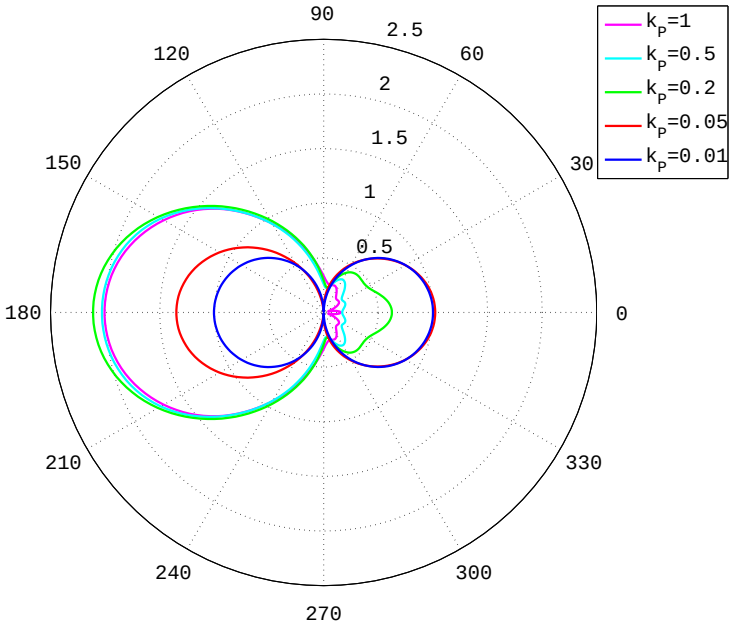

Figure 3.4: Radial velocity amplification at $r = a = 5$ m.

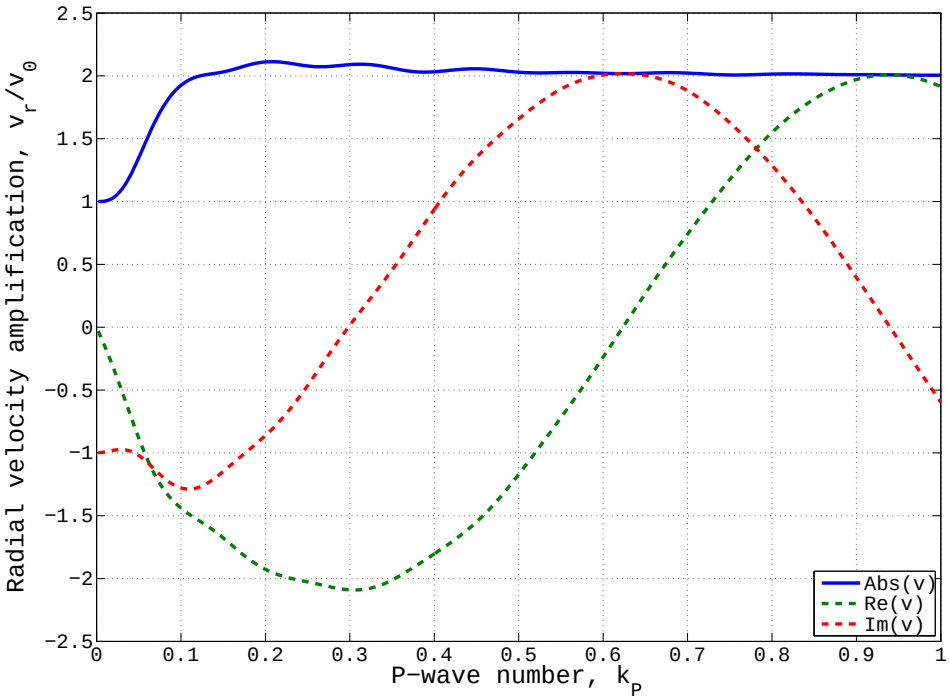

Figure 3.5: Radial velocity amplification at $\theta = \pi$ and $r = a = 5$ m.

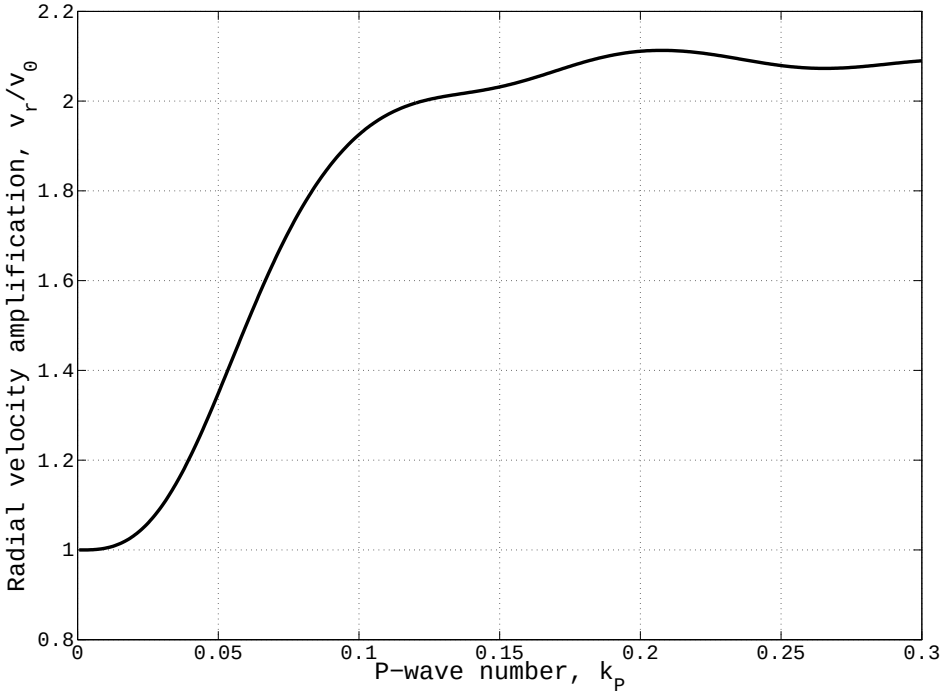

Figure 3.6: Radial velocity amplification at $\theta = \pi$ and $r = a = 5$ m.

the circular frequency is

$$\omega_r = \frac{c_P}{a} \tag{3.53}$$

and the frequency is

$$f_r = \frac{c_P}{2\pi a}. \tag{3.54}$$

It can also be seen in Figure 3.7 that the double amplitude is reached at $k_P a = 0.6$, i.e. that

$$\frac{v_r}{v_0} \geq 2 \qquad \text{when} \qquad f \geq 0.6\frac{c_P}{2\pi a}. \tag{3.55}$$

It is of interest to examine the radial amplitude amplification further away from the tunnel because it can help in determining the stability of the tunnel wall. The velocity amplification, starting from the wall of the cavity and moving further away in the radial direction, is shown in Figure 3.8 for three different cavities. Since these calculations concern steady state, there is an interference between the incoming and scattered waves, which give rise to the oscillating pattern. One interesting observation is that the distance between the peaks seems to be independent of the tunnel radius while the rate of amplification decrease is dependent of radius. As Figure 3.9 shows, the amplification for a given frequency is approximately dependent only on the distance from the cavity wall, normalized by radius (i.e. $\frac{r-a}{a}$). In this case ($k_P = 5$) the amplification decreases to approximately 30 percent 4 tunnel radii away from the circumference. For lower frequencies, the decrease is slightly faster. Note that Figures 3.4 to 3.9 and Equation (3.55) are equally valid for particle displacement and acceleration as for velocity.

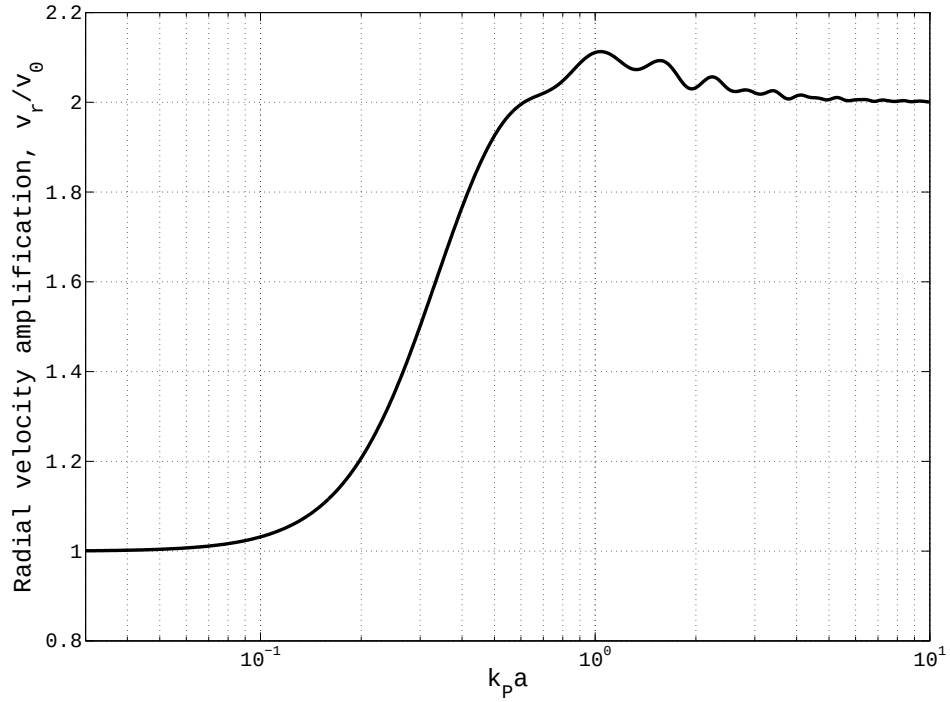

Figure 3.7: Radial velocity amplification at $\theta = \pi$ and $r = a$ versus wave number multiplied by radius, showing resonance at $k_P a \approx 1$.

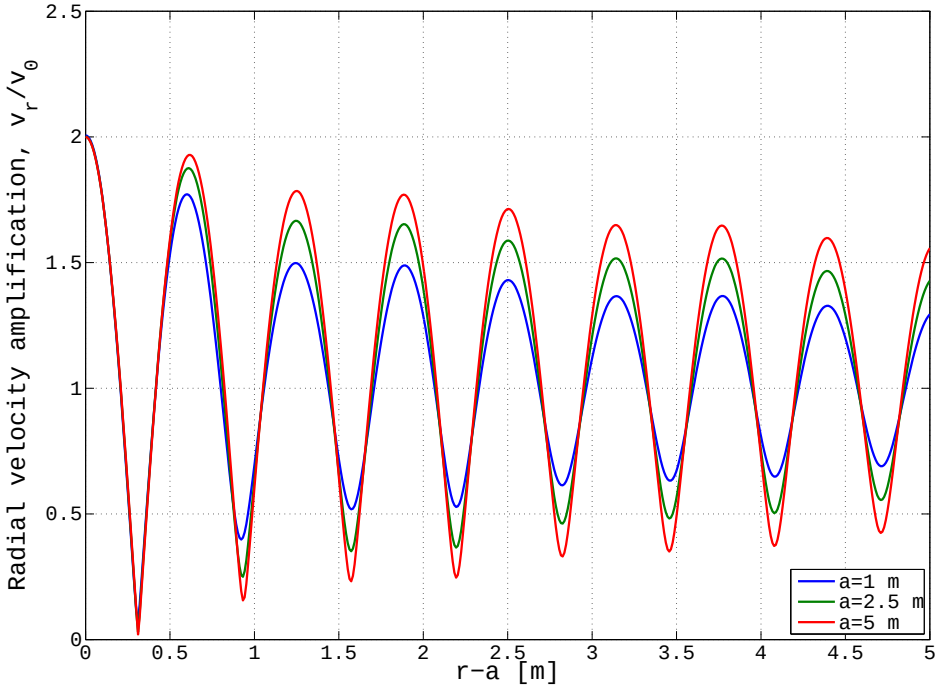

Figure 3.8: Radial velocity amplification at $\theta = \pi$ as the observation point moves away from the tunnel ($k_P = 5$).

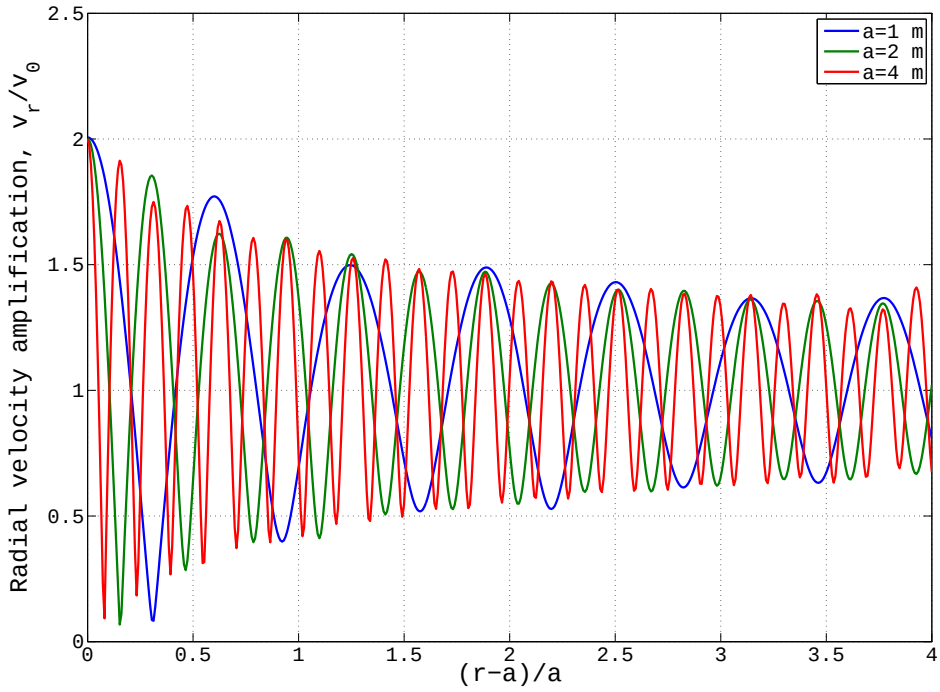

Figure 3.9: Radial velocity amplification as a function of normalized radial distance from cavity surface ($k_P = 5$).

3.3.2.2 Tangential stress

The tangential stress at the tunnel circumference for a radius of 5 m and an initial velocity amplitude of 0.1 m/s is shown in Figure 3.10. The maximum stress is obtained at points close to $\theta = \pi/2$ (and $\theta = 3\pi/2$ due to symmetry). The stress at that angle as a function of wave number is shown in Figure 3.11 for $r = a = 5$ m and a comparison for different radii is shown in Figure 3.12. The maximum value is 4 MPa and occurs at $k_P a = 0.25$, i.e. the frequency for maximum stress is not the same as the one for maximum velocity amplification. The wave number, wavelength, circular frequency and frequency for peak stress are obtained by

$$k_{Pr} = \frac{1}{4a}, \tag{3.56}$$

$$\lambda_r = 8\pi a, \tag{3.57}$$

$$\omega_r = \frac{c_P}{4a}, \tag{3.58}$$

$$f_r = \frac{c_P}{8\pi a}. \tag{3.59}$$

Since $\sigma_{\theta\theta}$ is proportional to φ_0 in Equation (3.49) and φ_0 is proportional to v_0 (which in this case is 0.1 m/s), the stress is proportional to the particle velocity of the incoming wave. This means that without changing the elastic properties ($\lambda = 24$ GPa, $\mu = 24$ GPa), since $\sigma_{\theta\theta} = 4$ MPa for $v_0 = 0.1$ m/s, then for example $\sigma_{\theta\theta} = 8$ MPa for $v_0 = 0.2$

m/s. Generally, using Equations (2.6), (2.11) and (3.49),

$$\begin{aligned}\sigma_{\theta\theta}(\varphi_0, a, r, \theta, k_P, k_S, \lambda, \mu) &= \varphi_0 \sigma_{\theta\theta}(a, r, \theta, k_P, k_S, \lambda, \mu) \\ &= \frac{v_0}{-i\omega k_P} \sigma_{\theta\theta}(a, r, \theta, k_P, k_S, \lambda, \mu)\end{aligned} \tag{3.60}$$

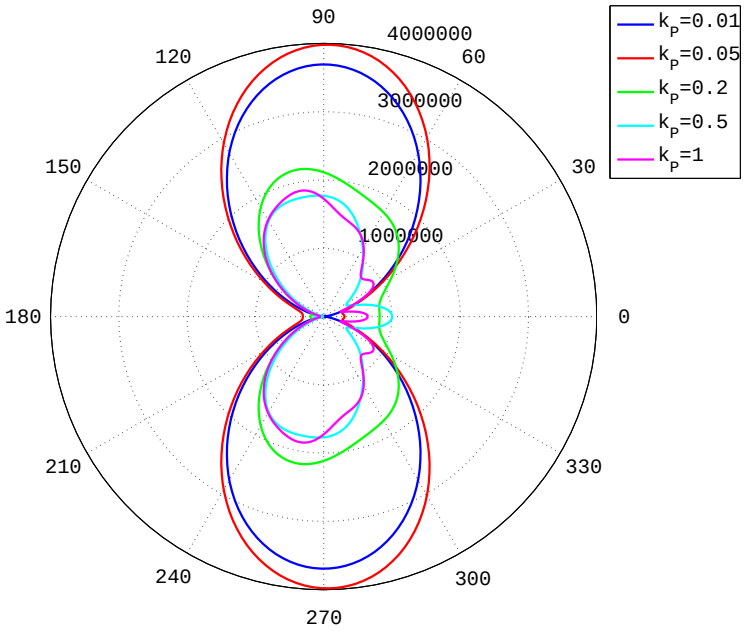

Figure 3.10: Tangential stress amplitude (Pa) for $r = a = 5$ m.

Table 3.1 is the result of calculating the maximum dynamic tangential stress around the cavity for different densities and elastic moduli. The P-wave velocity is obtained by

$$c_P = \sqrt{\frac{M}{\rho}} = \sqrt{\frac{\lambda + 2\mu}{\rho}} \tag{3.61}$$

and σ_0 is the stress induced by the same wave in a continuous infinite material, obtained by Equation (2.19). The dynamic stress concentration factor[4] seems to be dependent only on κ which is the ratio of the S- and P-wave numbers and can be calculated from Poisson's ratio,

$$\kappa = \frac{k_S}{k_P} = \sqrt{\frac{2 - 2\nu}{1 - 2\nu}}. \tag{3.62}$$

For rock mass (and many other materials) Poisson's ratio is usually between 0.25 and 0.3 which yields a value of κ between $\sqrt{3}$ and $\sqrt{3.5}$. Since the waveform is sinusoidal, which implies higher loads than realistic blast loads (for the same peak particle velocity) and

[4]The dynamic stress concentration factor is the ratio of $\sigma_{\theta\theta}$ over σ_0.

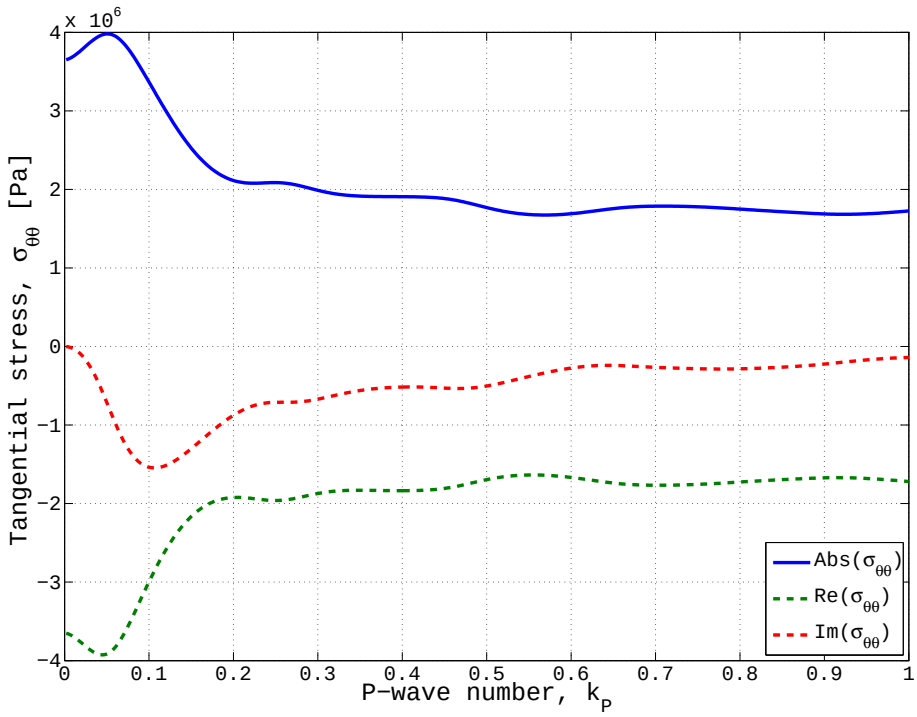

Figure 3.11: Tangential stress amplitude at for $r = a = 5$ m.

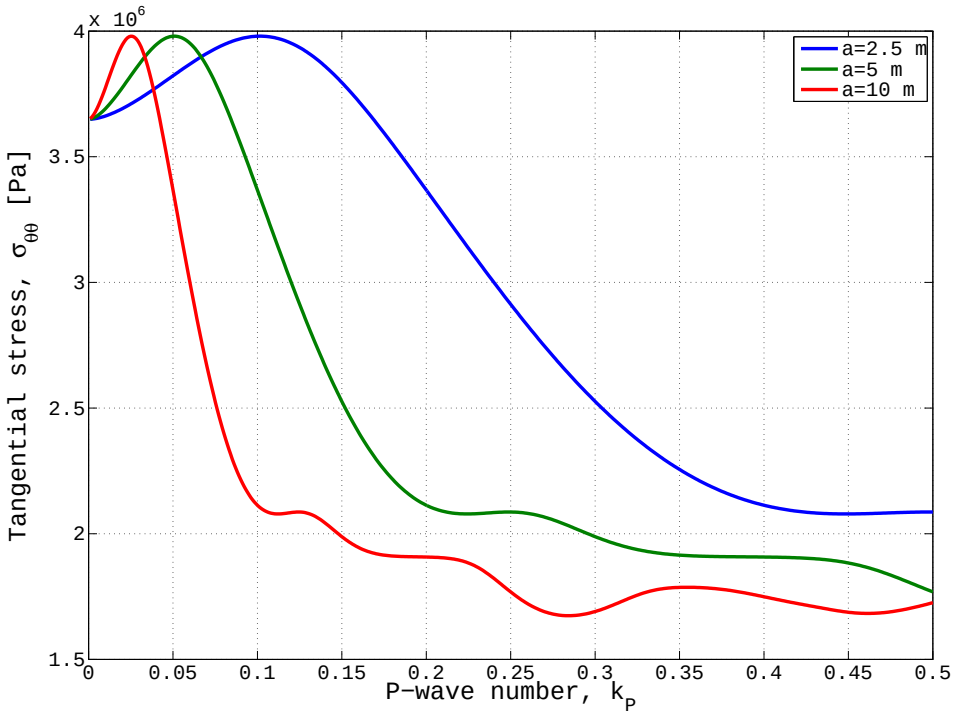

Figure 3.12: Tangential stress amplitude (absolute value).

since the dynamic stress concentration factor in Table 3.1 is right below 3 for common values of Poisson's ratio, the following upper bound expression can be constructed using Equation (2.19),

$$\sigma_{\theta\theta}^{max} < 3Zv_0, \tag{3.63}$$

where Z is the specific impedance of the material and v_0 is the peak particle velocity of the incident wave[5]. Equation (3.63) is in good correlation with Kirsch's static solution which states that the maximum tangential stress around a circular cavity, induced by a static compressive stress in one direction and a zero stress in the perpendicular direction, is three times the applied stress.

ρ	λ	μ	c_P	κ	$\sigma_{\theta\theta}/\sigma_0$
1500 kg/m^3	10 GPa	20 GPa	5573 m/s	$\sqrt{2.5}$	3.06
1500 kg/m^3	20 GPa	10 GPa	5164 m/s	$\sqrt{4}$	2.77
1500 kg/m^3	20 GPa	20 GPa	6324 m/s	$\sqrt{3}$	2.91
2000 kg/m^3	10 GPa	20 GPa	5000 m/s	$\sqrt{2.5}$	3.06
2000 kg/m^3	20 GPa	10 GPa	4472 m/s	$\sqrt{4}$	2.77
2000 kg/m^3	20 GPa	20 GPa	5477 m/s	$\sqrt{3}$	2.91
2500 kg/m^3	10 GPa	20 GPa	4472 m/s	$\sqrt{2.5}$	3.06
2500 kg/m^3	20 GPa	10 GPa	4000 m/s	$\sqrt{4}$	2.77
2500 kg/m^3	20 GPa	20 GPa	4899 m/s	$\sqrt{3}$	2.91

Table 3.1: The dynamic stress concentration factor for different densities and elastic moduli.

The maximum tangential stress at $\theta = \pi/2$ for a velocity amplitude of 0.1 m/s for the incoming wave as a function of radial distance from tunnel circumference is shown in Figure 3.13. The dashed line indicates the theoretical value without influence of the cavity, evaluated according to Equation (2.19). The increase in tangential stress around the cavity is noticed approximately three cavity radii away from the surface. After two radii the value is less than 10 percent greater than that of an infinite material with no cavity.

3.4 Summary

Scattering of SH- and P-waves on a cylindrical cavity was analyzed mathematically and evaluated by numerical methods. For the SH-problem, it was found that the displacement, velocity and acceleration amplitude amplification (i.e. the ratio of the amplitude of the total wave over the amplitude of the incoming wave) at the tunnel surface is one for low

[5] Observe that v_0 is the non-amplified peak particle velocity, i.e. not the measured velocity at the tunnel circumference.

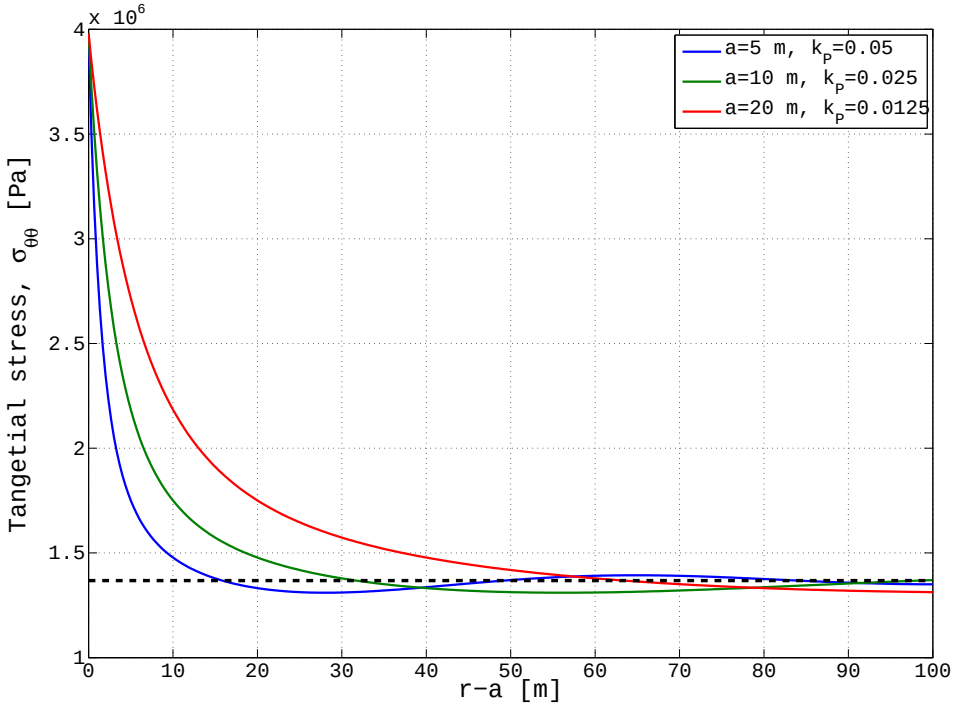

Figure 3.13: Tangential stress amplitude (absolute value) versus distance from tunnel circumference.

frequencies and two for high frequencies. The maximum amplification, approximately 2.2, is obtained at the first resonance frequency, which occurs when the wavelength of the incident wave is equal to the diameter of the cavity. Multiples of the first resonance frequency are also resonance frequencies and they are given by

$$f_r = \frac{c_S}{2a} n, \qquad n = 1, 2, 3, ... \tag{3.64}$$

For the P-wave problem, it was concluded that the existing mathematical expressions are not valid and they were therefore reformulated. Evaluation showed that, as for the SH-wave, the amplitude amplification is one for low frequencies and two for high frequencies. The amplitude is at least doubled for wave numbers larger than $0.6/a$. There is a resonance peak but the amplification is not very large, only about 2.1. The peak occurs when the wavelength of the incoming wave is equal to the circumference of the cavity. The resonance frequency can be expressed as

$$f_r = \frac{c_P}{2\pi a}. \tag{3.65}$$

At a distance of a few cavity radii away from the wall, a considerable part of the amplification is still noticed. However, this idealized case does not consider material damping so it is assumed that the decrease in amplification would be faster for geomaterials.

The tangential stress increase around the tunnel during diffraction of P-waves is largest close to the roof and to the floor (when the vibrations approach from the side). The

maximum stress occurs at the frequency

$$f_r = \frac{c_P}{8\pi a} \tag{3.66}$$

and can be described in upper bound using the specific impedance of the material,

$$\sigma_{\theta\theta} < 3Zv_0. \tag{3.67}$$

The stress field is affected by the cavity at a radial distance of about three radii from the circumference.

4 NUMERICAL FDM MODEL

To verify the results from the previous chapter, numerical simulations have been carried out and the results have been compared to those based on the analytical solutions. To get as realistic results as possible, the analyses are performed in three dimensions so that the response of the tunnel is simulated properly. 3D analysis is generally more suitable for simulating dynamic properties and wave propagation. Lu et al. (2005) compared 2D and 3D simulations for a buried structure in soil subjected to vibrations from blasting. They concluded that a 2D model could simulate wave propagation in the soil satisfactory but to obtain realistic results for the response of the structure, a 3D model is necessary.

The simulations have been carried out in the 3-dimensional distinct element (DEM) software 3DEC 3.0 (3-dimensional Distinct Element Code) with dynamic option, developed by Itasca Consulting Group, Inc. (2005b). 3DEC simulates discontinuous media by allowing the user to divide the model into discrete blocks. Within each block, the behavior is modeled with the finite difference method (FDM), which is closely related to the finite element method (FEM) and produce results with about the same accuracy as FEM (Cook et al., 1989)[1]. 3DEC is especially suited for jointed rock mass. The general solution procedure for dynamic analysis is shown in Figure 4.1.

Modeling the behavior of the circular tunnel is divided into three steps:

1. Create the model.
2. Verify the model by simulating events with known results.
3. Perform simulations in accordance to the previous chapter and compare the results.

4.1 Model description

The model consists of a circular cylindrical tunnel in a block with no joints, as shown in Figure 4.2. Because of the absence of discontinuities, it is purely an FDM model. Only reflection of P-waves is simulated since it is the case most relevant for blasting applications. Because there are no SH-waves, a plane strain condition can be applied in the z-direction and the block can therefore be very thin. The model measures 100x100x0.5 m and as in the previous chapter, the radius of the tunnel is 5 m and there is no material damping so that the numerical and analytical results are comparable.

[1] In this report, the term FEM is considered to include FDM, DEM and other related methods.

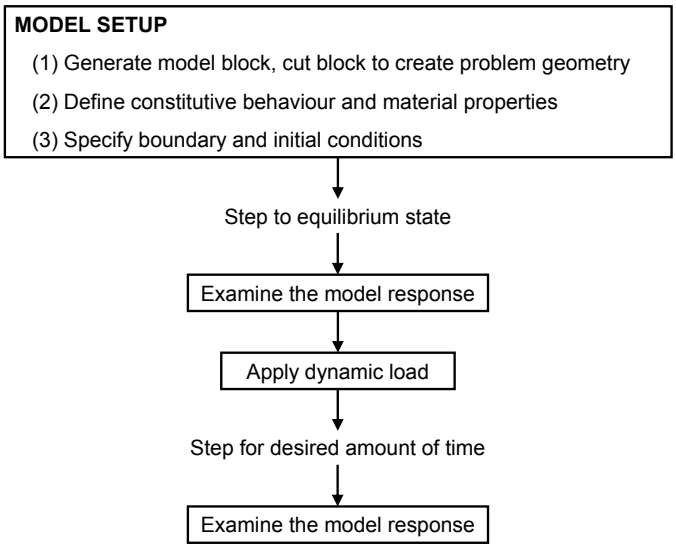

Figure 4.1: Solution procedure for dynamic analysis in 3DEC. Modified after Itasca Consulting Group, Inc. (2005b).

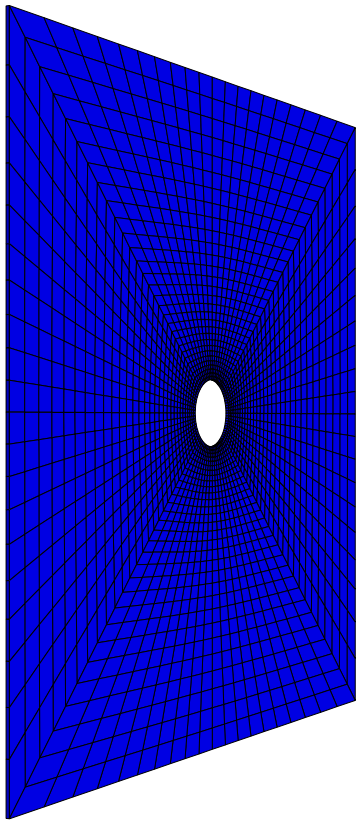

Figure 4.2: The FDM model.

Generating a proper grid is perhaps the most crucial part in finite element analysis. The shape and size of the zones affect the result. A finer mesh is generally more accurate but implies longer computation time. Usually, a shorter distance between the gridpoints is used closer to the area of most interest but in dynamic analysis, wave propagation require a fine mesh throughout the model. Studies have shown that at least eight gridpoints per wavelength are necessary for satisfactory representation of the dynamic wave (Itasca Consulting Group, Inc., 2005a). In this model, the grid consists of six-sided polyhedra zones, which are known to have high accuracy. Since a wide range of frequencies are simulated, four different meshes are generated (Figure 4.3), where the finer ones are used for higher frequencies.

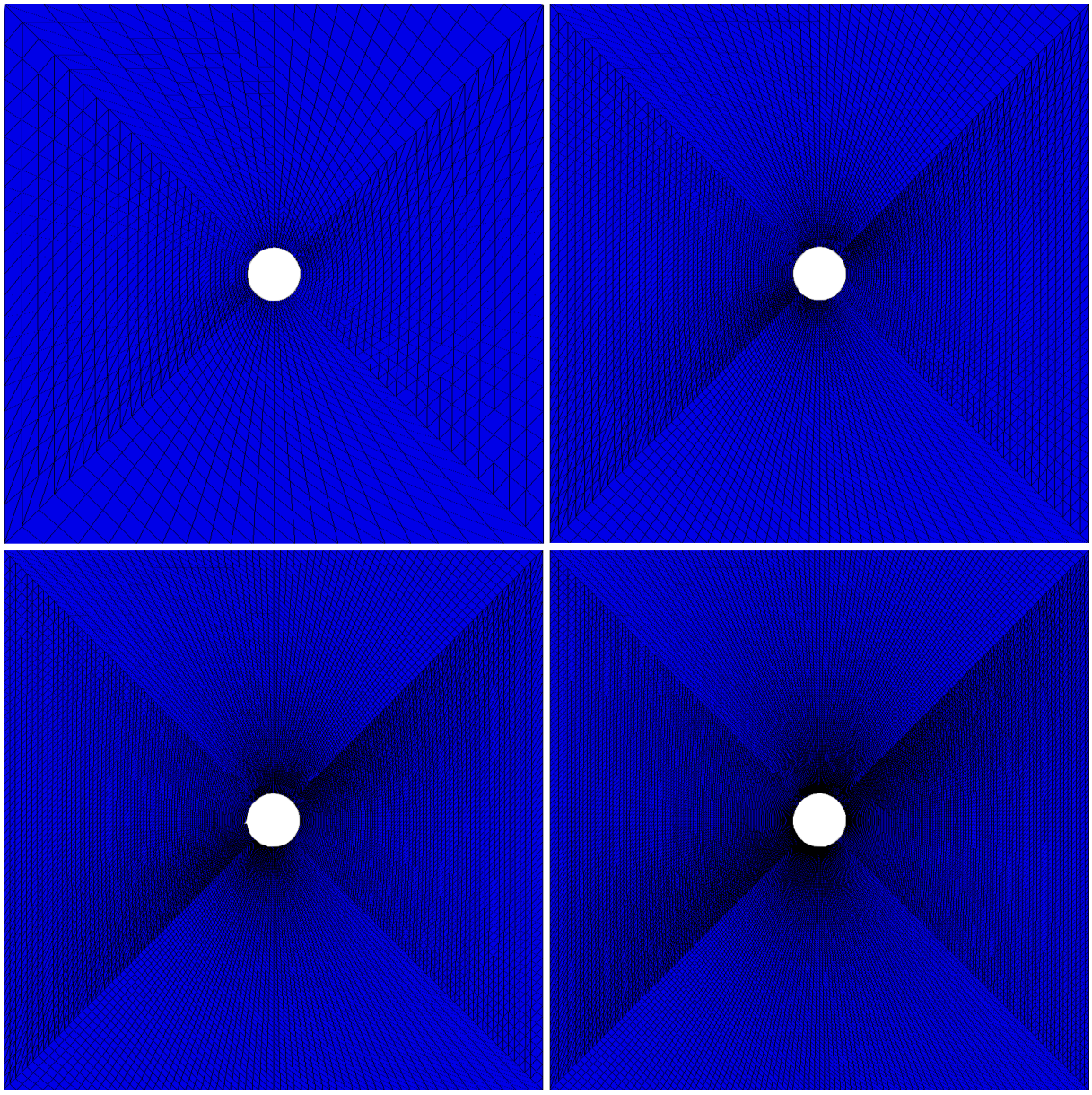

Figure 4.3: The four different zonings for the FDM model.

Because of the small strains involved in blast-induced vibrations (no plastic strains), a linear elastic material model is used. The elastic properties defined in Section 3.1 were assigned to the material. The dynamic input is applied at the left x-boundary as a sinusoidal velocity in the x-direction with an amplitude of 0.1 m/s. The two z-boundaries are fixed with a zero z-velocity so that the plain strain condition is satisfied. Regarding the right x-boundary and the y-boundaries, they cannot be fixed since that would imply that the wave is reflected back into the model. To simulate an infinite material, non-reflecting boundaries are used. 3DEC uses the viscous boundaries developed by Lysmer and Kuhlmeyer (1969), which consists of dashpots absorbing the wave.

4.2 Verification

After creating the FDM model, it has to be verified by simulating known cases where the outcome can be compared with the expected results. Two events are simulated, static stress around a circular cavity and dynamic stress induced by a plane P-wave.

4.2.1 Static stress

For a circular excavation in an elastic material, the tangential stress at the circumference is given in Hudson and Harrison (1997) by

$$\sigma_{\theta\theta} = p_z((1 + k_0) + 2(1 - k_0)\cos(2\theta)), \tag{4.1}$$

where p_z is the vertical in-situ stress and k_0 is the pressure coefficient, which is the ratio of horizontal over vertical stress. For hydrostatic stress conditions, i.e. when $k_0 = 1$, the tangential stress becomes

$$\sigma_{\theta\theta} = 2p_z. \tag{4.2}$$

A static in-situ compressive stress of 1 MPa was applied in the x and y direction at all nodes and at the x and y boundaries. The tangential stresses at the tunnel surface were then monitored while iterating to equilibrium, shown in Figure 4.4. The stresses in the 3DEC model were in good agreement with the theoretical values, i.e. Equation (4.2) is valid for the model.

4.2.2 Dynamic stress

For the FDM model to be valid, the stresses before any disturbance of the plane wave has taken place should equal those calculated by Equation (2.19). To minimize the influence of reflection and diffraction, the tunnel radius was decreased to 0.5 m while keeping the remaining geometry unchanged. The compressive stress in the x-direction, which should equal 1,37 MPa according to Equation (2.19), was then monitored at six point throughout the model. The results are shown in Figure 4.5 for different frequencies, where the dashed line indicates the theoretical value. There is very good match between

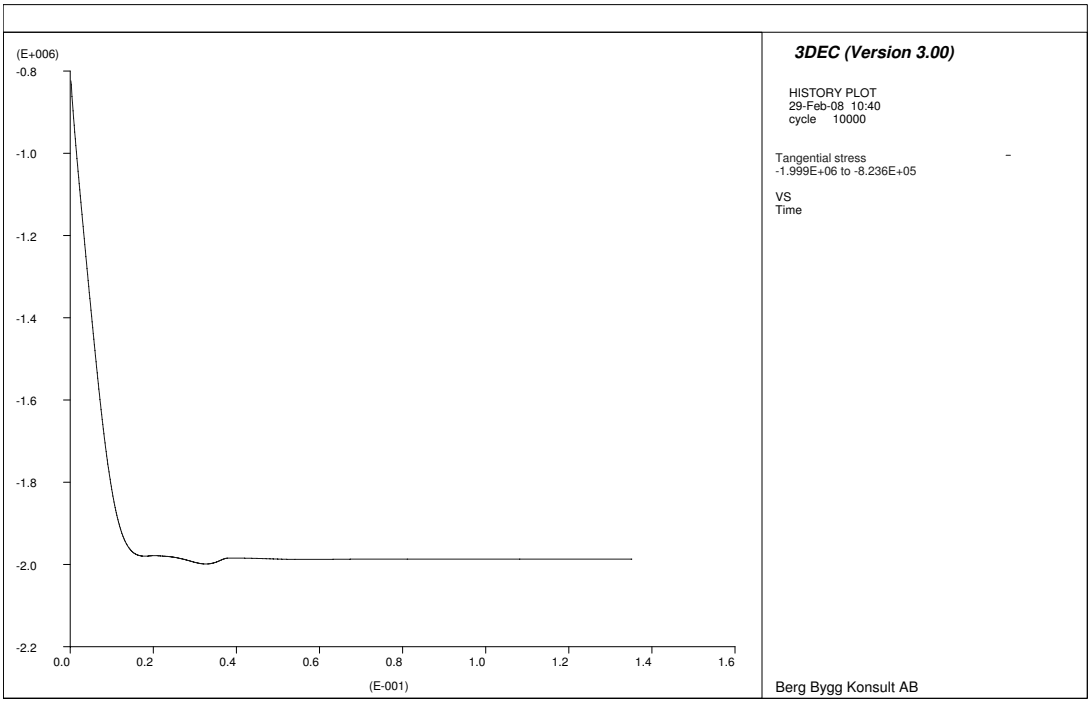

Figure 4.4: Tangential stress (Pa) while iterating to equilibrium.

the stresses obtained in 3DEC and the expected values. After a few cycles, diffraction disturbs the plane wave so that the stresses differ from their initial amplitudes.

4.3 Results

After validating the model, simulations were carried out and compared with the results based on the analytical solutions. Incident P-waves with a velocity amplitude of 0.1 m/s and frequencies varying between 35 Hz and 650 Hz were generated. The model was then iterated until reaching steady state. Two parameters were monitored, radial displacement at the tunnel wall closest to the incident wave and the tangential stress at the tunnel roof.

4.3.1 Displacement

Examples of radial displacement histories at the tunnel wall closest to the incident wave are shown in Figures 4.6 and 4.7 for the frequencies 120 Hz and 300 Hz respectively. See Appendix A.2 for a presentation of all displacement histories. It can be seen that there is often a peak in one of the first cycles before steady state occurs. The number of cycles required to reach steady state is dependent of frequency. For higher frequencies, more cycles are required than for lower frequencies.

The steady state values of radial particle displacement amplitude are plotted in Figure 4.8 together with the analytical solution. There is a good match between the FDM simulations

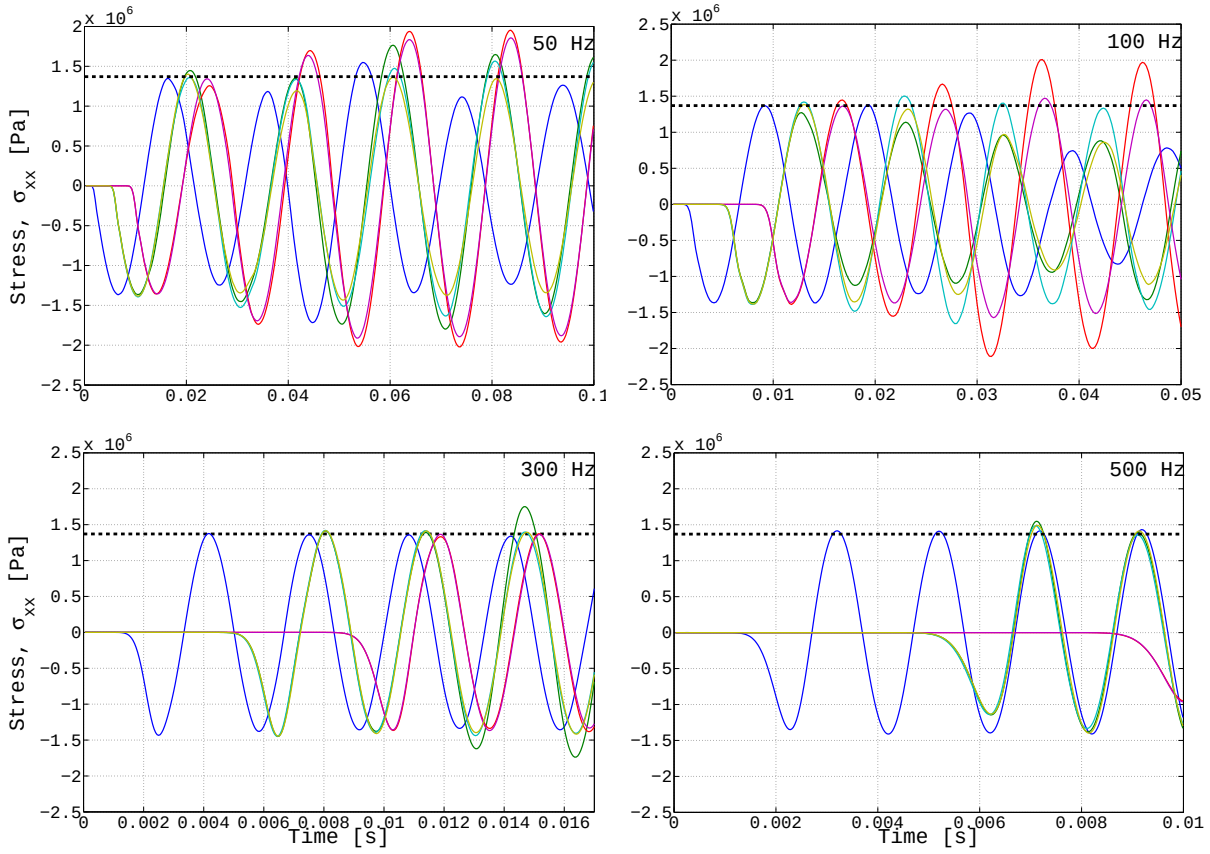

Figure 4.5: Stress histories at six points in the model for different frequencies showing good agreement with the theoretical value (dashed line) and thus validating the model.

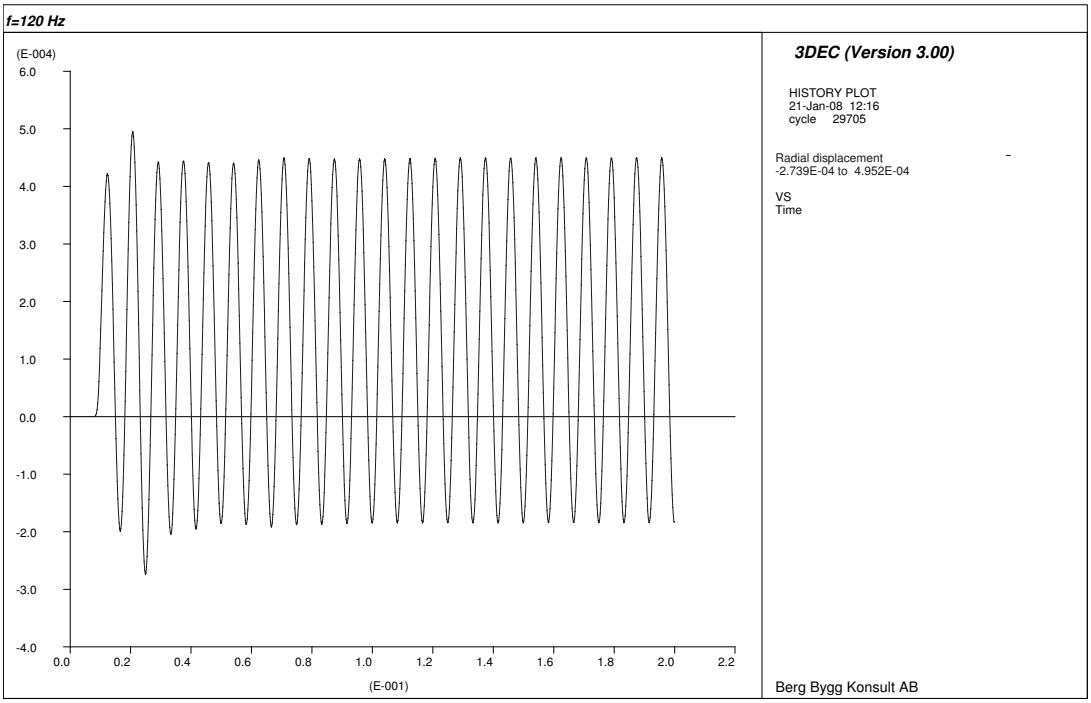

Figure 4.6: Radial displacement history (m) at $r = a = 5$ m and $\theta = \pi$ for $f = 120$ Hz.

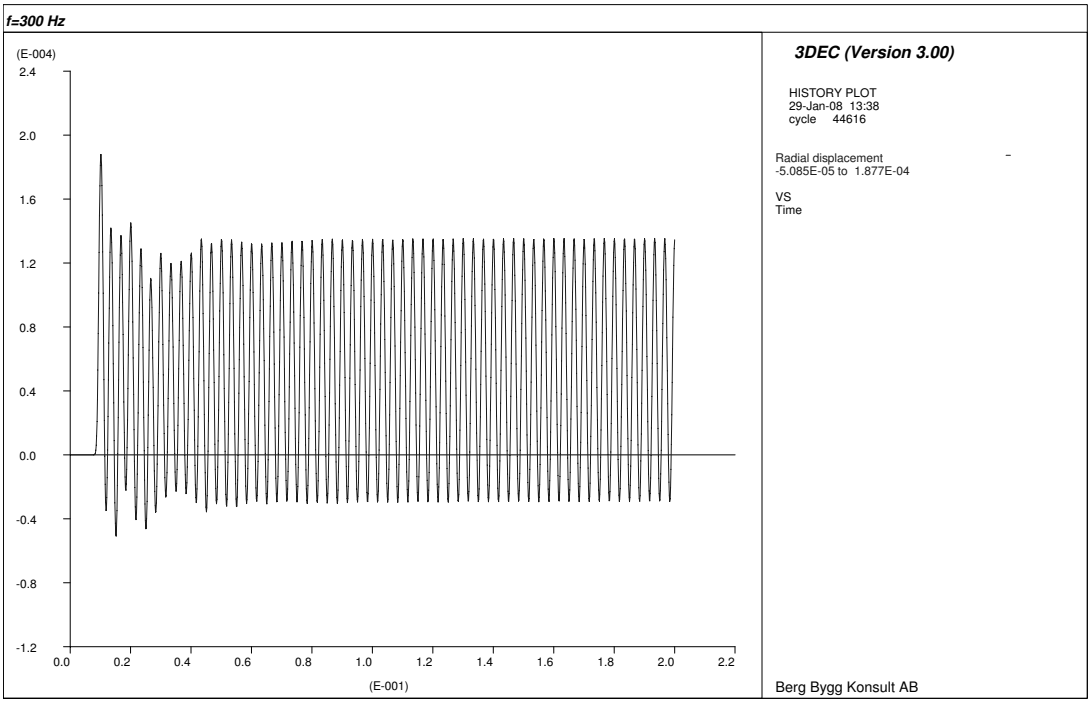

Figure 4.7: Radial displacement history (m) at $r = a = 5$ m and $\theta = \pi$ for $f = 300$ Hz.

and the theoretical values, even though the numerical result are slightly higher. Since the particle velocity is constant, the displacement tends toward infinity as the frequency approaches zero.

4.3.2 Stress

A vector plot of the principal stresses around the tunnel at steady state is shown in Figure 4.9 for $f = 450$ Hz. The stresses show good correlation with the stress contours based on the analytical solutions in Figure 3.10. The tangential stress histories at the tunnel roof are shown in Figures 4.10 and 4.11 for 120 Hz and 300 Hz and in Appendix A.3 for all frequencies. It can be observed that the tangential stress is generally compressive and only a small tensile stress occurs at high frequencies. As with displacement, there is a stress peak before reaching steady state and the number of cycles required to reach steady state varies with frequency.

A comparison between the numerical simulations in 3DEC and the analytical results is shown in Figure 4.12. The match is not as good as for displacement but the overall trend seems to be represented. Also, the maximum value is the same and occurs at the same wave number (4 MPa at $k_P \approx 0.05$). The reason for the larger variations is probably that stresses are much more sensitive and less accurate in FEM analysis than displacements are (Cook et al., 1989).

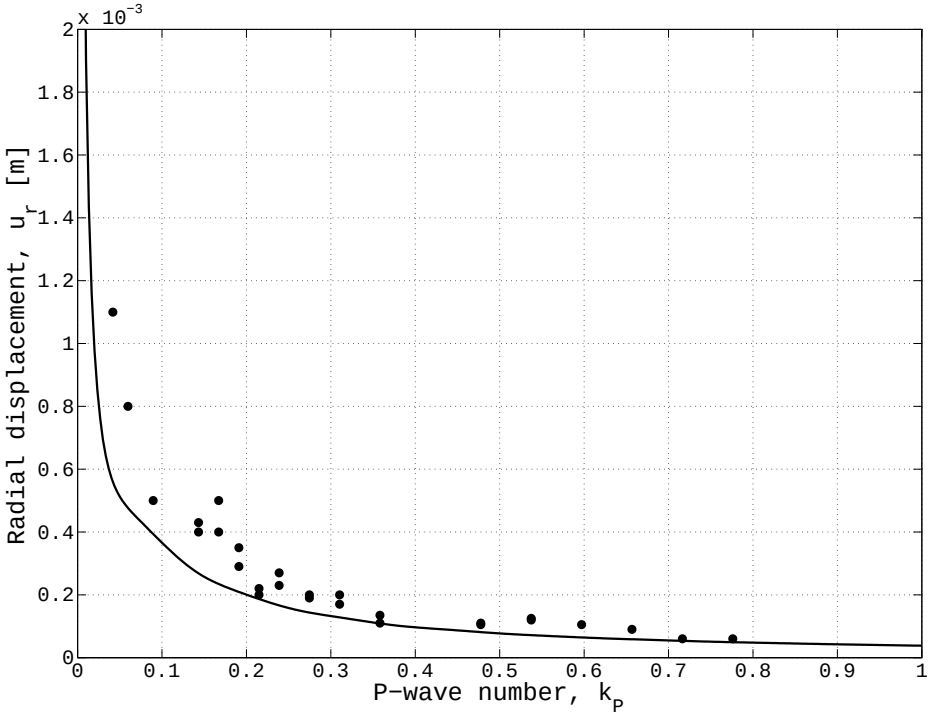

Figure 4.8: A comparison between the FDM results (dots) and the analytical results (curve) for radial particle displacement ($r = a = 5$ m, $\theta = \pi$).

4.4 Summary

A finite element model of a cylindrical cavity was created in 3DEC to confirm the results of the analytical solutions in Section 3.3. The model was validated by comparing the static stress around the circular cavity and the dynamic stress in the material with their theoretical values. The simulated radial displacements at the tunnel wall closest to the incident wave showed a good match with the analytical results. For the tangential stress at the roof, the correlation was not as good as for displacement (probably due to the sensitiveness of stress in FEM) but the FEM results seemed to follow the same pattern as the analytical results.

Stress and displacement behave similarly before steady state is reached. Both usually have a peak in the first few cycles. Steady state is reached within only a couple of cycles for low frequencies and in a larger number of cycles for higher frequencies. The radial displacement oscillates around the equilibrium state, but is greater in the direction toward the center of the cavity. The tangential stress is almost exclusively compressive.

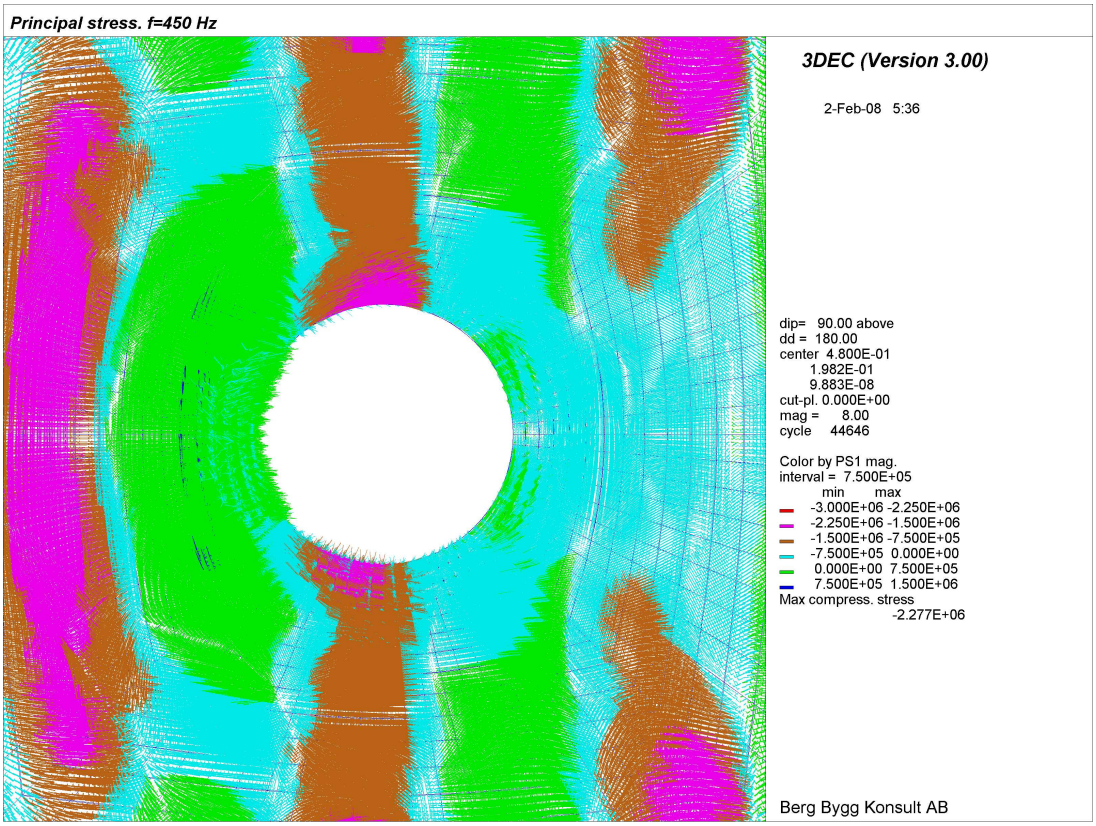

Figure 4.9: Principal stress vectors around the tunnel during steady state. The compressive wave is propagating from left to right.

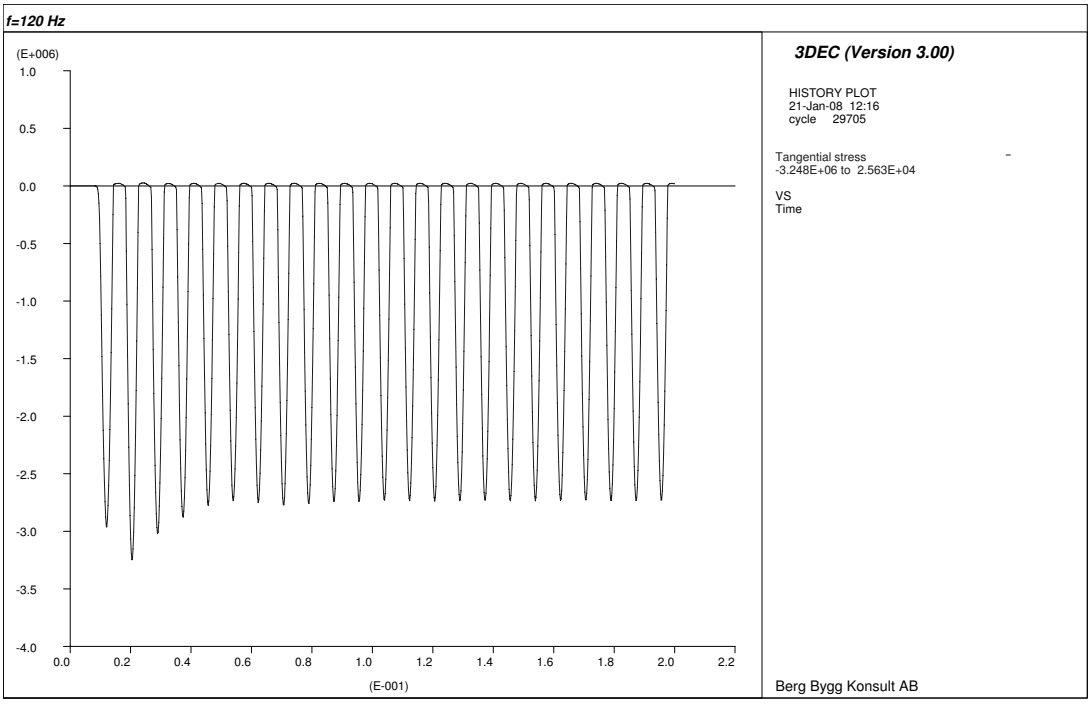

Figure 4.10: Tangential stress history at $r = a = 5$ m and $\theta = \pi/2$ for $f = 120$ Hz.

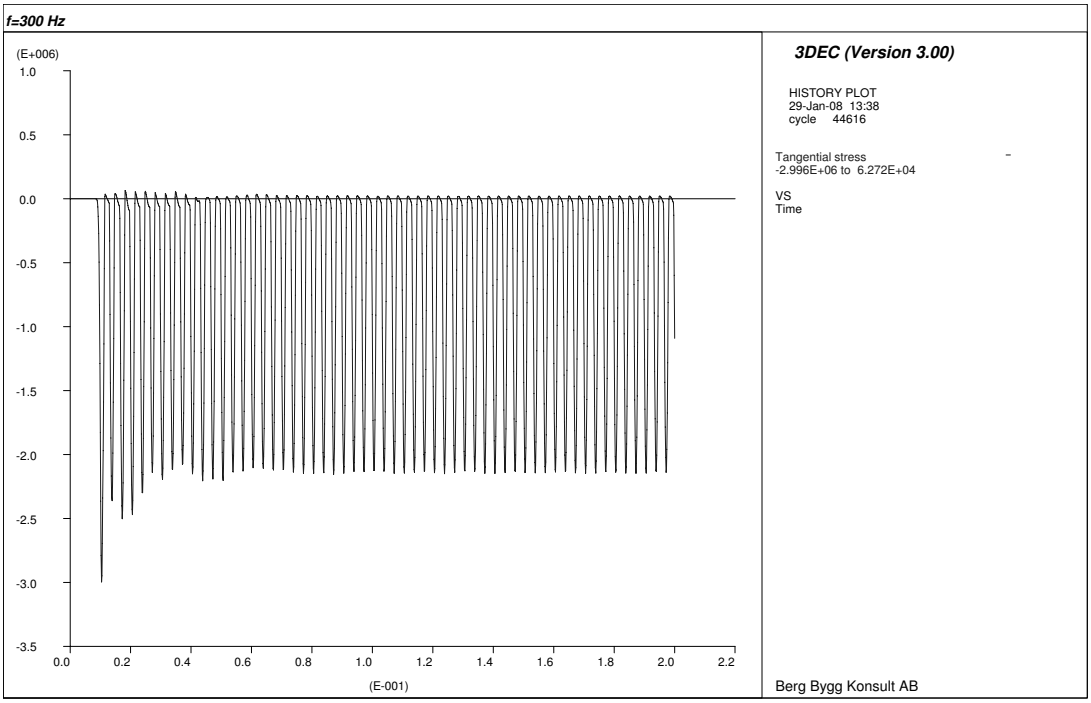

Figure 4.11: Tangential stress history at $r = a = 5$ m and $\theta = \pi/2$ for $f = 300$ Hz.

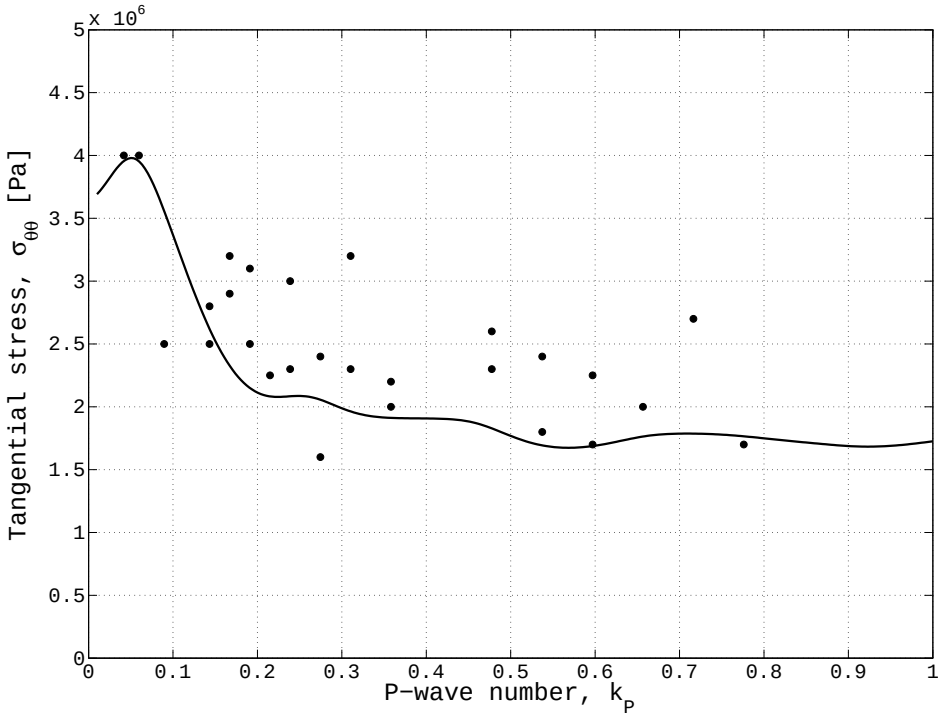

Figure 4.12: A comparison between the FDM results (dots) and the analytical results (curve) for tangential stress ($r = a = 5$ m, $\theta = \pi/2$).

5 CONCLUSIONS

The steady state dynamic response of a cylindrical excavation in an elastic material was investigated by both analytical and numerical methods. The vibrational input was sinusoidal with frequencies and particle velocities resembling those induced by blasting. It was found that there is an amplification in radial particle velocity amplitude at the circumference of the tunnel compared to the incident vibrations, varying from one for low frequencies to two for high frequencies. Between these two states there is a resonance frequency which yields the maximum amplification. The amplification of amplitude is also applicable to particle displacement and acceleration.

For an incident SH-wave, resonance occurs when the wavelength is equal to the diameter of the tunnel and, for an incident P-wave, when the wavelength is equal to the circumference. These frequencies can be expressed as

$$f_r^{(SH)} = \frac{c_S}{2a}, \tag{5.1}$$

$$f_r^{(P)} = \frac{c_P}{2\pi a}. \tag{5.2}$$

As an example, assuming diameters of 8 to 16 m, a P-wave velocity of 5000 m/s and an S-wave velocity of 3000 m/s, which are realistic values for rock mass, resonance frequencies of approximately 100 to 400 Hz are obtained. Since the dominating frequency in blast-induced vibrations usually lie within the interval 200 to 500 Hz, it is obvious that there is a possible risk of resonance in tunnels close to blasting activity. The amplification at resonance is, however, relatively modest. Moving further away from the tunnel, for a given frequency, the amplification is approximately dependent only on the distance from the cavity wall, normalized by the tunnel radius.

The tangential stress field around the tunnel changes when exposed to vibrations. The maximum additional compressive stress can be described in upper bound by

$$\sigma_{\theta\theta} < 3Zv_0 \tag{5.3}$$

for common blast signals and intact rock and occurs close to the frequency $c_P/8\pi a$. The tensile stress is very small. At a radial distance of two tunnel radii from the circumference, the amplification is less than 10 percent greater than that of an infinite material with no cavity and at distances greater than three tunnel radii, there is no amplification. An example of the diffraction of a propagating stress wave around the tunnel, simulated in 3DEC, is shown in Figure 5.1.

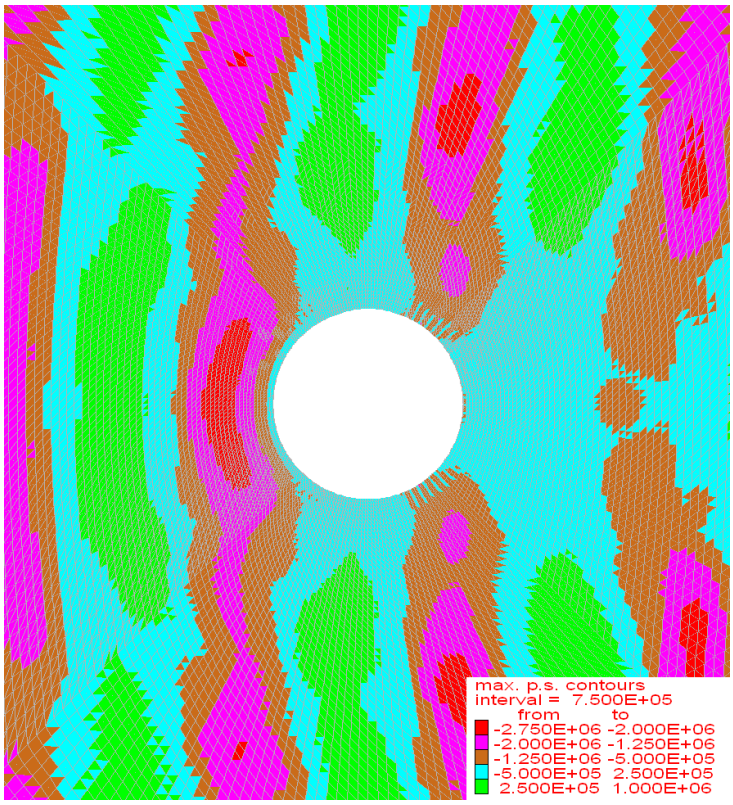

Figure 5.1: Maximum principal stress (Pa) of a 450 Hz P-wave propagating from left to right.

Finite element analysis showed that for stress and displacement (the two parameters investigated), there is a peak value during one of the first cycles, which is greater than the steady state value. It was also found that a higher frequency requires a larger number of cycles to reach steady state.

Finally, it should be noted that the analytical solution for tangential stress around a cylindrical cavity, induced by a plane P-wave, in Mow and Pao (1971) is incorrect.

5.1 Practical implications

The lessons learned from this study should be the frequency dependence of measured vibrational data at the tunnel circumference. So when analyzing measured data, the frequency should be taken into consideration and compared to the tunnel size. It should also be noted that resonance can occur in a tunnel and that the resonance frequency is the same order as the dominating frequency for blast signals. Finally, there is an additional stress of considerable size induced by the propagating wave, that might cause damage. With reservation that this is an idealized case, these issues should be regarded in planning and analyzing blasting activity.

5.2 Further research

The results obtained herein should be regarded as a basis for further studies in dynamic response of tunnels. Most tunnels are, in fact, not circular and rock mass is generally not homogeneous. Influence of tunnel shape, local geology and reinforcement must be considered to obtain damage criteria for real tunnels. Furthermore, all possible damage mechanisms should be defined. The transient response to real blast vibrational records should be investigated since sinusoidal input overestimates the dynamic load. In conclusion, if dynamic damage mechanisms in tunnels were properly defined and assessed, then together with theories for wave propagation it would serve as a tool for optimization of blasting rounds and thus lower the costs and risks associated with blasting.

BIBLIOGRAPHY

AB Storstockholms Lokaltrafik (2001a). Allmänna anvisningar Fö-I-364. Sprängningsarbeten inom eller i närhet av AB Storstockholms Lokaltrafik spåranläggningar.

AB Storstockholms Lokaltrafik (2001b). Allmänna anvisningar Fö-I-365. Gränsvärden för sprängningsinducerade vibrationer inom eller i närhet av AB Storstockholms Lokaltrafik spåranläggningar.

Bodare, A. (1997). *Jord- och bergdynamik*. Royal Institute of Technology, Dept. of Soil- and Rock Mechanics, Stockholm.

Cook, R. D., Malkus, D. S., and Plesha, M. E. (1989). *Concepts and applications of finite element analysis*. John Wiley and Sons, Inc.

Dowding, C. H. (1985). *Blast vibration monitoring and control*. Prentice Hall, Inc., Englewood Cliffs, NJ.

Graff, K. F. (1975). *Wave motion in elastic solids*. Dover Publications, Inc., New York.

Hao, H., Wu, Y., Ma, G., and Zhou, Y. (2000). Characteristics of surface ground motions induced by blasts in jointed rock mass. *Soil Dynamics and Earthquake Engineering*, 21:85–98.

Haug, A. J., Solomon, S. G., and Überall, H. (1978). Resonance theory of elastic wave scattering from a cylindrical cavity. *Journal of Sound and Vibration*, 57:51–58.

Hudson, J. and Harrison, J. (1997). *Engineering rock mechanics - an introduction to the principles*. Elsevier Ltd, Oxford.

Itasca Consulting Group, Inc. (2005a). 3DEC - Optional Features.

Itasca Consulting Group, Inc. (2005b). 3DEC - Users's Guide.

Kramer, S. L. (1995). *Geotechnical earthquake engineering*. Prentice Hall.

Lu, Y., Wang, Z., and Chong, K. (2005). A comparative study of buried structure in soil subjected to blast load using 2D and 3D numerical simulations. *Soil Dynamics and Earthquake Engineering*, 25:275–288.

Lysmer, J. and Kuhlmeyer, R. (1969). Finite dynamic model for infinite media. *Journal of the Engineering Mechanics Division, ASCE*, 95(EM4):859–877.

Mow, C. C. and Pao, Y. H. (1971). The diffraction of elastic waves and dynamic stress concentrations. Technical Report R-482-PR, United States Air Force Project Rand.

Ouchterlony, F. and Niklasson, B. (2004). Sprängning och sprängteknik. In Stille, H., Eriksson, M., and Nord, G., editors, *Kompendium i bergteknik*, pages 71–124. Royal Institute of Technology, Dept. of Soil- and Rock Mechanics.

Pao, Y. H. and Mow, C. C. (1973). *The diffraction of elastic waves and dynamic stress concentrations*. Crane, Russak and Company Inc., New York.

Råde, L. and Westergren, B. (2004). *Mathematics handbook for science and engineering*. Studentlitteratur, Lund.

Stille, H., Eriksson, M., and Nord, G., editors (2004). *Kompendium i bergmekanik*. Royal Institute of Technology, Dept. of Soil- and Rock Mechanics.

Swedish Standards Institute (1991). Vibration and shock - Guidance levels for blasting-induced vibrations in buildings.

Towhata, I. (2008). *Geotechnical earthquake engineering*. Springer.

Wu, Y. K., Hao, H., Zhou, Y., and Chong, K. (1998). Propagation characteristics of blast-induced shock waves in a jointed rock mass. *Soil Dynamics and Earthquake Engineering*, 17:407–412.

Yang, R. and Scovira, D. (2007). Using blast vibration measurements to estimate rock triaxial strains/stresses and dynamic rock strength for blast damage evaluation. In Eberhardt, E., Stead, D., and Morrison, T., editors, *Rock mechanics: Meeting society's challenges and demands*, pages 1547–1552. Taylor and Francis Group, London, UK.

A APPENDIX

A.1 Conversion formulas

Some important dynamic and elastic formulas are summarized in this section. First, the wave number can be expressed as

$$k = \frac{2\pi}{\lambda} \tag{A.1}$$

or

$$k = \frac{\omega}{c}, \tag{A.2}$$

where λ is wavelength, c is wave propagation velocity and ω is circular frequency, related to frequency f by

$$\omega = 2\pi f. \tag{A.3}$$

Hence, the compressional and shear wave number are obtained by

$$k_P = \frac{\omega}{c_P}, \tag{A.4}$$

$$k_S = \frac{\omega}{c_S}. \tag{A.5}$$

Frequency and wavelength are related by

$$f = \frac{c}{\lambda}. \tag{A.6}$$

The P- and S-wave velocities are related to elastic moduli by

$$c_P = \sqrt{\frac{M}{\rho}}, \tag{A.7}$$

$$c_S = \sqrt{\frac{\mu}{\rho}}, \tag{A.8}$$

where, M is constrained modulus, μ is shear modulus and ρ is mass density. The conversion formulas for elastic properties are shown in Table A.1. Note that λ in Table A.1 is Lamé's constant and not wavelength.

Table A.1: Elastic conversion formulas

	λ, μ	E, μ	K, λ	K, μ	λ, ν	μ, ν	E, ν	K, ν	K, E
$K =$	$\lambda + \frac{2\mu}{3}$	$\frac{E\mu}{3(3\mu - E)}$			$\lambda \frac{1+\nu}{3\nu}$	$\frac{2\mu(1+\nu)}{3(1-2\nu)}$	$\frac{E}{3(1-2\nu)}$		
$E =$	$\mu \frac{3\lambda+2\mu}{\lambda+\mu}$		$9K \frac{K-\lambda}{3K-\lambda}$	$\frac{9K\mu}{3K+\mu}$	$\frac{\lambda(1+\nu)(1-2\nu)}{\nu}$	$2\mu(1+\nu)$		$3K(1-2\nu)$	
$\lambda =$		$\mu \frac{E-2\mu}{3\mu-E}$		$K - \frac{2\mu}{3}$		$\frac{2\mu\nu}{1-2\nu}$	$\frac{E\nu}{(1+\nu)(1-2\nu)}$	$\frac{3K\nu}{1+\nu}$	$\frac{3K(3K-E)}{9K-E}$
$\mu =$			$3\frac{K-\lambda}{2}$		$\lambda \frac{1-2\nu}{2\nu}$		$\frac{E}{2+2\nu}$	$3K\frac{1-2\nu}{2+2\nu}$	$\frac{3KE}{9K-E}$
$\nu =$	$\frac{\lambda}{2(\lambda+\mu)}$	$\frac{E}{2\mu} - 1$	$\frac{\lambda}{3K-\lambda}$	$\frac{3K-2\mu}{2(3K+\mu)}$					$\frac{3K-E}{6K}$
$M =$	$\lambda + 2\mu$	$\mu \frac{4\mu-E}{3\mu-E}$	$3K - 2\lambda$	$K + \frac{4\mu}{3}$	$\lambda \frac{1-\nu}{\nu}$	$\mu \frac{2-2\nu}{1-2\nu}$	$E\frac{1-\nu}{(1+\nu)(1-2\nu)}$	$3K\frac{1-\nu}{1+\nu}$	$3K\frac{3K+E}{9K-E}$

A.2 3DEC displacement histories

The displacement histories obtained by numerical simulations in 3DEC are presented in this section. For those frequencies where models with several different zonings have been used, the displacement for the most accurate zoning (smallest distance between gridpoints) is shown. The units are seconds on the time axis and meters on the displacement axis.

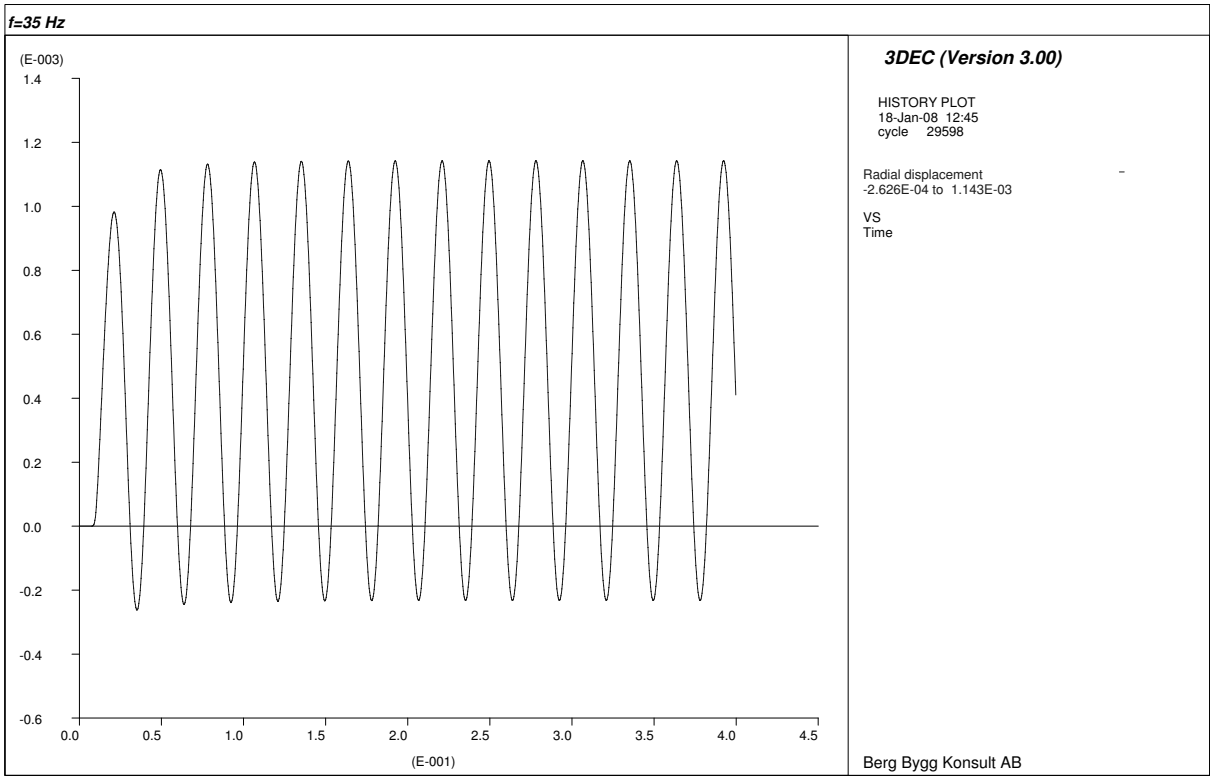

Figure A.1: Radial displacement history for 35 Hz ($r = a = 5$ m, $\theta = \pi$).

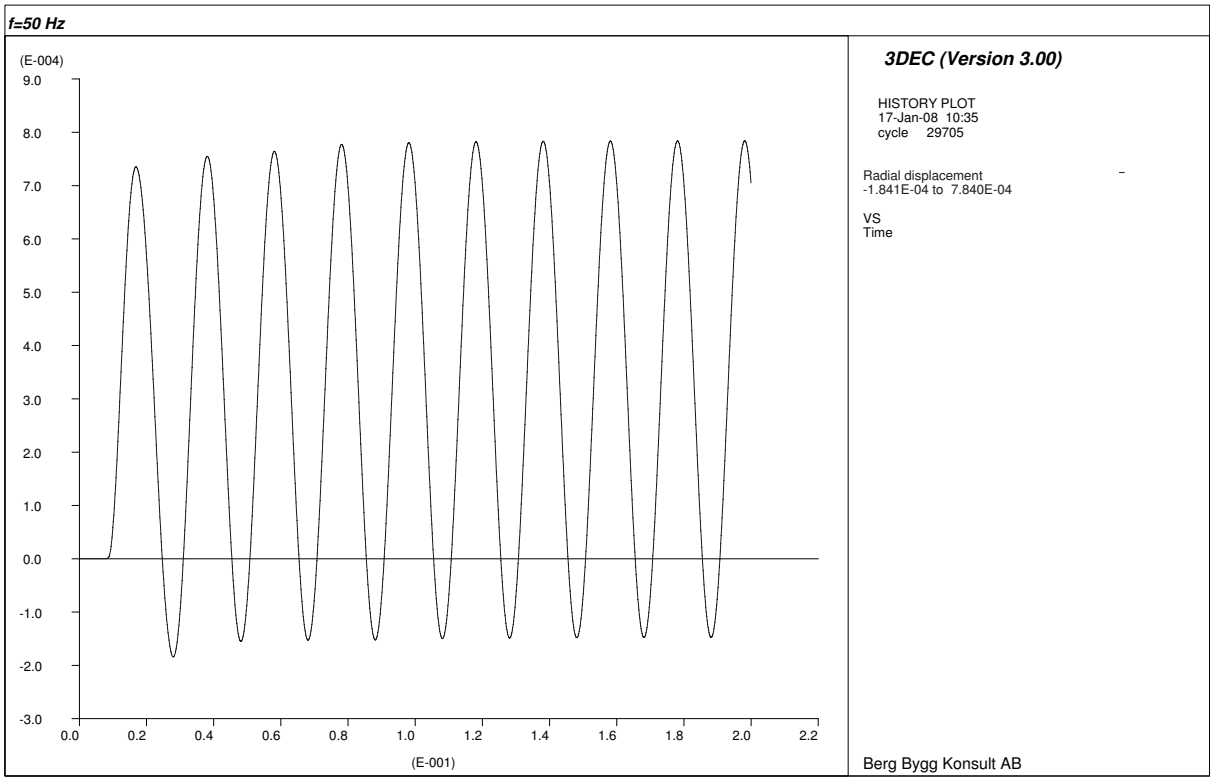

Figure A.2: Radial displacement history for 50 Hz ($r = a = 5$ m, $\theta = \pi$).

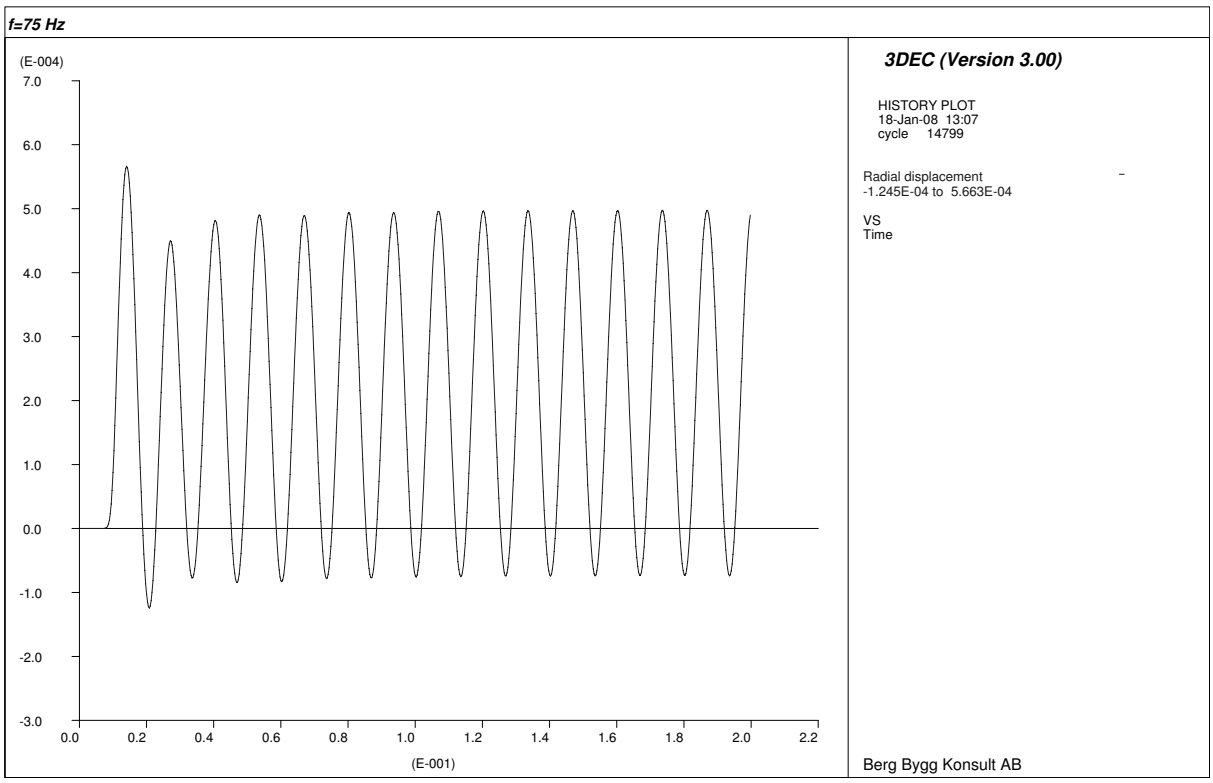

Figure A.3: Radial displacement history for 75 Hz ($r = a = 5$ m, $\theta = \pi$).

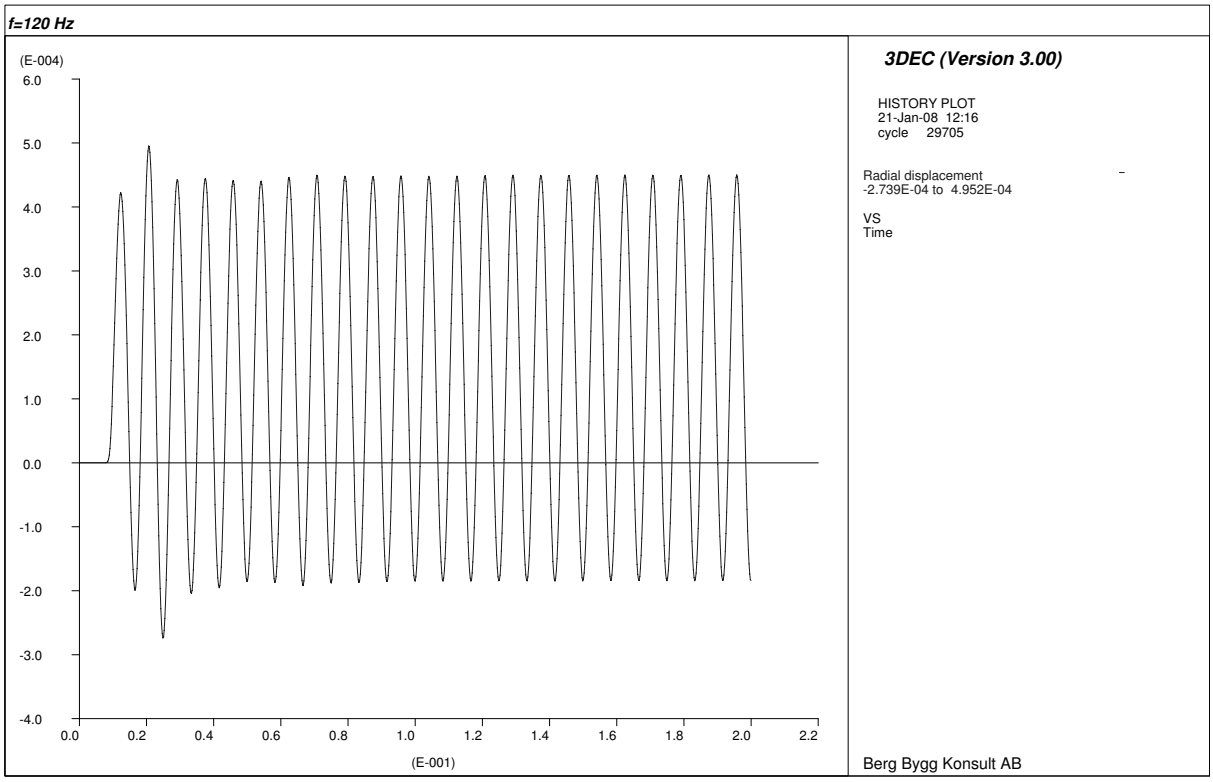

Figure A.4: Radial displacement history for 120 Hz ($r = a = 5$ m, $\theta = \pi$).

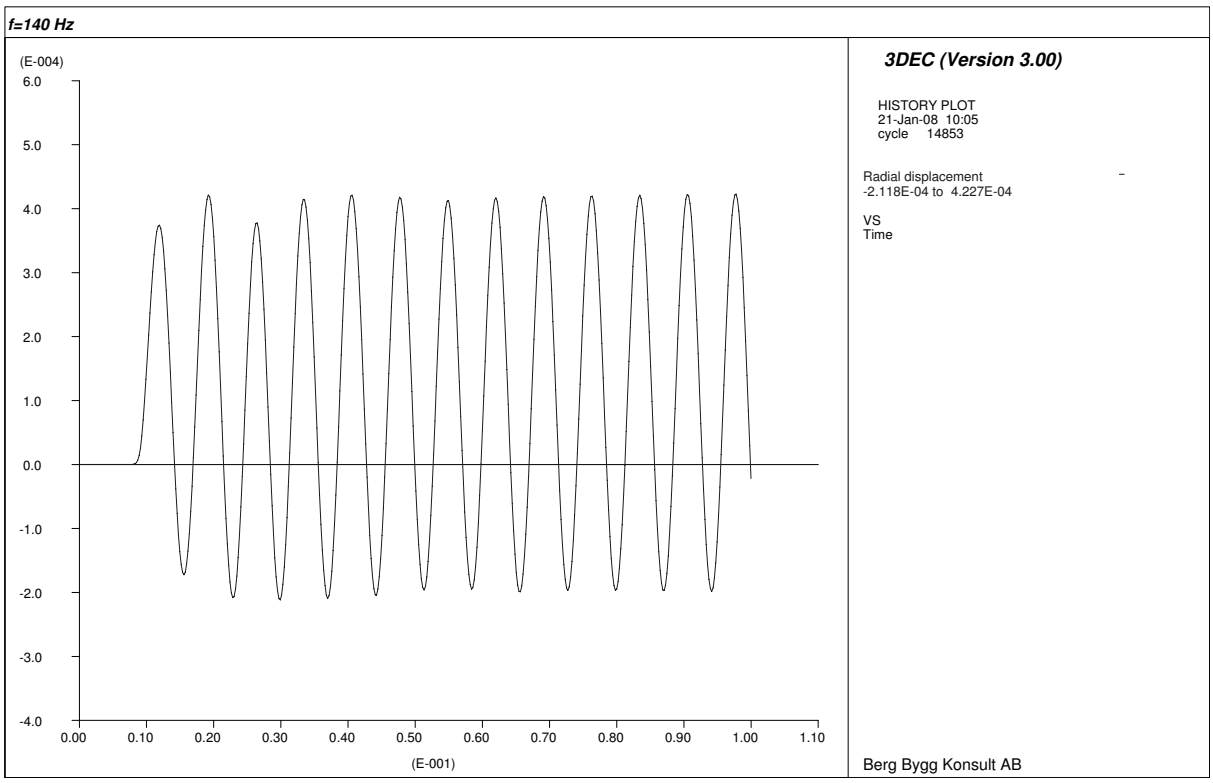

Figure A.5: Radial displacement history for 140 Hz ($r = a = 5$ m, $\theta = \pi$).

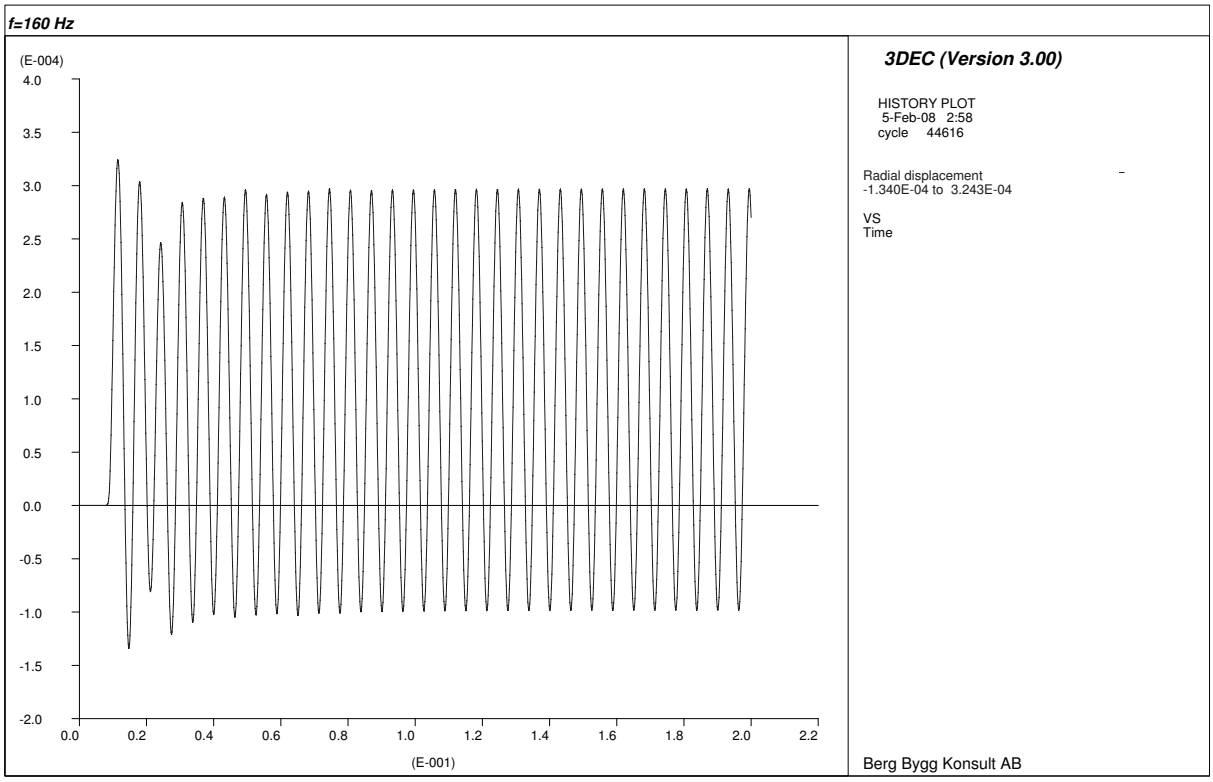

Figure A.6: Radial displacement history for 160 Hz ($r = a = 5$ m, $\theta = \pi$).

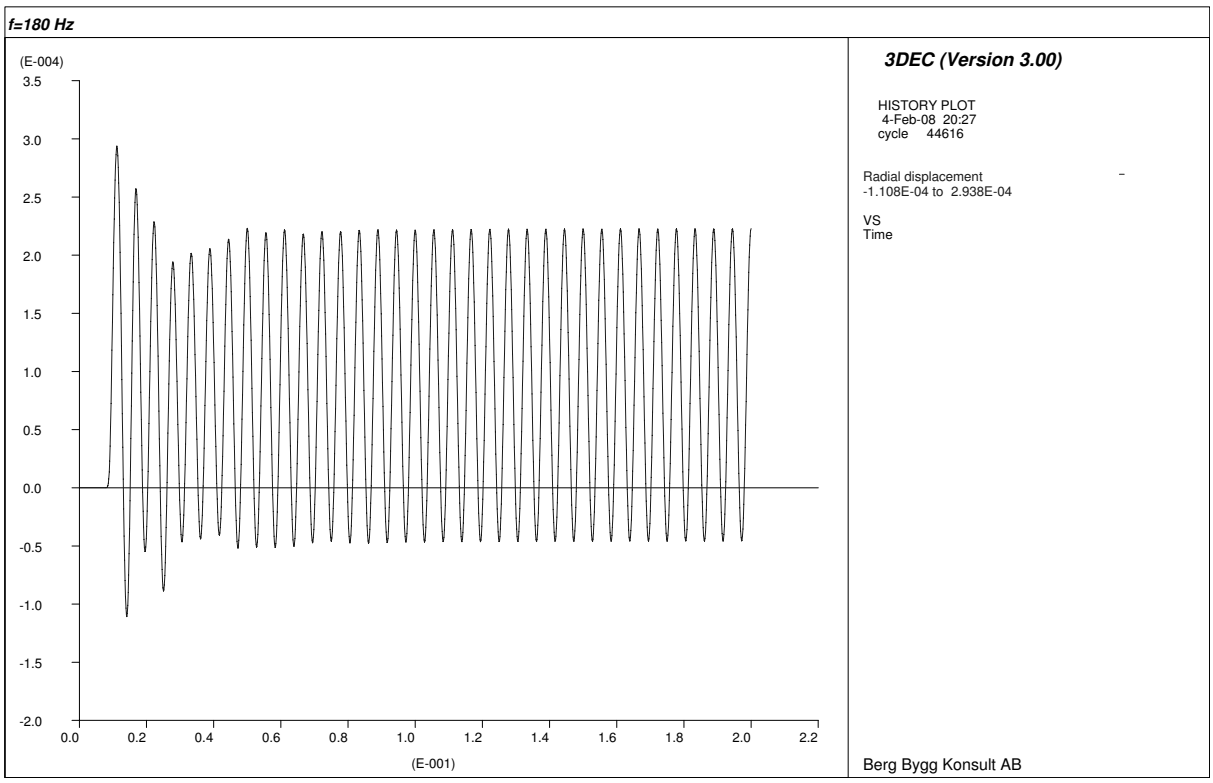

Figure A.7: Radial displacement history for 180 Hz ($r = a = 5$ m, $\theta = \pi$).

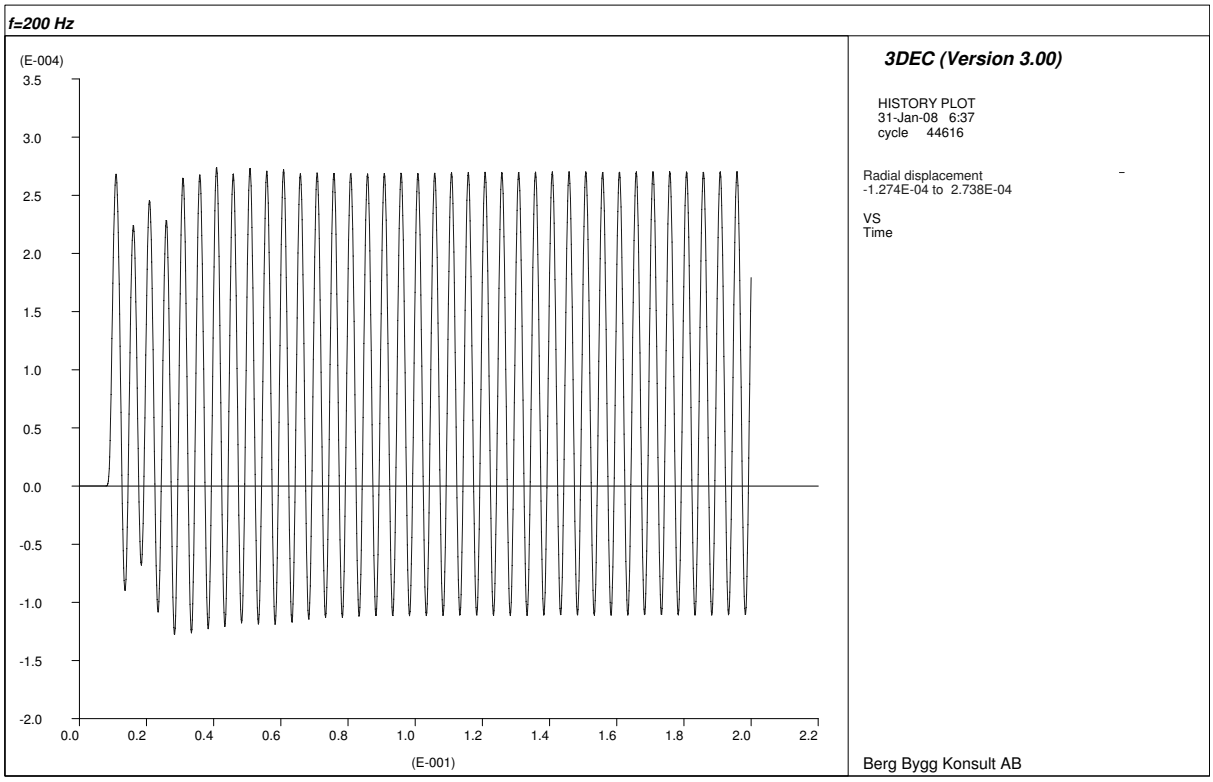

Figure A.8: Radial displacement history for 200 Hz ($r = a = 5$ m, $\theta = \pi$).

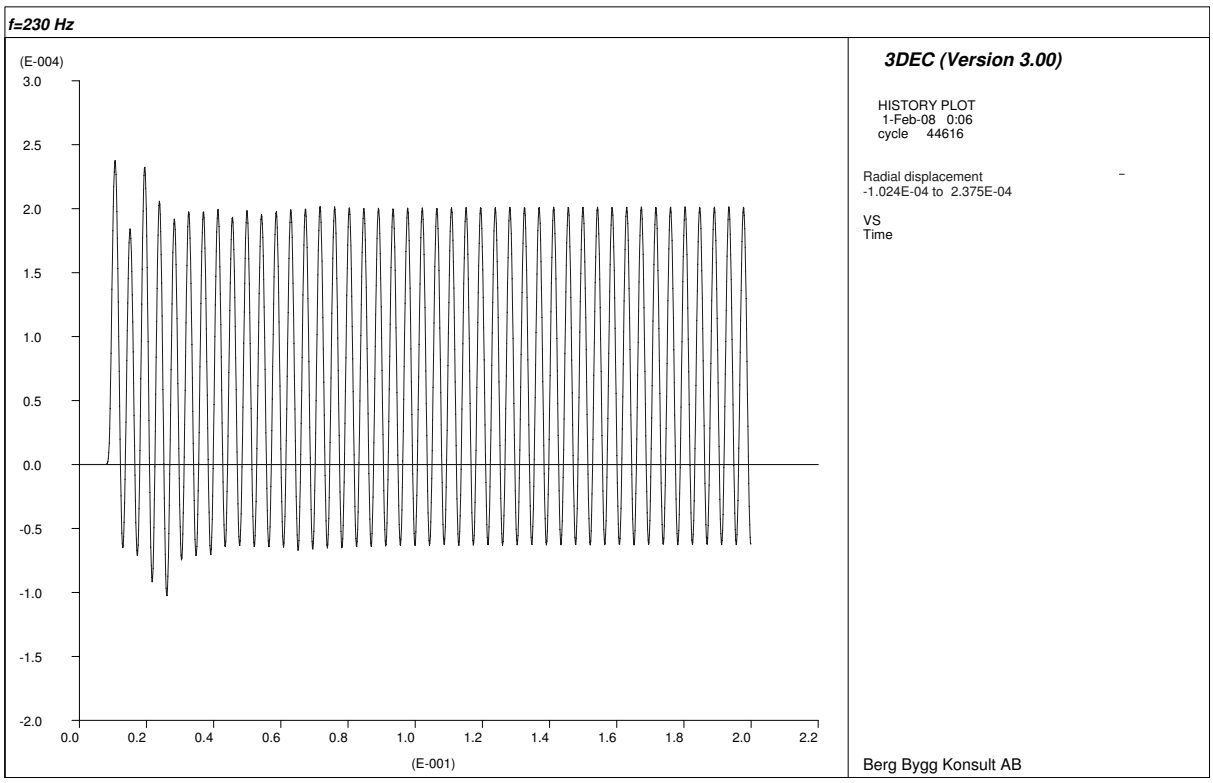

Figure A.9: Radial displacement history for 230 Hz ($r = a = 5$ m, $\theta = \pi$).

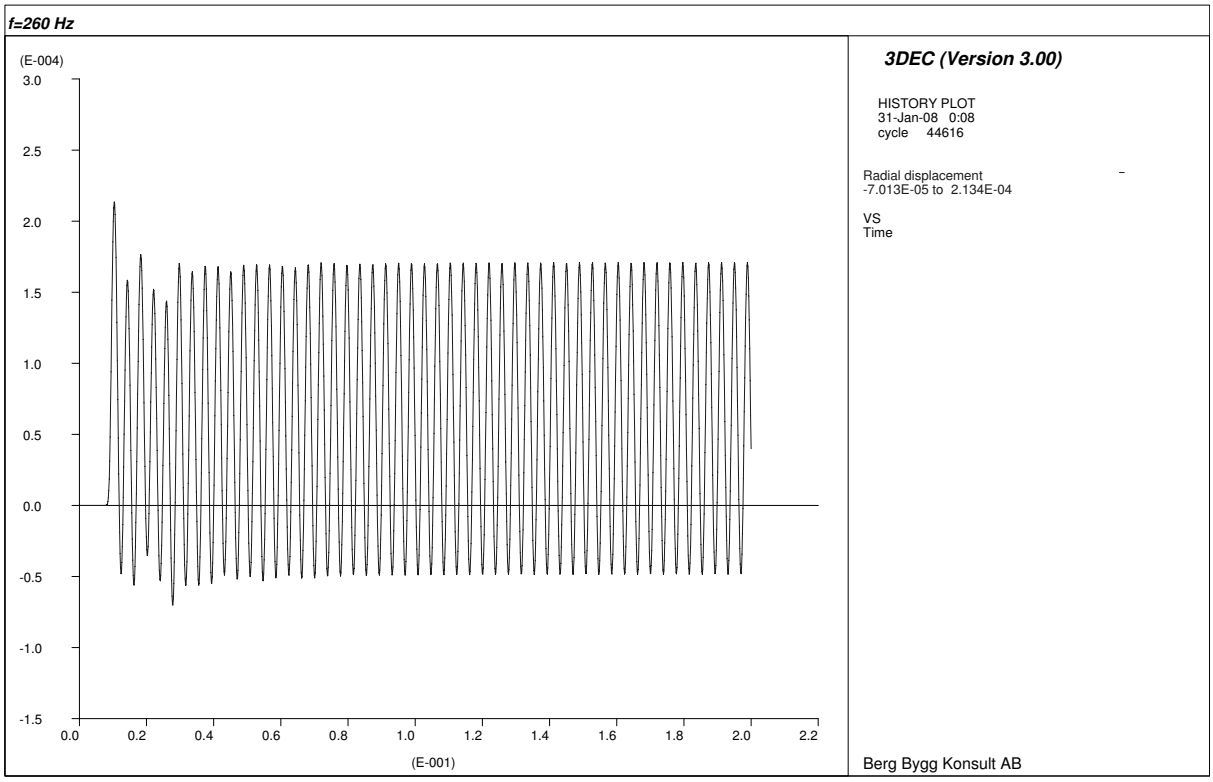

Figure A.10: Radial displacement history for 260 Hz ($r = a = 5$ m, $\theta = \pi$).

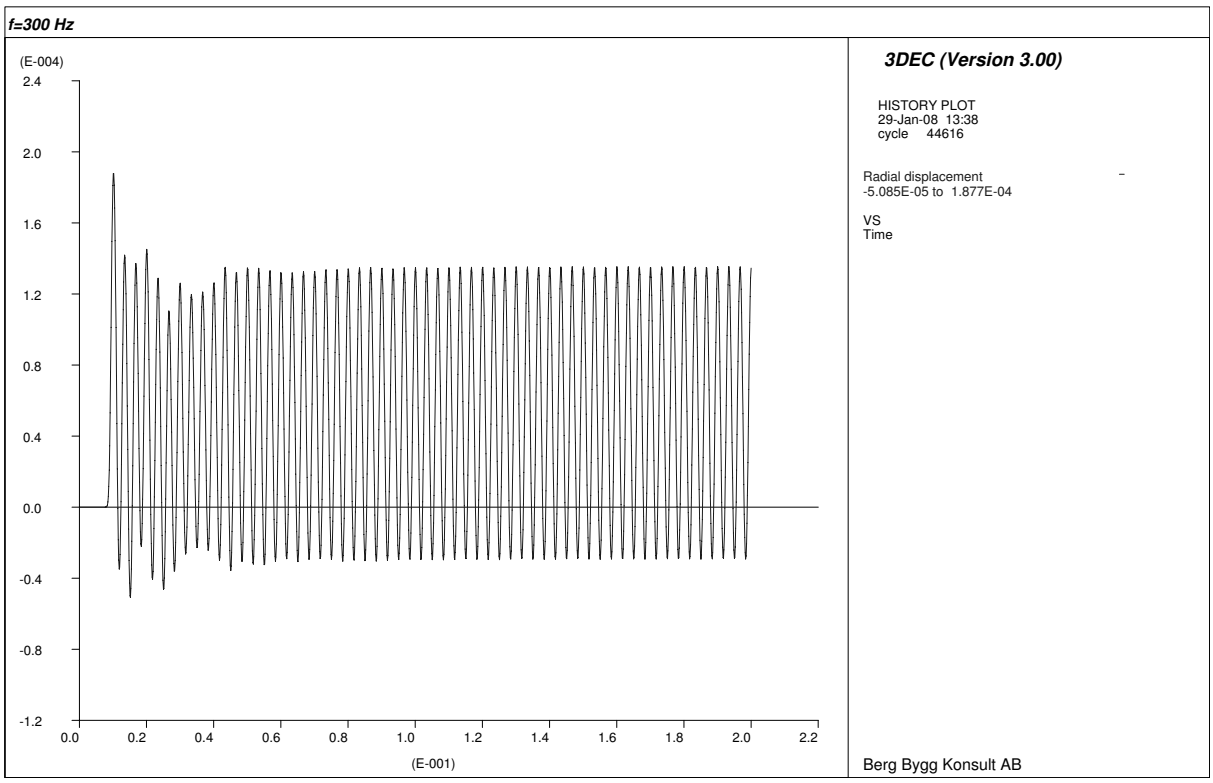

Figure A.11: Radial displacement history for 300 Hz ($r = a = 5$ m, $\theta = \pi$).

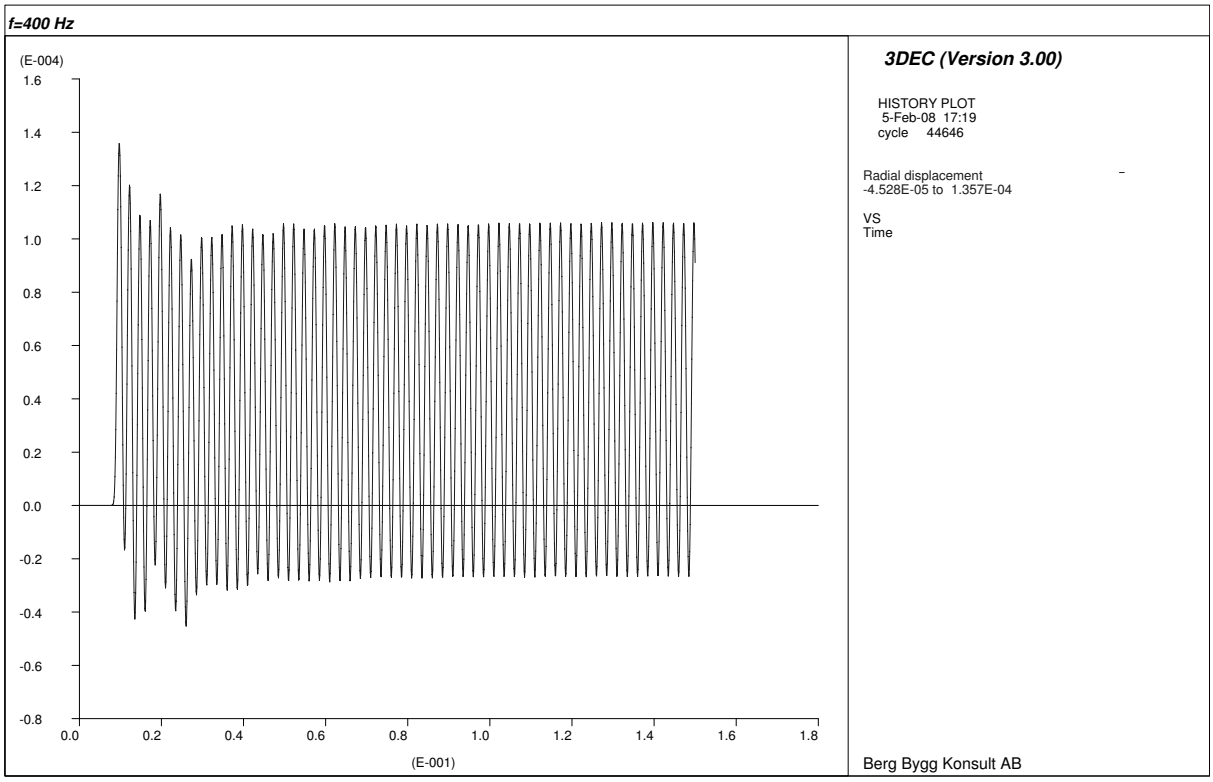

Figure A.12: Radial displacement history for 400 Hz ($r = a = 5$ m, $\theta = \pi$).

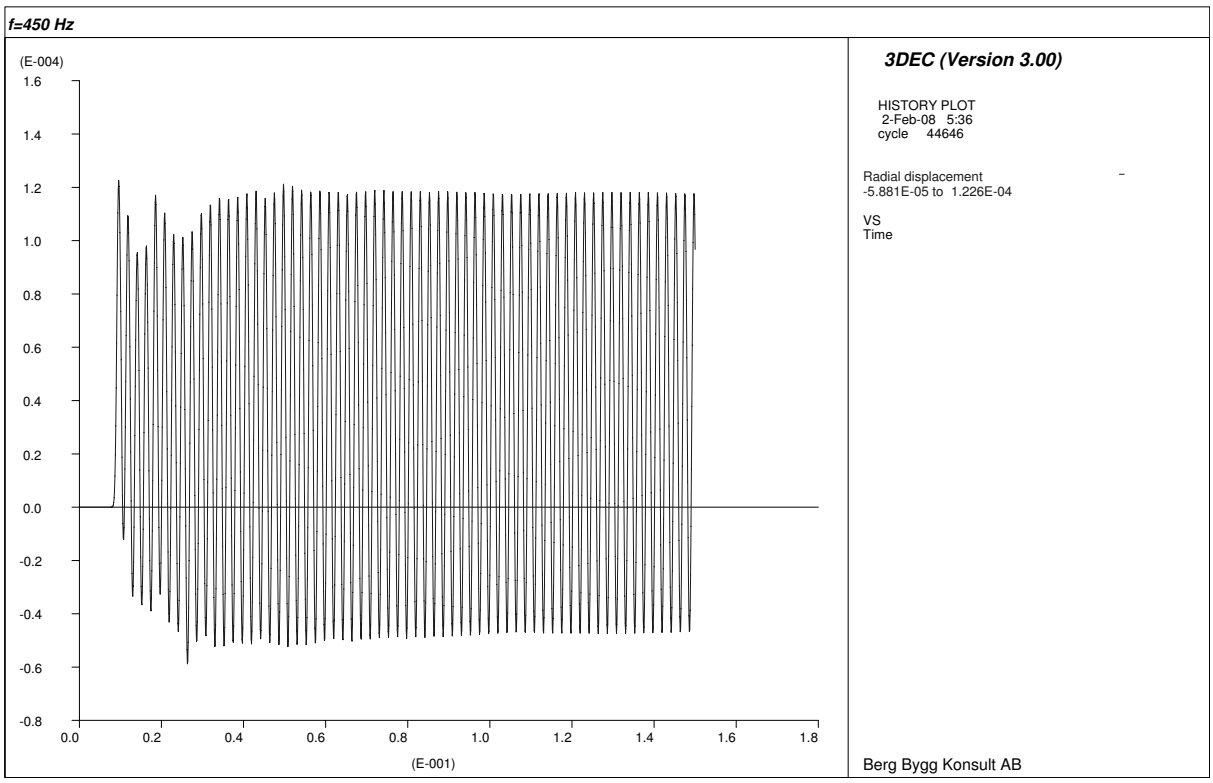

Figure A.13: Radial displacement history for 450 Hz ($r = a = 5$ m, $\theta = \pi$).

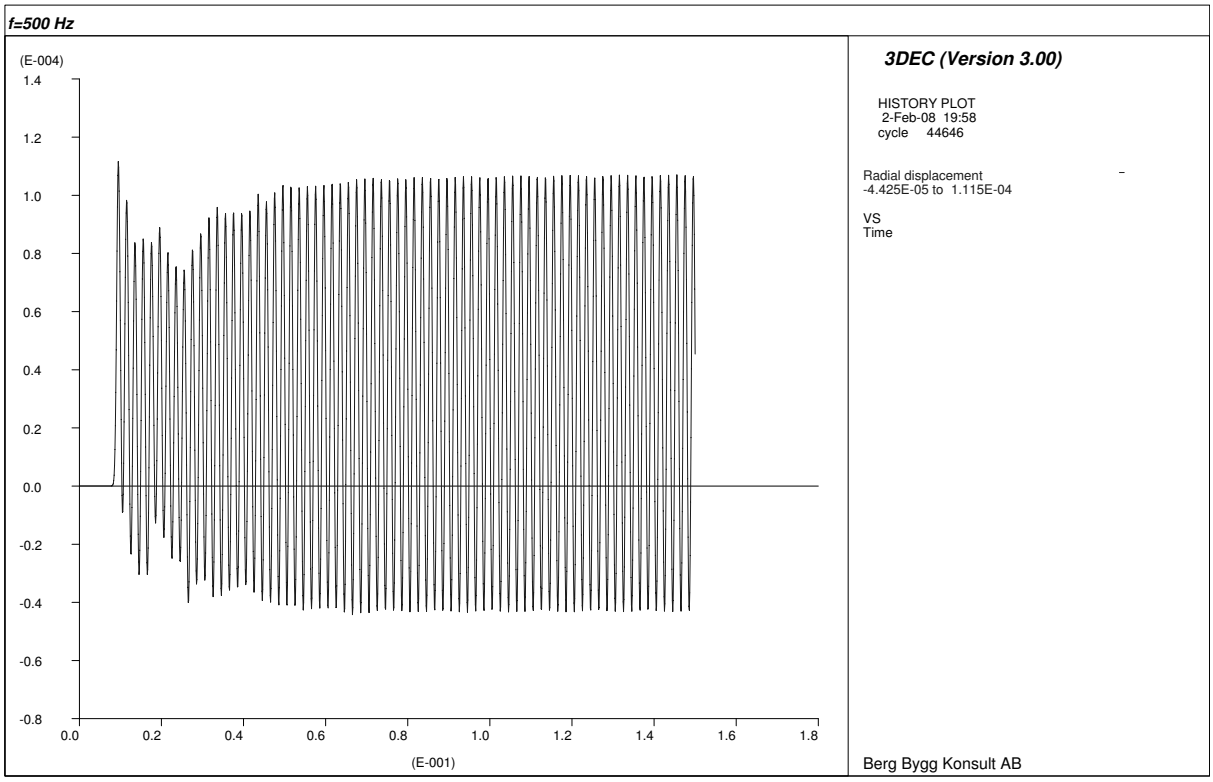

Figure A.14: Radial displacement history for 500 Hz ($r = a = 5$ m, $\theta = \pi$).

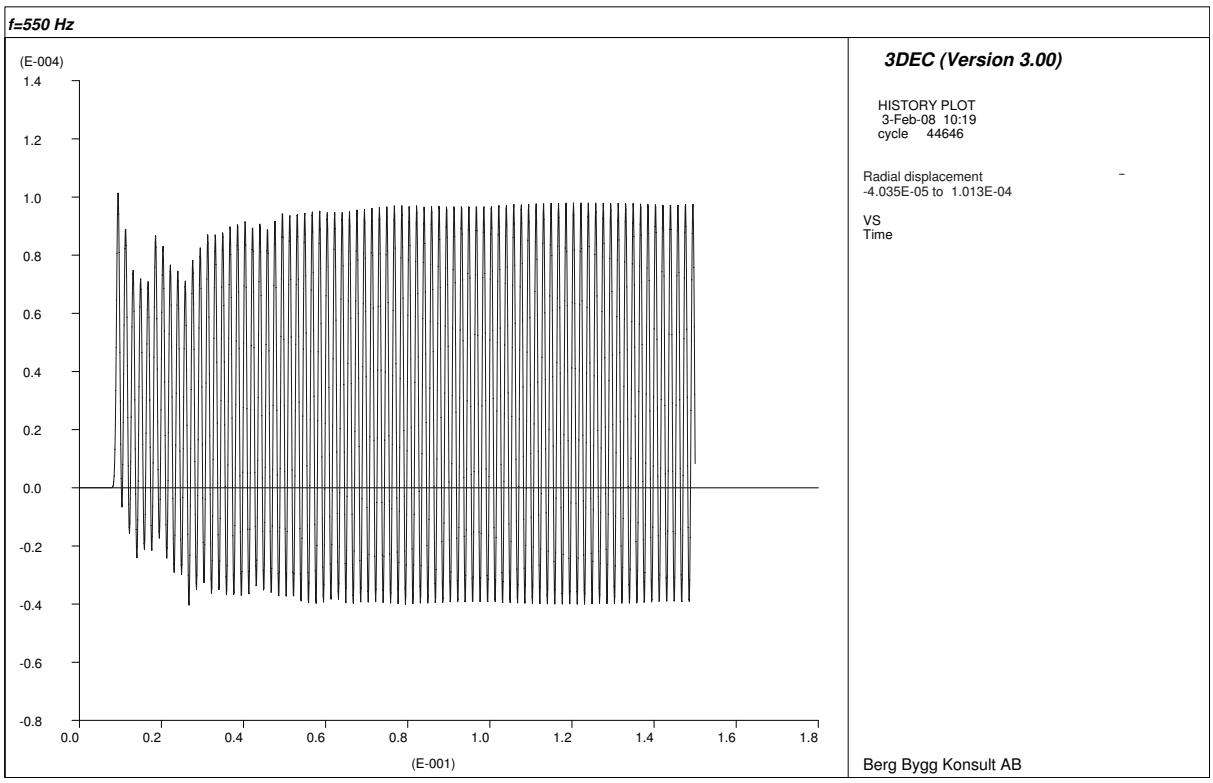

Figure A.15: Radial displacement history for 550 Hz ($r = a = 5$ m, $\theta = \pi$).

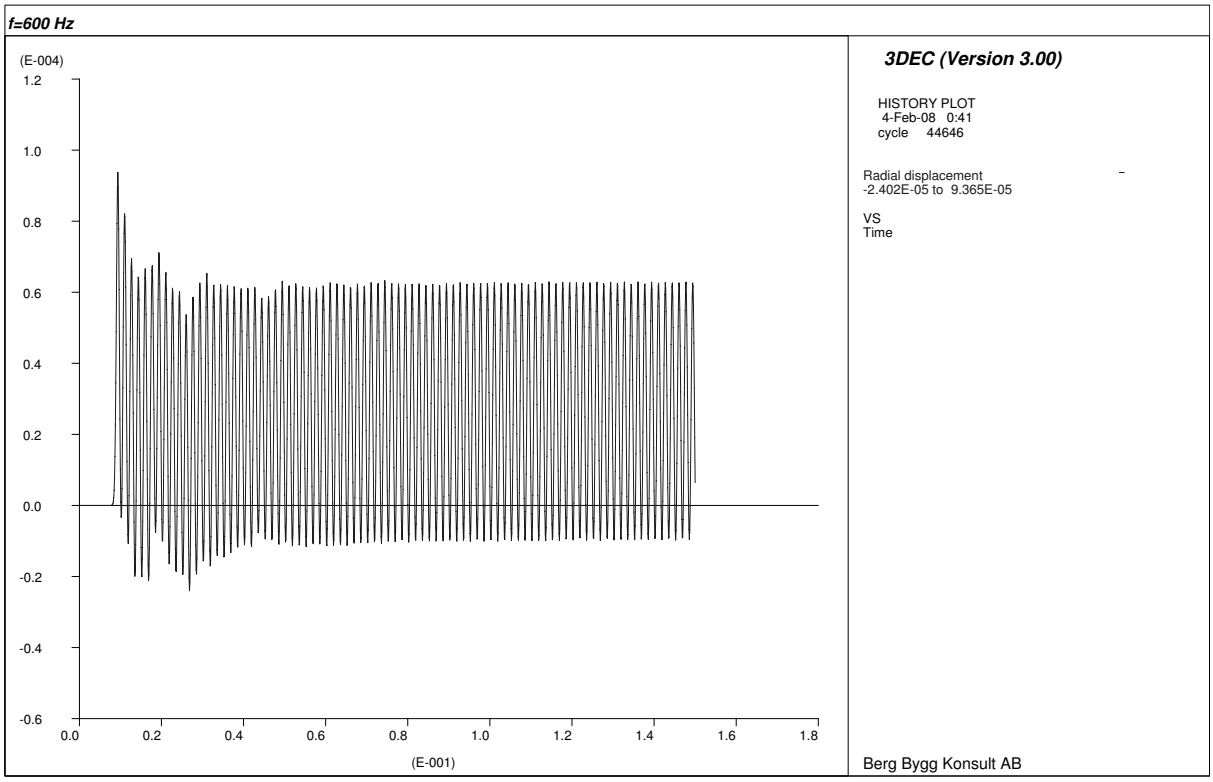

Figure A.16: Radial displacement history for 600 Hz ($r = a = 5$ m, $\theta = \pi$).

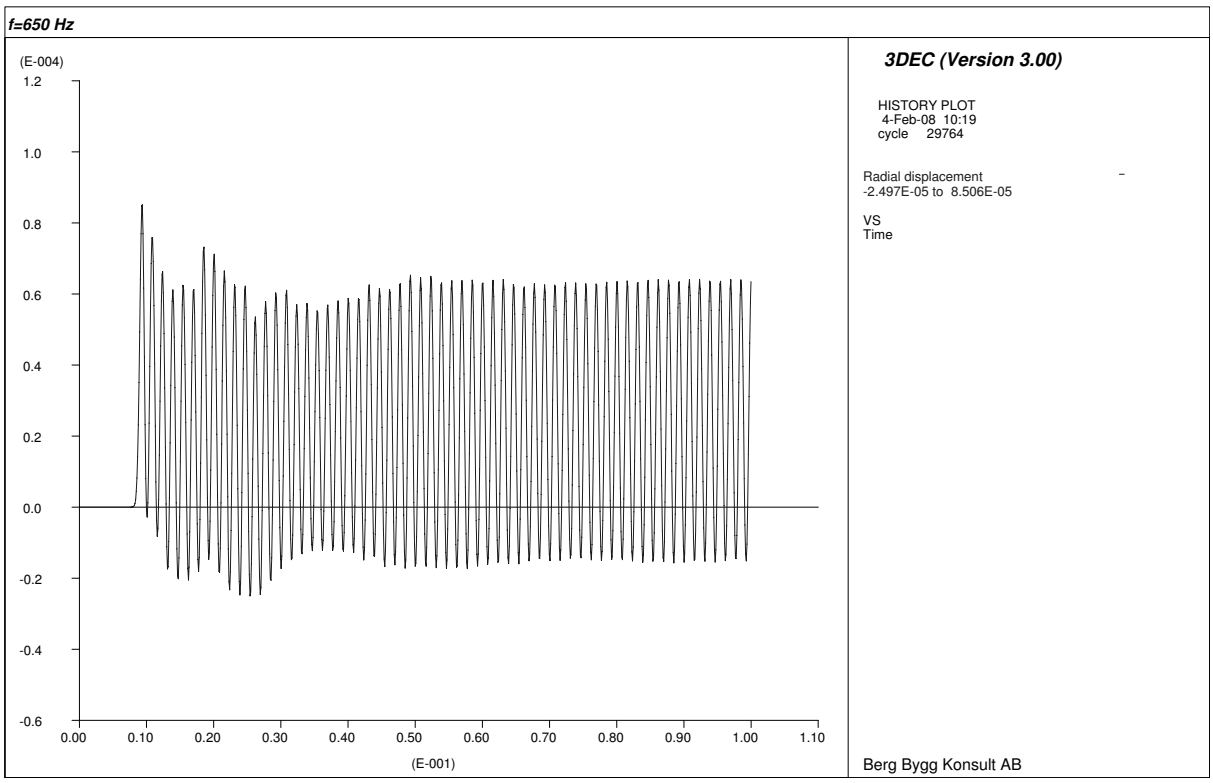

Figure A.17: Radial displacement history for 650 Hz ($r = a = 5$ m, $\theta = \pi$).

A.3 3DEC stress histories

The tangential stress histories obtained by numerical simulations in 3DEC are presented in this section. As in the previous section, when several zonings have been used for the same frequency, the stress for the most accurate zoning is shown. The units are seconds on the time axis and Pascal on the stress axis.

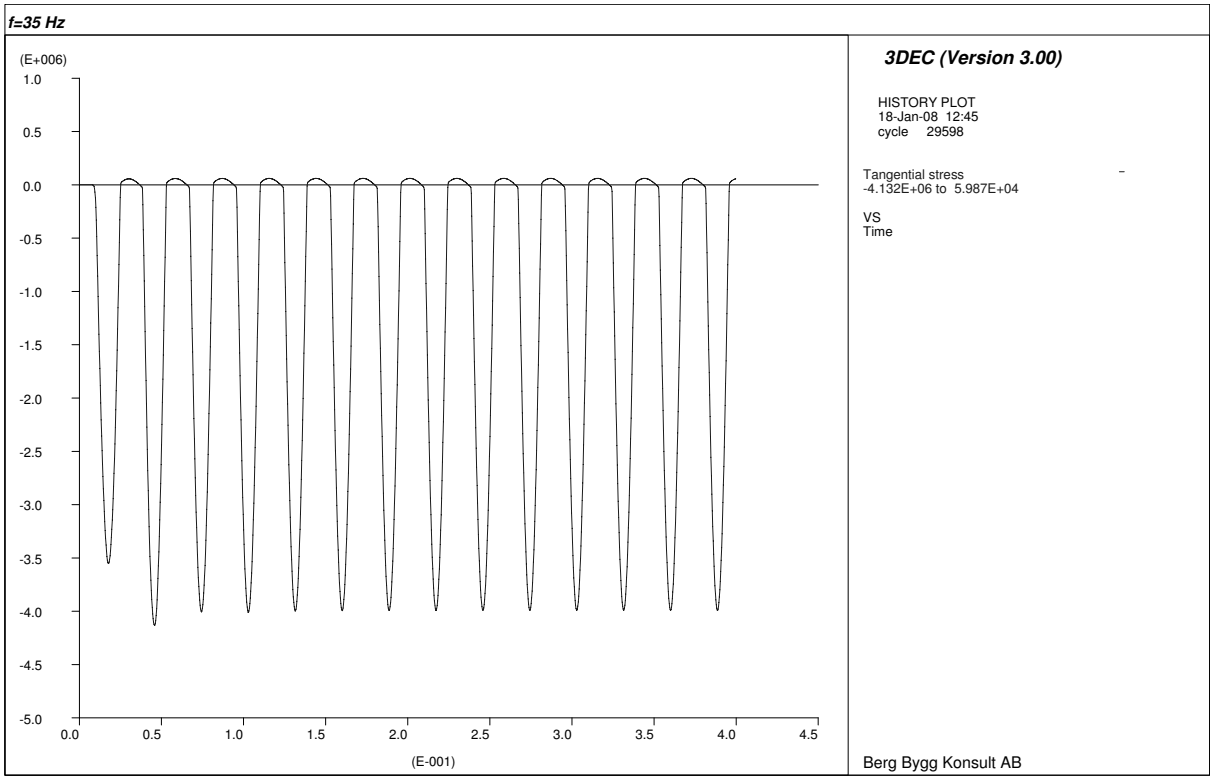

Figure A.18: Tangential stress history for 35 Hz ($r = a = 5$ m, $\theta = \pi/2$).

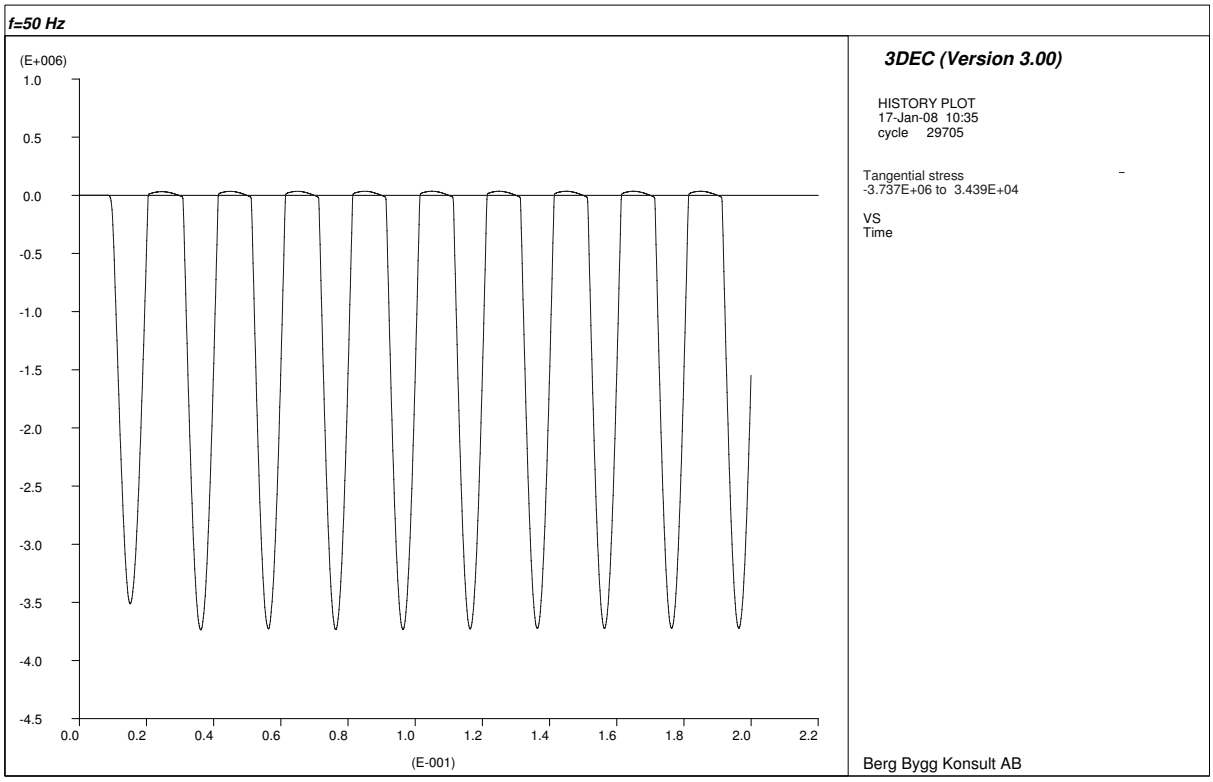

Figure A.19: Tangential stress history for 50 Hz ($r = a = 5$ m, $\theta = \pi/2$).

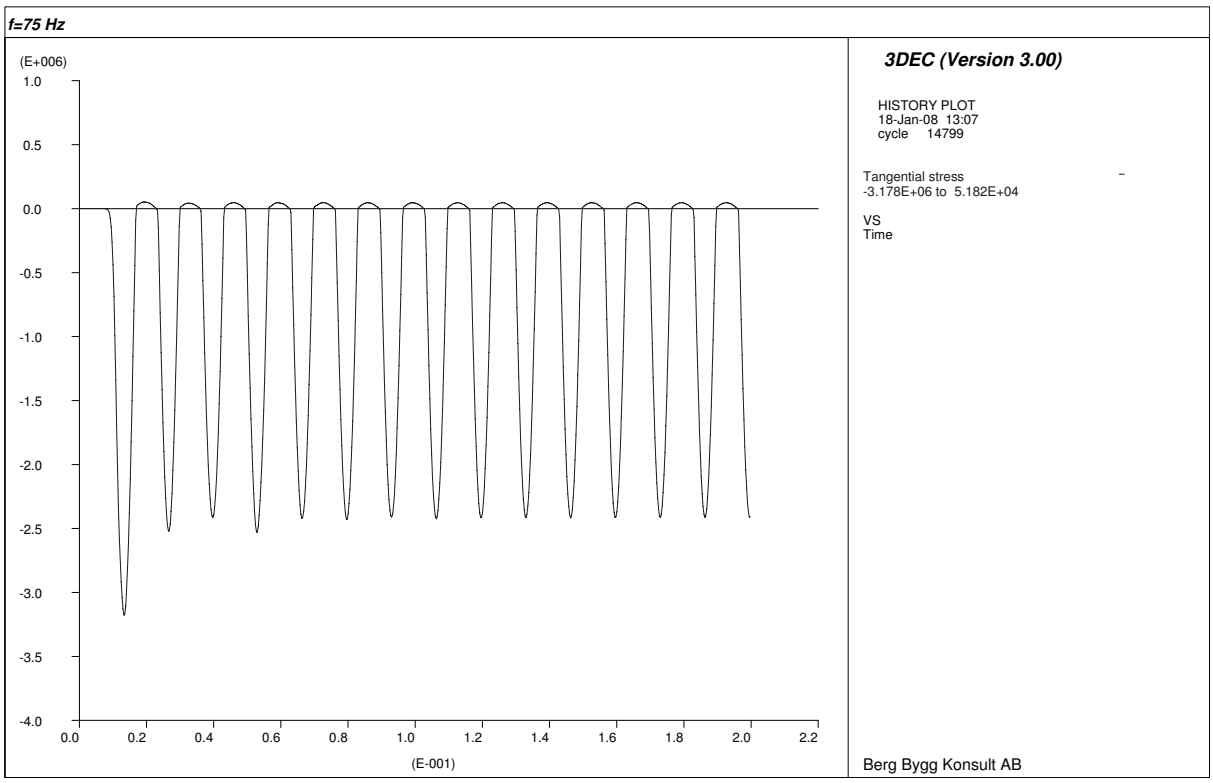

Figure A.20: Tangential stress history for 75 Hz ($r = a = 5$ m, $\theta = \pi/2$).

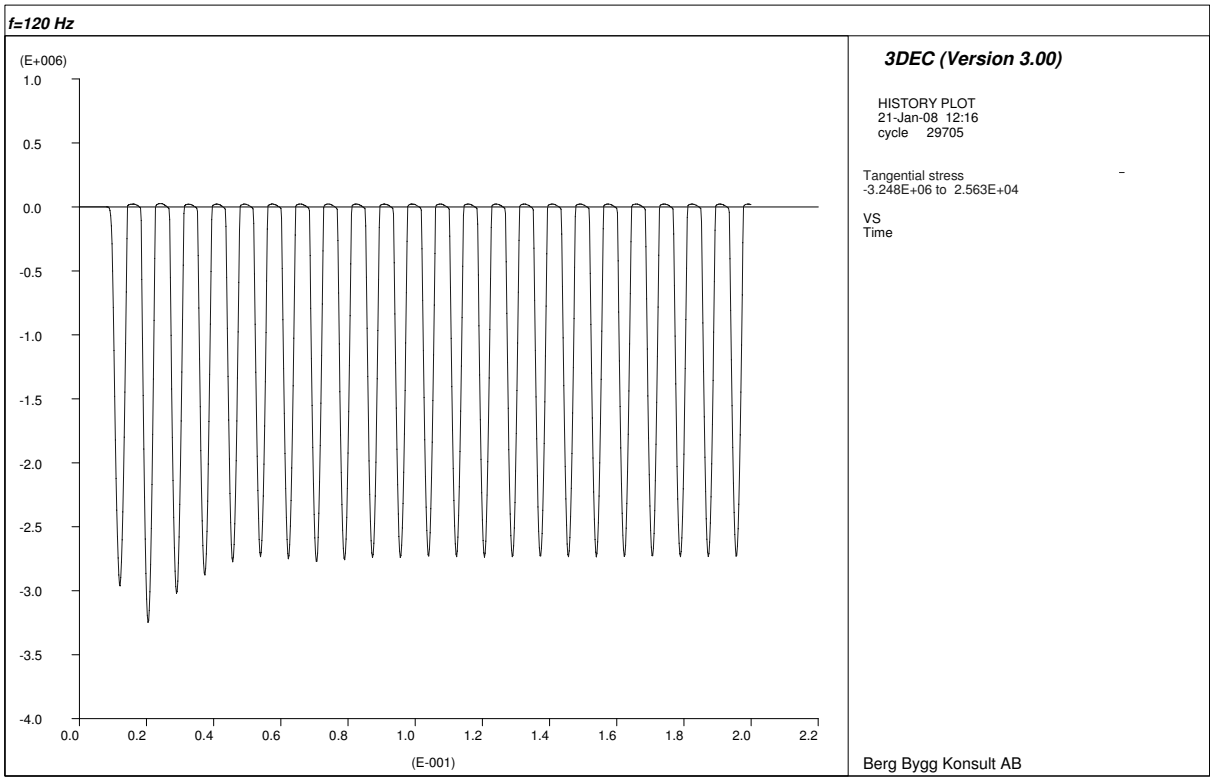

Figure A.21: Tangential stress history for 120 Hz ($r = a = 5$ m, $\theta = \pi/2$).

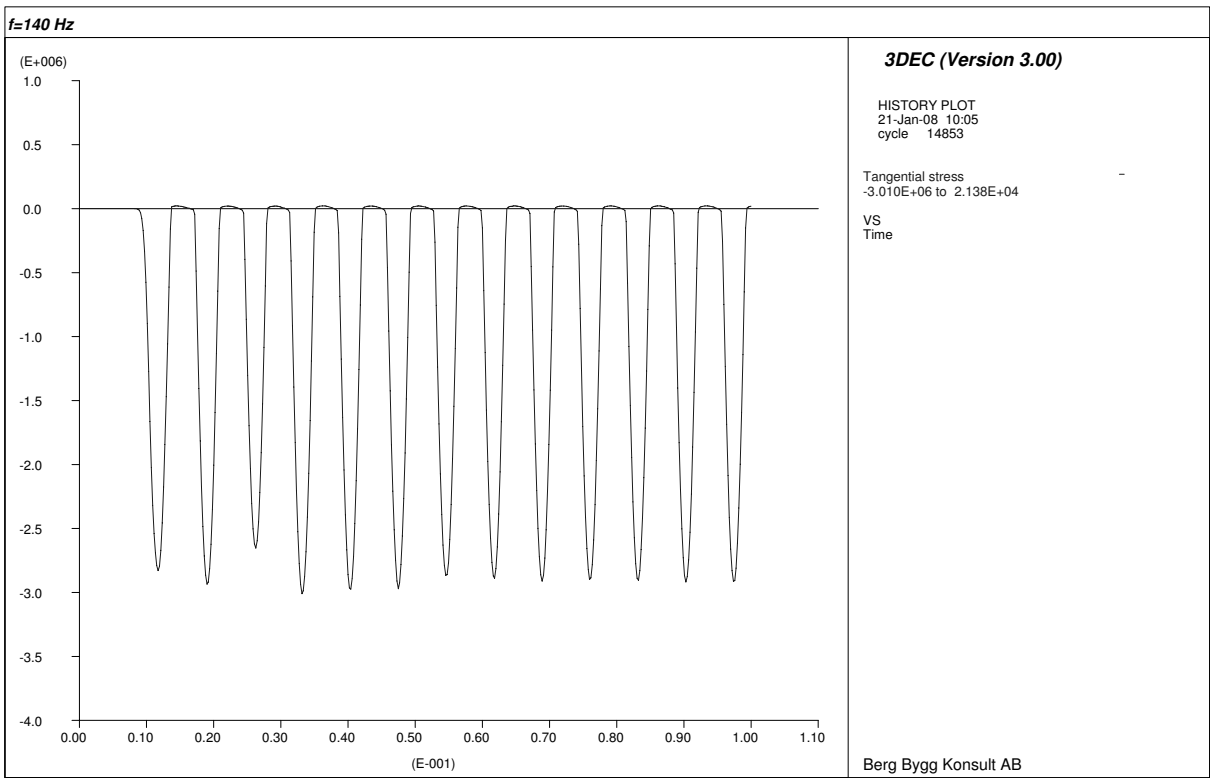

Figure A.22: Tangential stress history for 140 Hz ($r = a = 5$ m, $\theta = \pi/2$).

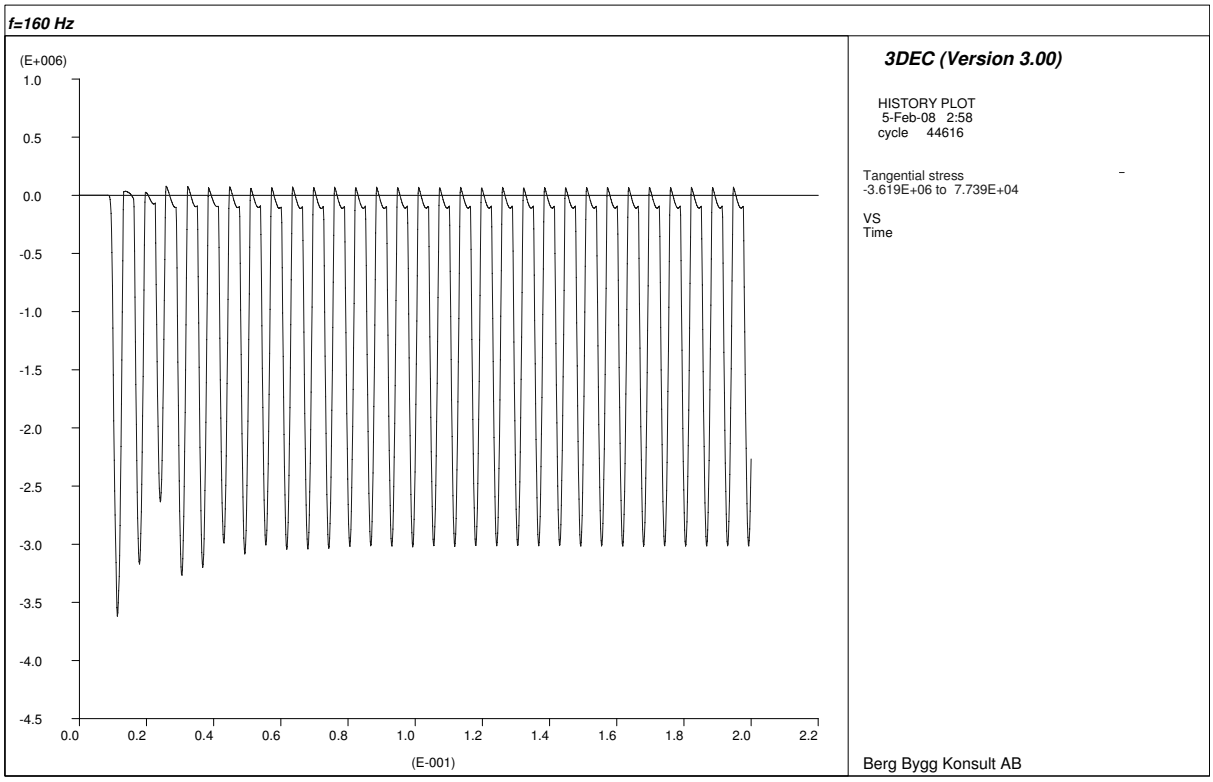

Figure A.23: Tangential stress history for 160 Hz ($r = a = 5$ m, $\theta = \pi/2$).

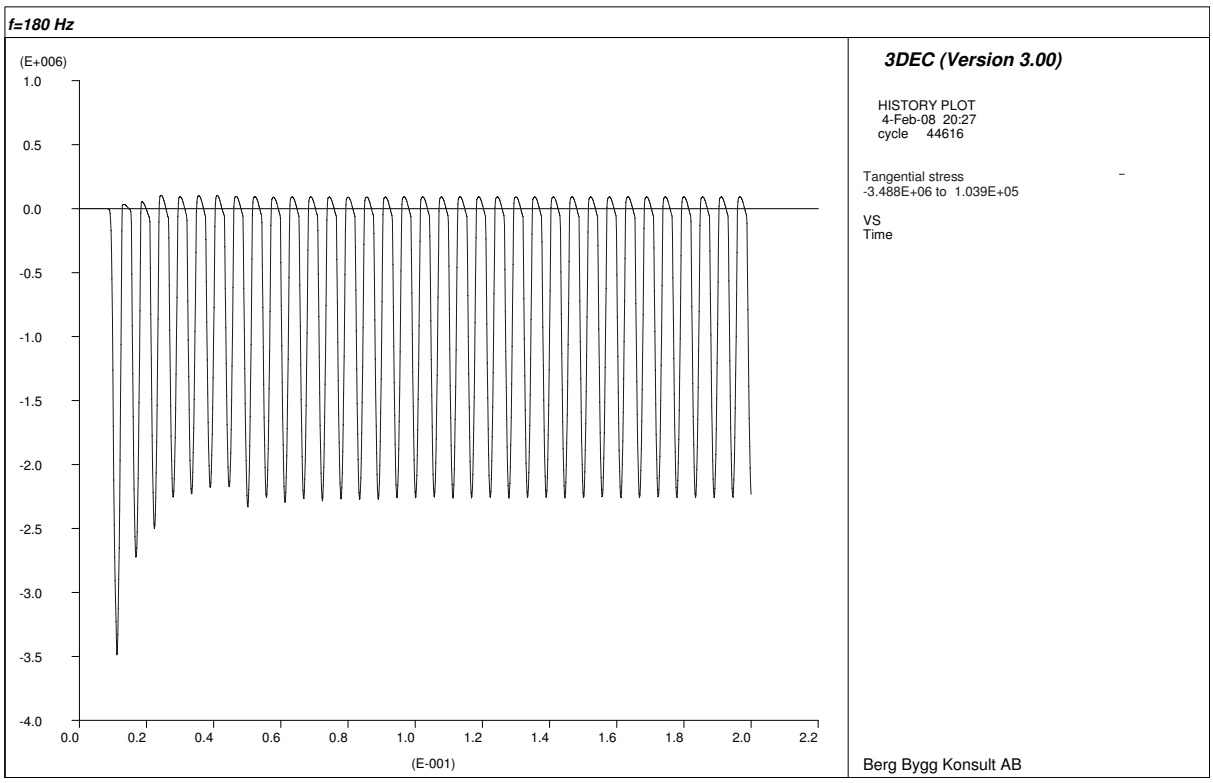

Figure A.24: Tangential stress history for 180 Hz ($r = a = 5$ m, $\theta = \pi/2$).

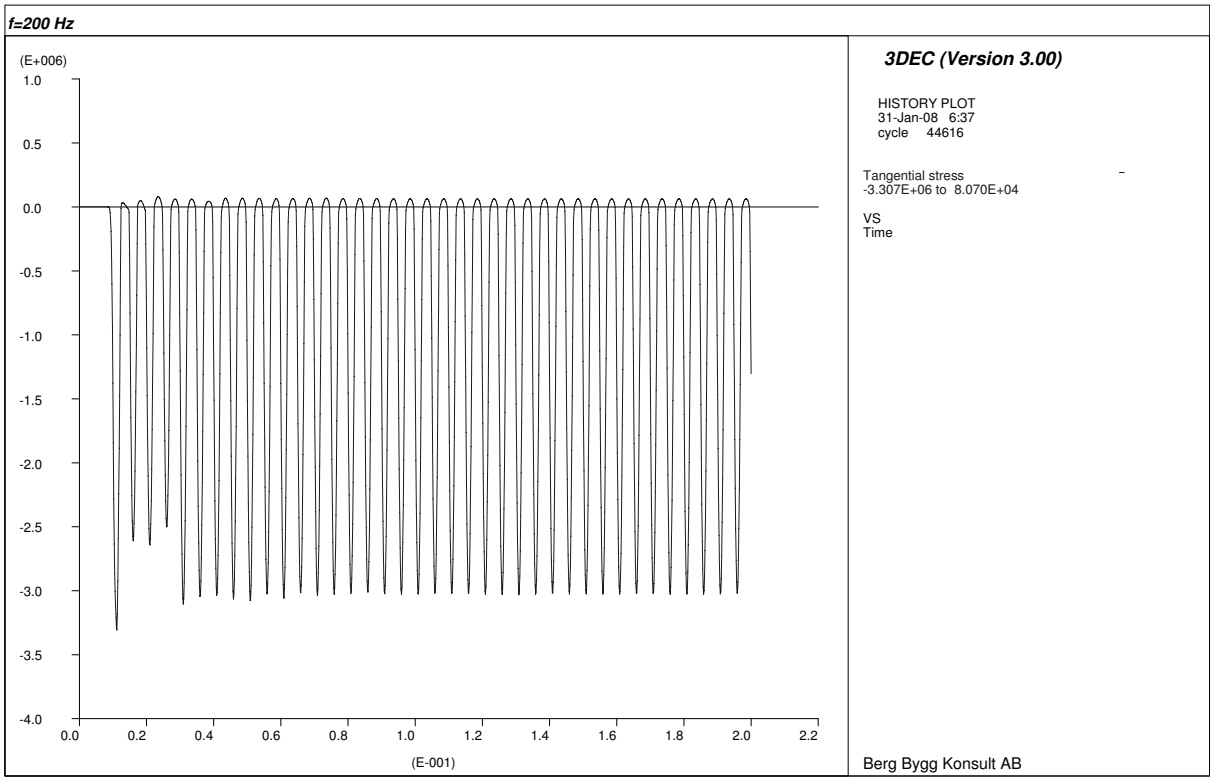

Figure A.25: Tangential stress history for 200 Hz ($r = a = 5$ m, $\theta = \pi/2$).

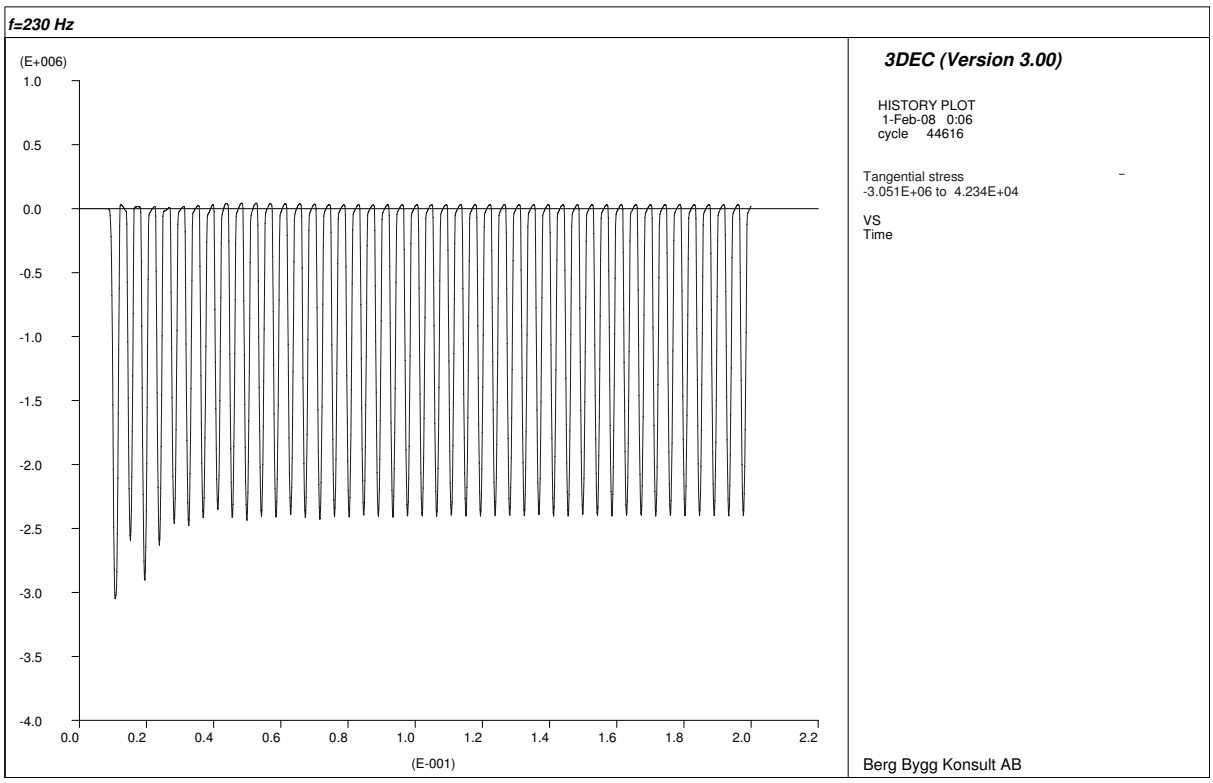

Figure A.26: Tangential stress history for 230 Hz ($r = a = 5$ m, $\theta = \pi/2$).

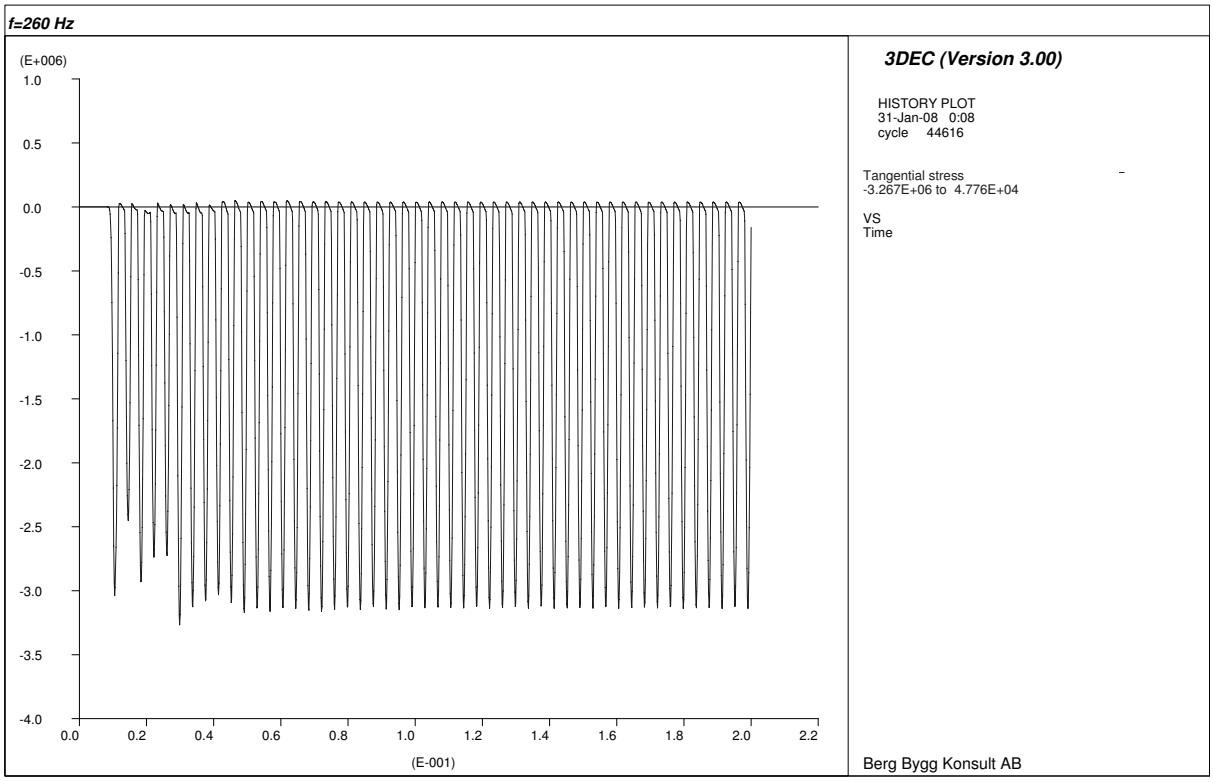

Figure A.27: Tangential stress history for 260 Hz ($r = a = 5$ m, $\theta = \pi/2$).

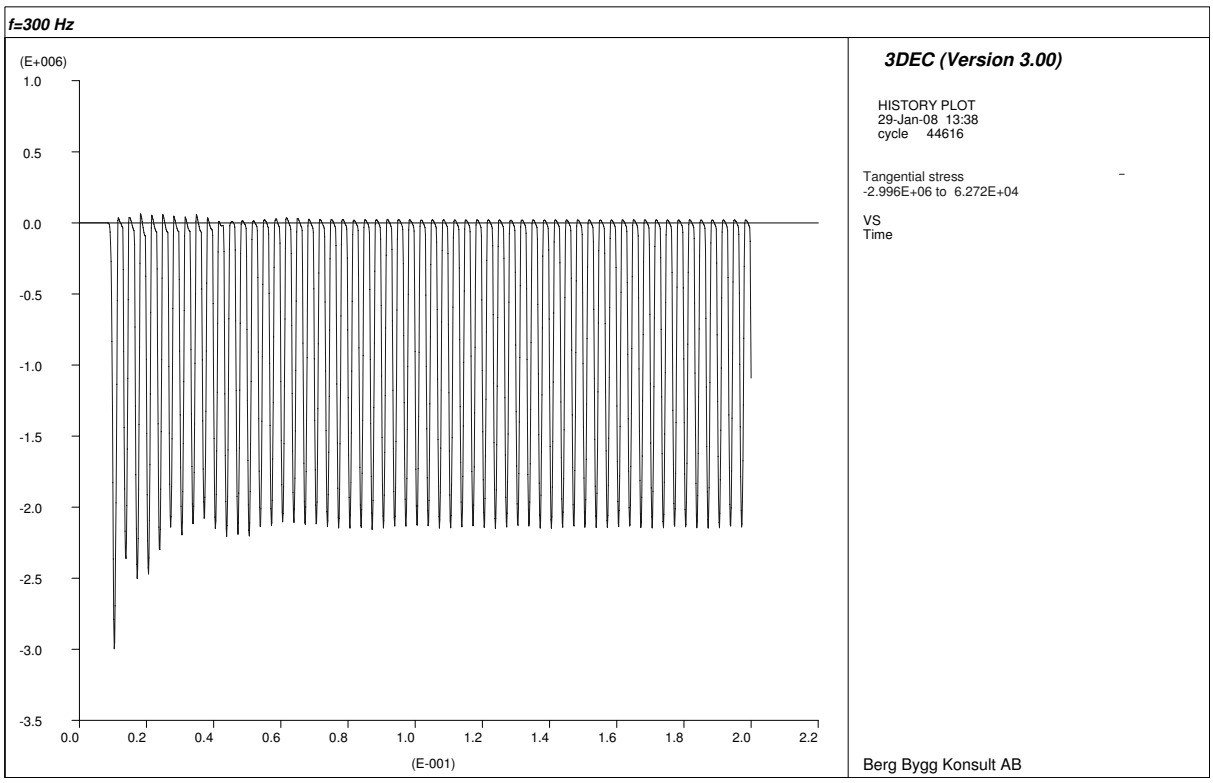

Figure A.28: Tangential stress history for 300 Hz ($r = a = 5$ m, $\theta = \pi/2$).

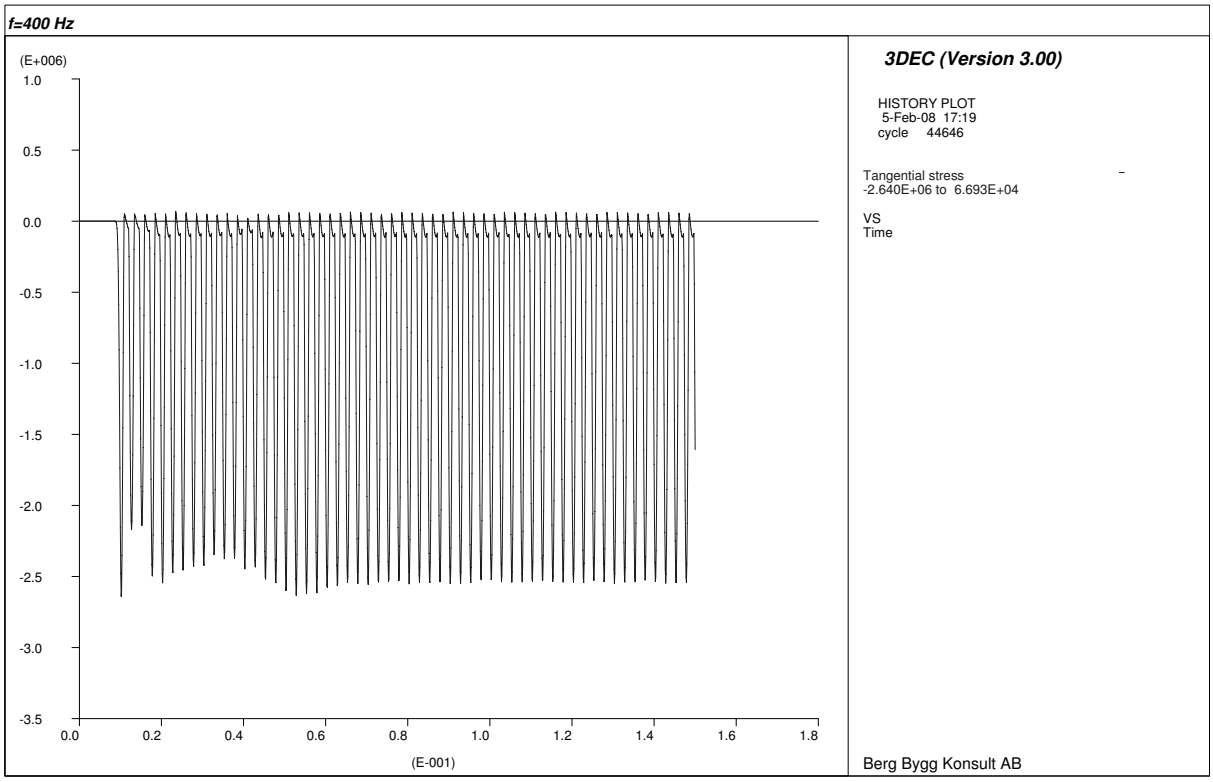

Figure A.29: Tangential stress history for 400 Hz ($r = a = 5$ m, $\theta = \pi/2$).

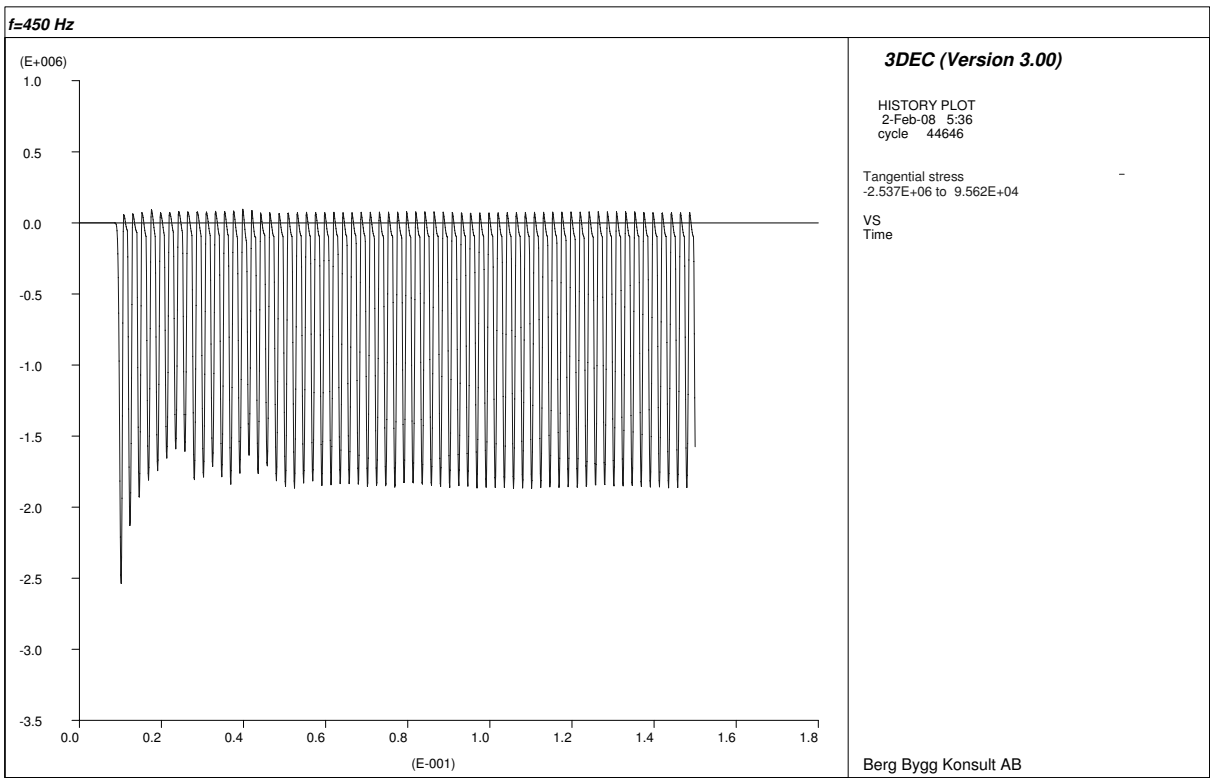

Figure A.30: Tangential stress history for 450 Hz ($r = a = 5$ m, $\theta = \pi/2$).

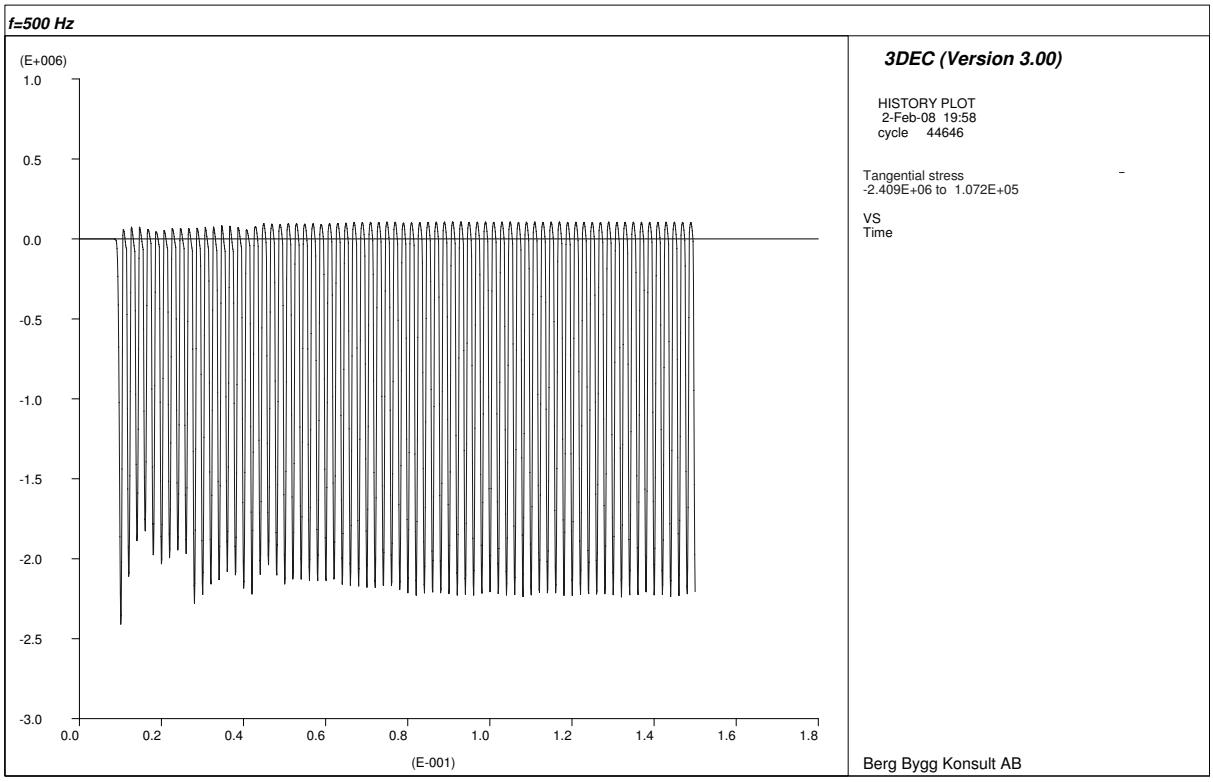

Figure A.31: Tangential stress history for 500 Hz ($r = a = 5$ m, $\theta = \pi/2$).

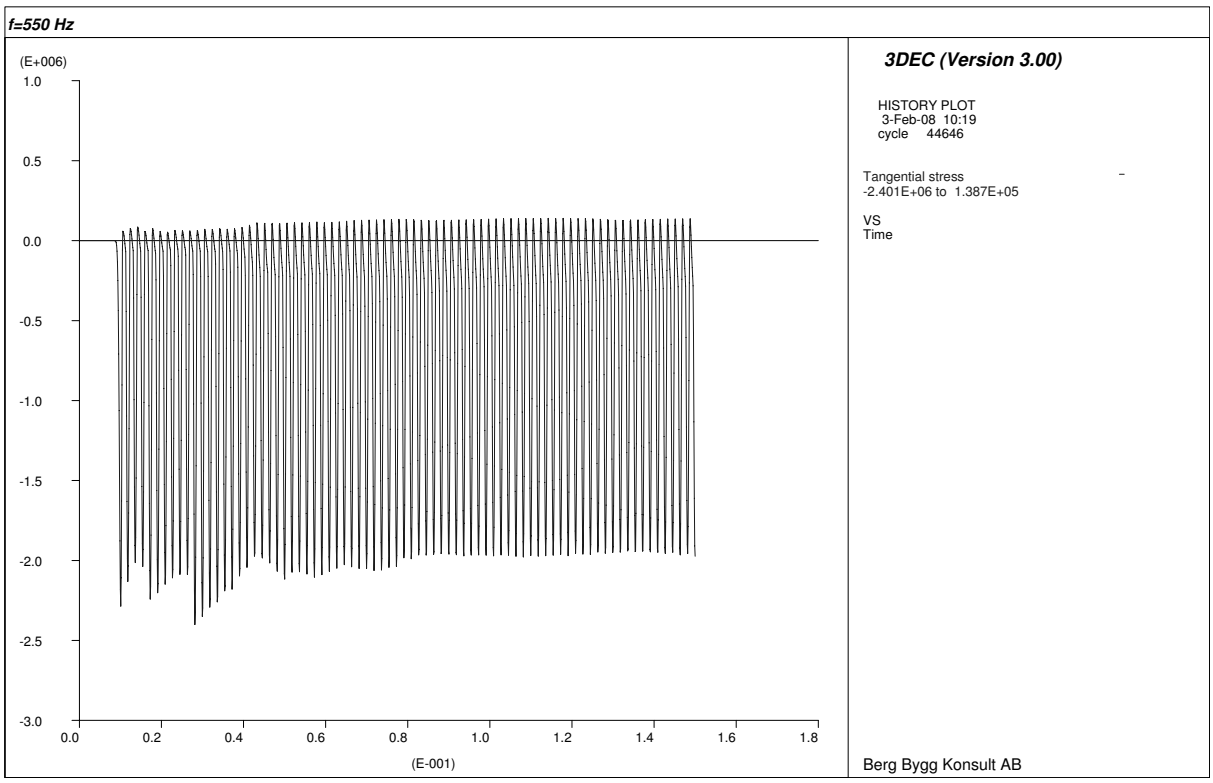

Figure A.32: Tangential stress history for 550 Hz ($r = a = 5$ m, $\theta = \pi/2$).

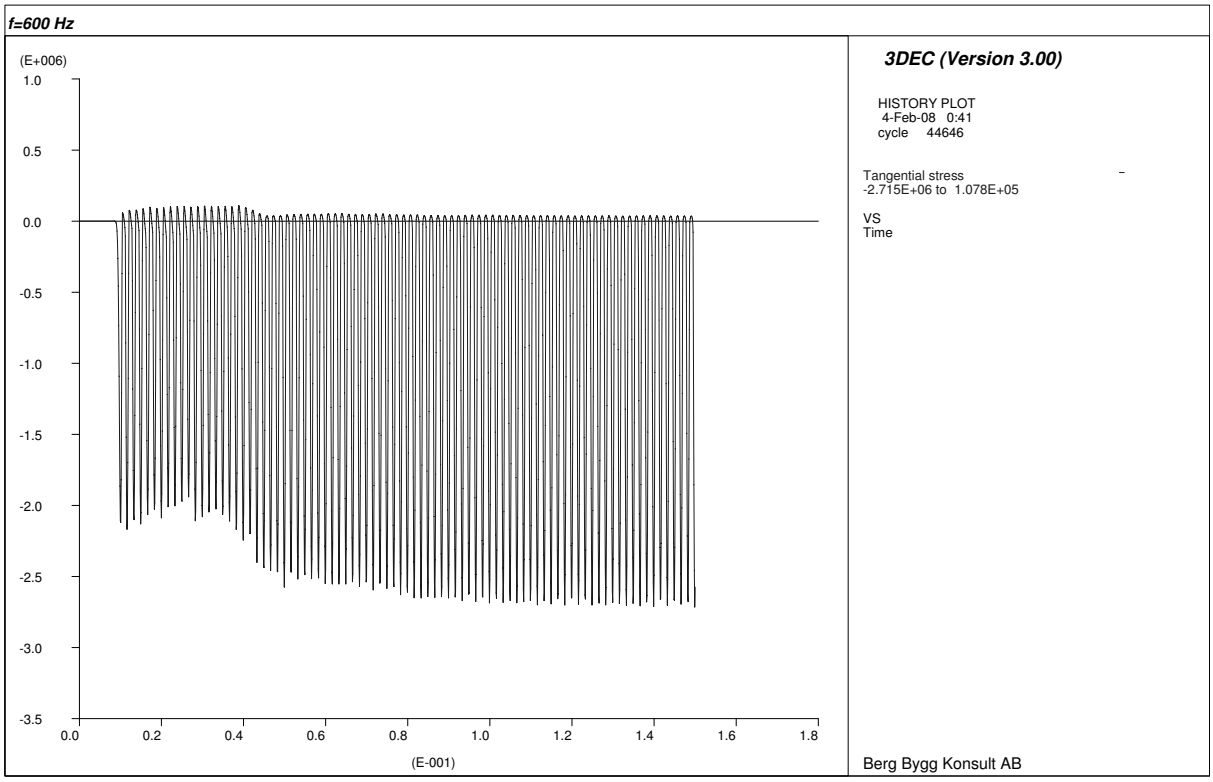

Figure A.33: Tangential stress history for 600 Hz ($r = a = 5$ m, $\theta = \pi/2$).

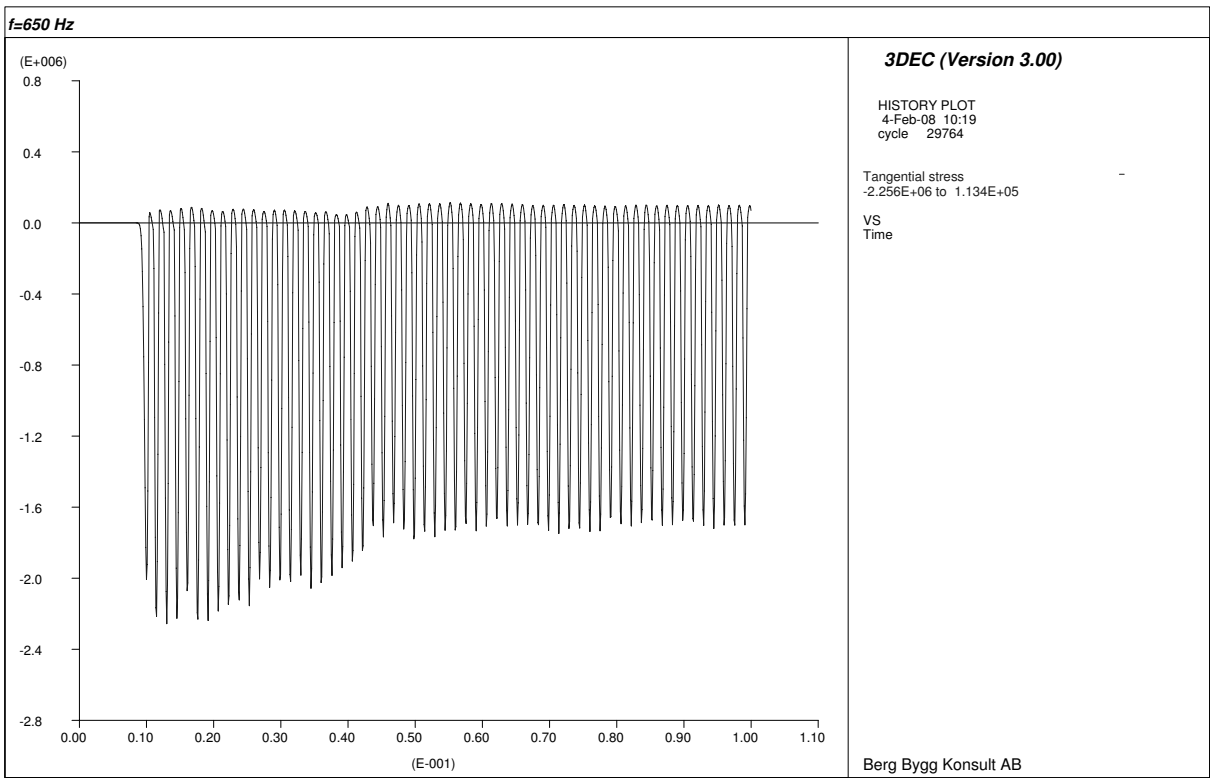

Figure A.34: Tangential stress history for 650 Hz ($r = a = 5$ m, $\theta = \pi/2$).